BONNER METEOROLOGISCHE ABHANDLUNGEN

Heft 90 (2020) (ISSN 0006-7156)
Herausgeber: Andreas Hense

Alexander Kelbch

INVESTIGATIONS TO QUANTIFY INDIVIDUAL EXPOSURE TO SOLAR ULTRAVIOLET ERYTHEMAL RADIATION INCLUDING CLOUD METEOROLOGICAL IMPACT

BONNER METEOROLOGISCHE ABHANDLUNGEN

Heft 90 (2020) (ISSN 0006-7156)
Herausgeber: Andreas Hense

Alexander Kelbch

INVESTIGATIONS TO QUANTIFY INDIVIDUAL EXPOSURE TO SOLAR ULTRAVIOLET ERYTHEMAL RADIATION INCLUDING CLOUD METEOROLOGICAL IMPACT

Investigations to quantify individual exposure to solar ultraviolet erythemal radiation including cloud meteorological impact

Dissertation
zur
Erlangung des Doktorgrades (Dr. rer. nat.)
der
Mathematisch-Naturwissenschaftlichen Fakultät
der
Rheinischen Friedrich-Wilhelms-Universität Bonn

vorgelegt von
M.Sc.
Alexander Kelbch
aus
Tübingen

Bonn, März, 2020

Diese Arbeit ist die ungekürzte Fassung einer der Mathematisch-Naturwissenschaftlichen Fakultät der Rheinischen Friedrich-Wilhelms-Universität Bonn im Jahr 2020 vorgelegten Dissertation von Alexander Kelbch aus Tübingen.

This paper is the unabridged version of a dissertation thesis submitted by Alexander Kelbch born in Tübingen to the Faculty of Mathematical and Natural Sciences of the Rheinische Friedrich-Wilhelms-Universität Bonn in 2020.

Anschrift des Verfassers: Address of the author:

Alexander Kelbch
Institut für Geowissenschaften, Abt. Meteorologie
Universität Bonn
Auf dem Hügel 20
D-53121 Bonn

1. Gutachter: Prof. Dr. Andreas Bott,
Rheinische Friedrich-Wilhelms-Universität Bonn
2. Gutachter: Prof. Dr. Andreas Hense,
Rheinische Friedrich-Wilhelms-Universität Bonn

Tag der Promotion: 25. Juni 2020

Contents

Abstract

Combined meteorological and dosimetric ultraviolet (UV) erythemal radiation (UVER) measurements were performed in 2016 and 2017. Based on collected data sets the actual UVER exposure of outdoor working probands is determined and compared to the globally available UVER dose during their working shifts. The highest absolute UVER dose (7.94 SED) was measured by a track worker which is 23.4% of the maximum possible UVER dose. For each combined measurement event the UV index (UVI) is calculated based on horizontally collected global dosimetric UVER data and compared to the respective public UV hazard forecast provided by the German Meteorological Service (DWD). As a result, the actual UVI is never overestimated. For 56% of the cases UVI forecast and corresponding measurement agree with an absolute difference of 1 UVI. In one case differences up to 8 UVI are observed. The cloud meteorological impact on personal UVER exposure is investigated based on horizontally collected dosimetric UVER data of 16 and 17 August 2016 in Jena. A nonlinear regression was performed to derive a clear sky UVER data set for both days. For both the measured and estimated UVER data sets SimUVEx model simulations were performed. By comparing these simulation results the cloud meteorological impact on the UVER exposure of a human posture is determined and visualized. The trunk front anatomical zone shows the largest relative global UVER dose increase (19.2%). The relative diffuse UVER dose increase, however, is found to be significantly lower and amounts to the same value (3.6%) for all anatomical zones. On 6 and 7 April 2017 meteorological and dosimetric UVER measurements were also performed in Didcot, England. Both days were characterized by clear-sky conditions in the morning and the afternoon with the development of shallow stratocumulus clouds (SSC) around noon. On 7 April a low-ozone event occurred being characterized by a 34 DU (Dobson Unit) drop in total stratospheric ozone content. Compared to 6 April, the ozone mini-hole caused UVER dose increases of 2.67 standard erythema dose (SED) for the diffuse and 4.32 SED for the global radiation part being characterized by radiation amplification factors (RAF) of 1.62 and 1.52, respectively. As innovation the RAF is decomposed into two parts, named cloud ozone factor (COF) and radiation amplification factor based on measured data (RAF_m), to quantify the low-ozone event's effect and the SSC influence in independently modifying the UVER doses. Hereby the weight of each of these two effects acting during the same low-ozone event is expressed by the new COF. In this case the COF values range between -0.13 and -0.11 for diffuse UVER and -0.03 to -0.07 for the global UV and UV-B parts. A positive COF value (0.18) results for the global UV-A range. For this event also a mean spectral COF is calculated based on global UVER spectroradiometer data. As a result the minimum mean spectral COF values amount to $\sim$0.02 in the spectral range between 305 - 310 nm indicating almost no cloud impact on the UVER dose ratio despite cloudy conditions.

Kurzzusammenfassung

In den Jahren 2016 und 2017 wurden Messungen durchgeführt bei denen sowohl meteorologische Daten als auch dosimetrische Daten der erythemgewichteten ultravioletten (UV) Sonnenstrahlung (engl.: ultraviolet erythemal radiation (UVER)) gesammelt wurden. Basierend auf diesen Messungen wird die UVER-Exposition von im Freien arbeitenden Probanden bestimmt und mit der während ihrer Schicht tatsächlich verfügbaren globalen UVER Dosis verglichen. Die höchste absolute UVER Dosis (7.94 SED) wurde von einem Gleisarbeiter gemessen, was einem Anteil von 23.4% der maximal verfügbaren Dosis entspricht. Auf der Basis der globalen UVER Dosimeterdaten wird außerdem der UV-Index (UVI) zu jeder Messung bestimmt und mit der UV-Index Vorhersage des Deutschen Wetterdienstes (DWD) verglichen. Die Ergebnisse zeigen,

dass der tatsächliche UV Index generell nie überschätzt wird. Für 56% der Fälle stimmen prognostizierter und gemessener UV Index mit einer maximalen Differenz von 1 UVI überein. In einem Fall wird eine Differenz von 8 UVI beobachtet. Der meteorologische Einfluss in Form von Wolken auf die individuelle UVER-Exposition wird mit Hilfe von dosimetrischen UVER-Daten untersucht, die am 16. und 17. August 2016 mit horizontal ausgerichteten Dosimetern gemessen wurden. Auf der Grundlage dieser Dosimeterdaten wurde mittels einer nichtlinearen Regression ein Datensatz zur Abschätzung der UVER-Exposition für wolkenlose Bedingungen erzeugt. Mit beiden Datensätzen wurden SimUVEx-Modellsimulationen durchgeführt, wobei jeweils die individuelle UVER-Exposition bezogen auf die anatomischen Zonen einer menschenähnlichen Figur bestimmt wurde. Durch Vergleich der Simulationsergebnisse wird der Wolkeneinfluss auf die individuelle UVER-Exposition quantifiziert und visualisiert. Für den Körperbereich Rumpf-Vorderseite ergibt sich die stärkste relative Änderung der globalen UVER Dosis (19.2%). Die relative Änderung der diffusen UVER Dosis stellt sich hingegen als bedeutend kleiner heraus und ist betragsmäßig identisch für alle Körperbereiche (3.6%). Weitere meteorologische sowie dosimetrische Messungen der UVER-Exposition fanden am 6. und 7. April 2017 in Didcot, England, statt. Beide Messtage waren sowohl morgens als auch ab dem späteren Nachmittag durch wolkenlose Bedingungen charakterisiert, wobei sich jeweils über die Mittagsstunden flache Stratocumulus Bewölkung entwickelte. Am 7. April ereignete sich zudem ein 'low-ozone event' (Mini-Ozonloch), das durch einen Abfall des stratosphärischen Ozongehalts von 34 DU (engl.: Dobson Unit) charakterisiert ist. Im Vergleich zum Vortag (6. April) stieg die UVER-Dosis im gleichen Zeitraum bedingt durch das Mini-Ozonloch um 2.67 SED (engl.: standard erythema dose) bezogen auf die diffuse und um 4.32 SED bezogen auf die globale UVER Dosis. Dies entspricht einem Strahlungsverstärkungsfaktor (engl.: radiation amplification factor (RAF)) von 1.62 beziehungsweise 1.52. Als Innovation wird der RAF bei den durchgeführten Analysen in zwei Teile zerlegt, den Wolken-Ozon Faktor (engl.: cloud ozone factor (COF)) und den auf gemessenen UVER-Werten basierenden Strahlungsverstärkungsfaktor (engl.: RAF_m), um die voneinander unabhängigen Effekte von Mini-Ozonloch und Stratocumulus-Bewölkung auf die UVER-Dosis zu bestimmen. Dabei drückt der COF das relative Gewicht der beiden Prozesse aus. Im untersuchten Fall weist der COF Werte zwischen -0.13 und -0.11 für diffuse UVER sowie Werte zwischen -0.03 und -0.07 für den globalen UVER beziehungsweise den UV-B Teil auf. Für den globalen UV-A Anteil ergibt sich ein positiver COF von 0.18. Zusätzlich konnte für dieses Event ein spektraler COF auf der Basis von Spektralradiometer-Messungen bestimmt werden. Für den Wellenlängenbereich zwischen 305 und 310 nm ergeben sich minimale spektrale COF-Werte von $\sim$0.02, was bedeutet, dass das Verhältnis von gemessenen UVER-Dosen (mit Bewölkung) näherungsweise identisch zum Verhältnis der geschätzten UVER-Dosen (wolkenlose Bedingungen) ist.

1 Introduction

Motivation

Solar UV radiation influences the human body especially by affecting and penetrating into the outer body protection layer - the human skin. The human body adapted during its evolutionary development to the latitudinally highly different levels of solar UV radiation by providing different levels of skin pigmentation with the maximum skin pigmentation being observed in the tropics (Jablonski and Chaplin 2010). Subsequently, huge differences regarding the occurrence of melanoma have been developed which is, for example, 25 times higher for non-Hispanic white populations compared to black populations (Watson et al. 2016). High exposure to solar UV radiation on short time scales may lead to spontaneous skin reactions like erythema or keratitis whereas skin cancer, skin ageing or lens opacification mostly occur after longstanding UV exposure (Setlow 1974; Setlow et al. 1993; Ambach and Blumthaler 1993; Greinert et al. 2015). Children may be particularly endangered in urban areas due to the habitual UV exposure behaviour of urban populations (Heisler and Grant 2000). The amount of solar UV radiation reaching the surface and which may thus affect the human skin is partly determined by the stratospheric ozone concentration. A 10% decrease in stratospheric ozone, for example, leads to a 26% increase in skin cancer occurrence and to a 6-8% increase regarding the occurrence

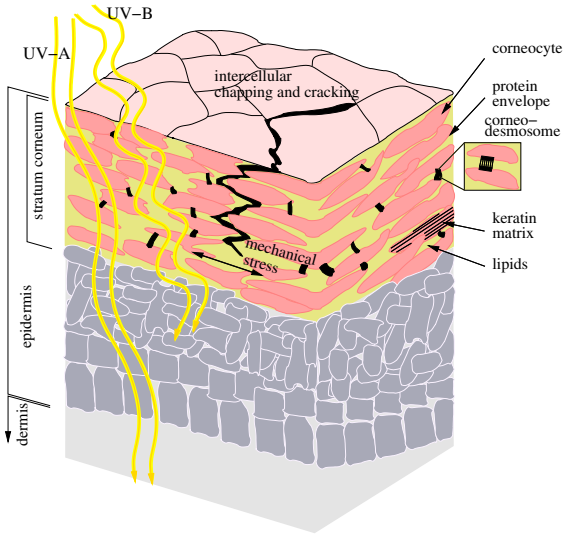

Fig. 1: UV radiation impact on human skin, leaned on Biniek et al. (2012).

of cataracts (Ambach and Blumthaler 1993). The outermost layer of the human skin is called stratum corneum (Fig. 1) which has an important barrier function regarding environmental influences (Biniek et al. 2012). A change in this barrier function, caused by solar UV radiation for example, may lead to inflammation, chapping, scarring or infections, subsequently. Biniek et al. (2012) found the impact of solar UV radiation on human skin to be twofold by forcing the damage of the biomechanical skin functioning and by reducing the natural skin sustainability. Another important effect of solar UV radiation on human health is the vitamin D synthesis with UV-B radiation being responsible for the reaction of provitamin D into previtamin D (Engelsen 2010). Vitamin D positively

affects bone health and it is suggested to act preventive regarding cancer, autoimmune diseases and influenza (e.g. Reichrath 2007; Engelsen 2010), whereas a lack of vitamin D is regarded as a global health problem (Holick 2008). A vitamin D deficit as a result of almost completely avoiding the sun may lead to diseases like multiple sclerosis, arthritis, diabetes and cardiovascular disease for example (Juzeniene et al. 2011; Tsiaras and Weinstock 2011). McKenzie et al. (2009) investigated the relation between both harmful and beneficial effects of solar UV radiation on human health. Their results show a 1 *min* complete body exposure to solar UV radiation in midlatitude summer to be sufficient for the vitamin D production, while the harmful impact on the skin occurs only after 15 *min*. In order to better protect and prevent human beings from the harmful effects of solar UV radiation it is important to recognize the amount of UV radiation reaching the human body to be highly variable and to strongly depend on the anatomical zone, the season and that it has a pronounced diurnal variability (Hu et al. 2010) especially due to meteorological influences.

Influences on solar UV radiation

According to the World Meteorological Organization (WMO 2010), 97% of the extraterrestrial solar spectrum (blue line, Fig. 2) is confined to the wavelength (λ) interval from 290 to 3000 *nm*, hereafter named solar radiation. The solar spectrum is subdivided into several intervals called the infrared ($\lambda > 700$ *nm*), the visible ($400\ nm < \lambda < 700\ nm$) and the ultraviolet ($100\ nm < \lambda < 400\ nm$) range, as indicated by the grey vertical lines in Fig. 2. The solar UV radiation spectrum is subdivided into three sub-ranges: UV-C includes wavelengths between 100 - 280 *nm*, UV-B ranges from 280 - 315 *nm* and UV-A stretches from 315 to 400 *nm* according to the International Commission on Illumination (CIE 1987).

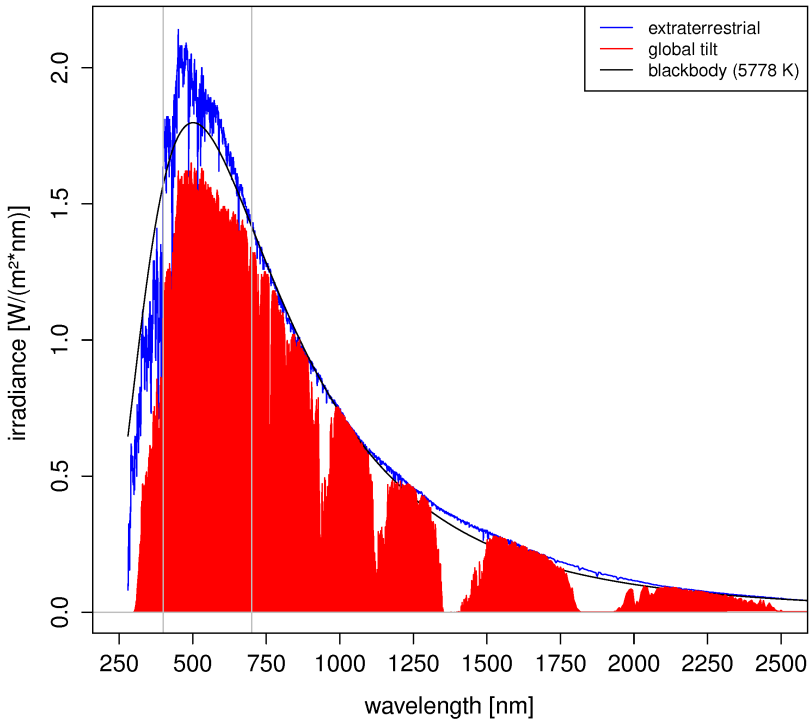

Fig. 2: Blackbody and ASTM reference spectra (https://rredx.nrel.gov)

The amount of UV radiation reaching the earth's surface shows variabilities on a broad range of timescales reaching from thousands of years down to time periods of less than one hour. The UV variabilities with the largest timescales are related to astronomical effects like changes of the earth's ecliptic, precession and eccentricity. On shorter astronomical timescales UV radiation variabilities occur due to changes in both sun's activity and rotation cycles. These large-scale variations effectively act through amplifying or attenuating and shifting the total solar spectrum including its ultraviolet part. The temperature response to the 11-year solar cycle, for example, shows a maximum of 1.6 K in the upper equatorial stratosphere due to irradiance changes and a secondary maximum in the lower parts of the equatorial stratosphere related to ozone variations (Gray et al. 2009).

Due to the general stratospheric circulation (Brewer 1949) the ozone concentrations increase with higher latitude directly affecting the incoming solar UV radiation. During spring time, however, photochemical processes cause strong ozone depletion in the polar regions inversing the regular increase of the ozone amount with latitude (Sola and Lorente 2011). According to Taalas et al. (1997) the springtime stratospheric ozone loss has a significant impact on upper tropospheric ozone resulting in a decrease of -12.8% in the antarctic and -10% in arctic regions, respectively. The latitudinal changes of ozone concentration act differently on UV-A and UV-B radiation parts due to the strong wavelength dependency of the ozone absorption efficiency. Thus, ozone absorption influences the UV-B range by strongly reducing the amount of UV-B radiation reaching the earth's surface. The UV-A spectral range is much less affected by changes in total ozone concentration resulting in much smaller variability with respect to latitudinal changes. The photochemical processes acting on the production and destruction reactions of stratospheric ozone will be described in more detail in the second chapter.

Variations of the amount of surface UV radiation on a daily timescale arise from the solar diurnal cycle, the influence of clouds as well as scattering and absorption processes of atmospheric gases. According to the following expression

$$I(\Theta_s) \propto \lambda^{-4} \tag{1.1}$$

with the scattering angle Θ_s, the scattering intensity $I(\Theta_s)$ of air molecules (Rayleigh scattering) is proportional to the inverse fourth power of the wavelength λ. As a result of this scattering behaviour the skies are colored blue during daytime and change into a reddish coloring for large solar zenith angles (morning and evening). Besides the scattering processes the incoming solar radiation is attenuated by absorption of different atmospheric gases like water vapor, oxygen, ozone and carbon dioxide. Thus, for clear sky conditions, the resulting solar spectrum measured at the earth's surface shows a significant overall attenuation of the visible spectral range and is characterized by strong irradiance decreases within specific narrow spectral bands (red area, Fig. 2). The ozone absorption specifically causes the pronounced decrease in the ultraviolet spectral range. Water vapor and carbon dioxide, instead, more effectively absorb in the infrared spectral range. At surface levels, the solar radiation shows its highest intensities in the visible part (Fig. 2) in comparison to the infrared and especially to the UV spectral intervals being much less intense. The theoretical framework being used to describe atmospheric scattering and absorption processes, the Mie theory, will be introduced in section 2.

In general, meteorological processes develop as a consequence of the transformation and redistribution of the incoming solar radiative energy via thermal and latent energy fluxes as visualized in the annual mean solar radiation budget (Fig. 3) of the energy fluxes within

the earth-atmosphere system (Trenberth et al. 2009). After having developed, meteorological processes themselves influence the incoming solar radiation in form of scattering

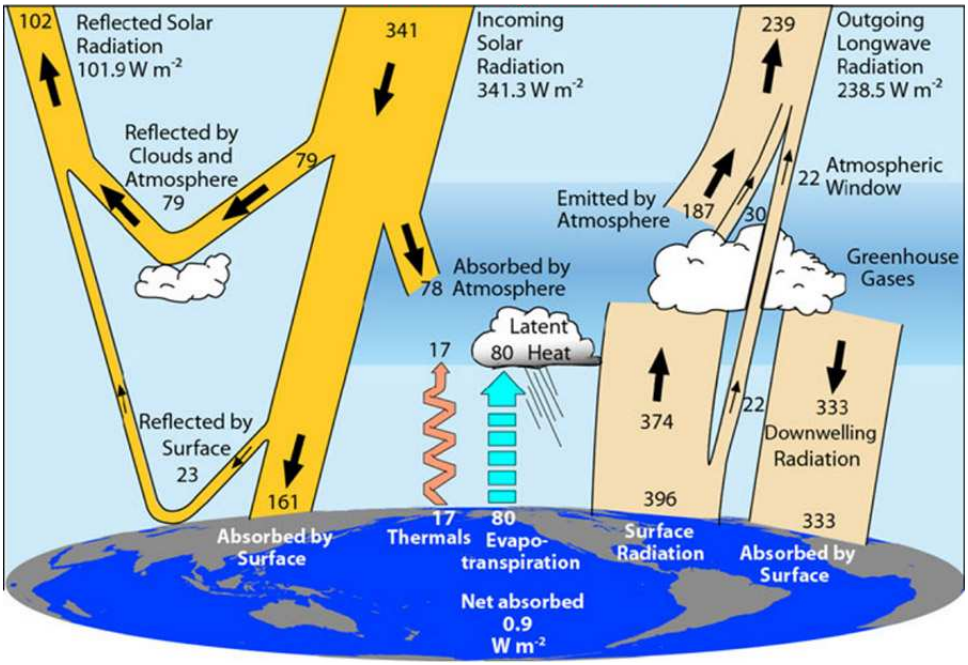

Fig. 3: Radiation budget of the atmosphere, global energy flows (Wm^{-2}) (Trenberth et al. 2009).

and absorption processes either amplifying or attenuating the amount of solar radiation reaching the surface. Elaborating the cloud meteorological influence on individual exposure to solar UVER is one of the major research topics of the thesis at hand.

Research conception and objectives

People having worked outside for many years were often exposed to the sun during their occupational activities (Milon et al. 2014). Boniol et al. (2015) estimated the occupational daily standard erythema dose (SED) for french outdoor workers and found out that gardeners, construction or agricultural workers were exposed to solar UV erythemal radiation (UVER) with more than 1 SED per day (1 SED amounts to a UVER dose of 100 Jm^{-2} (CIE 2014)). As introduced above UV irradiance penetrating into the human skin affects different skin layers and leads to different responses directly affecting the skin or acting on the immune system in general (Heisler and Grant 2000). High diurnal UV doses may cause sunburns (erythema) of different kind. Longstanding UV exposure can subsequently lead to skin cancer.

By law, skin cancer was accepted as occupational disease in Germany in 2015 (BKV 1997). To provide a profound data base to assess the UV exposure to individual occupational disease cases, the Institute for Occupational Safety and Health (IFA) of the German Social Accident Insurance (DGUV) launched a research project to collect exposure data for different jobs and job tasks (Wittlich et al. 2016). The core of this research campaign is a platform called GENESIS-UV (GENeration and Extraction System for Individual expoSure) consisting of dosimeters for exposure measurements by probands, tablet com-

puters serving as user interfaces and a data storage server (Wittlich et al. 2016). To elaborate the actual exposure to solar UV radiation of people working outside a mobile meteorological station was composed and subsequently used to measure the solar UV irradiance data as well as the atmospheric state synchronously to dosimeter measurements performed by probands during their outdoor work.

The meteorological influence on the amount of solar irradiance reaching the ground and thus on individual UVER exposure is evident. Clouds for instance lead to an attenuation of the incoming solar UV radiation at the surface of different magnitude depending on cloud type, level, optical thickness and spatio-temporal variability (Calbó et al. 2005). On the other hand scattering processes from clouds may lead to an increase in surface UV irradiance up to 50 % in the UV-B and 30 % in the UV-A spectral range as measured in Girona, Spain (Feister et al. 2015). Calbó et al. (2017) found UV irradiance enhancements up to 1.3 *CMF* (cloud modification factor) obtained from measured data in Lauder, New Zealand. Mateos et al. (2015) performed spectral measurements for global and diffuse UV irradiance showing a strong solar zenith angle (SZA) dependency of the *CMF* for both parts. McKenzie et al. (1991) related measured spectral UV irradiance data to total ozone measurements emphasizing the relative importance of SZA, cloud cover and ozone variations. Besides the SZA being dominant, their results also show a temporarily strong cloud influence with UV irradiance reductions up to 50 %. Optically thick clouds lead to strongly increased scattering activity with a photon path enhancement of 10 times and more and thus a pronounced attenuation of UV irradiance under the clouds due to an increased absorption by tropospheric ozone and aerosol (Mayer et al. 1998). Serrano et al. (2006) also identified clouds to be mainly responsible for daily and annual UVER amounts having performed a study to statistically describe the UVER distribution in Badajoz, Spain. Obviously, the presence of clouds affects the daily UV dose which may be gathered by people working outside.

The investigations presented in the thesis at hand deal with the meteorological influence in form of clouds on individual exposure to surface solar UV radiation on a time scale of several hours. The impact of both clouds and a low-ozone event independently affecting the surface UVER is also analyzed based on dosimetric and spectral UV irradiance data. The research objectives will be addressed in section 4 by providing answers to the following research questions:

1. How strong is the actual UVER exposure of outdoor workers?
2. Is the UV-Index a sufficient tool to inform the public about harmful solar UV radiation?
3. How strong is the cloud meteorological effect on individual UVER exposure?
4. How strong is the impact of both clouds and a low-ozone event in independently affecting surface solar UVER?
5. How can spectral UVER data be used to further characterize ozone mini-holes?

2 Theoretical background

2.1 Solar radiation

According to Kren (2015) 99.98% of the energy sourcing atmospheric and biological processes on Earth originates either directly or indirectly from radiative energy emitted by the sun. At the top of the atmosphere (TOA), after having traveled the average sun-earth distance of $1.496 \times 10^{11}\ m$, the incoming longterm mean radiant flux density amounts to $1360.8 \pm 0.5\ Wm^{-2}$ (Kopp and Lean 2011), often somewhat misleading (Kopp 2016) referred to as the solar constant S_0. Due to the 11-year solar cycle, S_0 shows variations amounting up to 0.1% (Fröhlich 2006).

The solar spectrum contains electromagnetic waves ranging from X-rays (roentgen) to radio waves and it is characterized by a peak intensity within the visible spectral interval (390 - 700 nm, see Fig. 2). Most of the solar radiation is referred to as thermal radiation being related to the respective surface temperature of the emitting body. As part of ionizing radiation, X-rays originate from highly excited atoms or charged particles which are accelerated or decelerated, respecitvely. Solar flares, for example, are major sources for X-rays reaching the earth's surface (Kopp 2016) with large flare events leading to short-time increases of the total solar irradiance up to 0.028% (Kopp et al. 2005). According to Kirchhoff's law of thermal radiation, given by

$$E_\lambda(\lambda, T) = \epsilon_\lambda E_{\lambda,black}(\lambda, T), \tag{2.2}$$

the wavelength-specific emission $E_\lambda(\lambda, T)$ of radiative energy of an arbitrary body in thermodynamic equilibrium with temperature T can be expressed by its emissivity ϵ_λ and the perfect black body energy emission $E_{\lambda,black}(\lambda, T)$. The spectral energy emission of a black body is given by Planck's law denoted as

$$\frac{\partial E_{\lambda,black}(\lambda, T)}{\partial \lambda} d\lambda = \frac{2\pi hc^2}{\lambda^5} \frac{1}{\left(\exp(\frac{hc}{k_B \lambda T}) - 1\right)} d\lambda \tag{2.3}$$

with the body temperature T, the thermal radiation wavelength λ, Planck's constant h, the speed of light c and k_B the Boltzmann constant. The magnitude of the extraterrestrial black-body spectrum (cf. Fig. 2) results by applying the correction factor ${r^2}_{sun} {r^{-2}}_{sun-earth}$ to take the mean sun-earth distance of 1 AU into account.

As introduced earlier, a major research topic investigated in this thesis are processes affecting the amount of solar UV radiation reaching the surface. With UV radiation being a small part of the solar spectrum with wavelengths ranging between 100 and 400 nm, the World Meteorological Organization (WMO) introduced a dimensionless number called the UV index (UVI) in order to inform the public about the expected surface UV irradiance intensity. In 2002 the International Illumination Commission (CIE) adopted the UVI officially (CIE 2002) which is defined as:

$$UVI = k_{er} \int_{280nm}^{400nm} E(\lambda) s_{er} d\lambda \tag{2.4}$$

with E(λ) [W m^{-2} nm^{-1}] being the spectral solar irradiance on a horizontal plane. λ and dλ [nm] represent wavelength and wavelength interval, respectively. $k_{er} = 40$ $[m^2W^{-1}]$ represents a constant, choosen to achieve the desired simple UVI values for the public. s_{er} represents the erythema reference action spectrum defined as follows (CIE 2014):

$$
\begin{aligned}
s_{er} &= 1.0 && \text{for } 250\ nm \leq \lambda \leq 298\ nm \\
s_{er} &= 10^{0.094(298-\lambda nm^{-1})} && \text{for } 298\ nm < \lambda \leq 328\ nm \\
s_{er} &= 10^{0.015(140-\lambda nm^{-1})} && \text{for } 328\ nm < \lambda \leq 400\ nm
\end{aligned}
$$

According to McKenzie et al. (2017) UVI values up to 300 can be reached above the Earth's atmosphere with the highest terrestrial UVI value (SZA = 0) being estimated to 38.5 (WMO 2010b). Gillotay et al. (2005) provide a potential improvement of UV indices for cloudy conditions by including cloud coverage (okta) from model output and a mean optical density expressing the cloud induced solar radiation attenuation. Madronich (2007) introduced an analytic formula to calculate clear-sky UV index values.

Another important quantity is the erythemal effective UV dose. According to DWD (2015), it represents the erythemal effective amount of energy on a horizontal plane within a given time interval and the unit $[J_{ery}m^{-2}]$. This quantity can easily be calculated by dividing the hourly UVI by 40 $W^{-1}m^2$ and multiplying the result by 3600 s, yielding the hourly erythemal effective dose. As a forecast product, the erythemal effective dose is calculated with an integration time of one day and is influenced by the same factors valid for the UV irradiance.

2.2 The Mie theory

In general, scattering processes in the atmosphere cause a direction change of the incident solar radiation (photons) on its way down to the earth's surface. Numerous gaseous, liquid or solid constituents of the atmosphere like ozone, oxygen, nitrogen, aerosols, water vapour and water droplets of different sizes affect the incoming photons causing different types of scattering. A scattering process is called 'elastic' if the photon's frequency remains unchanged while undergoing a change in path direction. Inelastic scattering, on the contrary, is characterized by both a shift in direction and frequency (Zdunkowski et al. 2007).

The Mie theory (Mie 1908) is a mathematical tool to describe different scattering processes of electromagnetic waves at homogeneous spherical objects. The probability of a photon with frequency ν being elastically scattered into the solid angle segment $d\Omega_s$ while traveling the distance dl can be expressed by the differential scattering optical depth as given by

$$
d\tau_s(\mathbf{r}, \mathbf{\Omega} \rightarrow \mathbf{\Omega}_s, t) = k_{s,\nu}(\mathbf{r}, \mathbf{\Omega} \rightarrow \mathbf{\Omega}_s, t) d\Omega_s dl \tag{2.5}
$$

with the position vector $\mathbf{r}$ as well as the photon's travel directions $\mathbf{\Omega}$ and $\mathbf{\Omega}_s$ prior to and after the scattering process, respectively. $k_{s,\nu}(\mathbf{r}, \mathbf{\Omega} \rightarrow \mathbf{\Omega}_s, t)$ denotes the differential scattering coefficient.

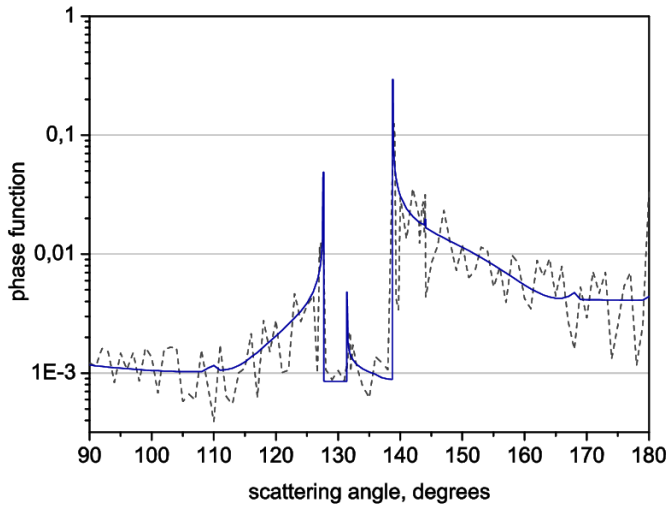

Fig. 4: Calculated rainbow phase function (Fomin and Falaleeva 2012)

Each scattering process is characterized by a specific scattering phase function $P_{s,\nu}(\mathbf{r}, \mathbf{\Omega} \rightarrow \mathbf{\Omega}_s, t)$ describing the distribution of the scattered photons with each of them being characterized by a scattering related direction change ($\mathbf{\Omega} \rightarrow \mathbf{\Omega}_s$). The scattering phase function is defined by

$$\frac{k_{s,\nu}(\mathbf{r}, \mathbf{\Omega} \rightarrow \mathbf{\Omega}_s, t)}{k_{s,\nu}(\mathbf{r}, t)} = \frac{1}{4\pi} P_{s,\nu}(\mathbf{r}, \mathbf{\Omega} \rightarrow \mathbf{\Omega}_s, t) \tag{2.6}$$

with the scattering coefficient $k_{s,\nu}(\mathbf{r}, t)$ resulting from the integration of $k_{s,\nu}(\mathbf{r}, \mathbf{\Omega} \rightarrow \mathbf{\Omega}_s, t)$ over the full solid angle.

Visualizing a specific scattering phase function may help understanding the underlying scattering process. As an example the rainbow scattering phase function (Fig. 4) may be considered being characterized by two pronounced maxima occurring for scattering angles of $\theta_s = 127°$ and $\theta_s = 140°$. Per definition, the scattering angle θ_s spans between the directions of the incident ($\mathbf{\Omega}$) and scattered ($\mathbf{\Omega}_s$) radiation.

In general, regarding the number of photons being scattered, two scattering types can be distinguished:

- Single scattering is characterized by photons being scattered only once. This scattering type occurs predominantly in optically thin media ($\tau \ll 1$).
- Multiple scattering, on the contrary, occurs for optically thick ($\tau \gg 1$) but non-absorbing media.

In contrast to scattering, absorption is the process of including photons, while on their path through the atmosphere, into the energetic structure of atoms or molecules of an atmospheric component (Zdunkowski et al. 2007). After the absorption process took place, the photons involved have disappeared. Due to the increased path length of a scattered photon, there is an enhanced probability for the photon to be absorbed. Thus, scattering processes in the atmosphere may subsequently lead to a higher number of photons being absorbed. According to Planck's law, cf. eq. (2.4), this energy exchange

can only amount to multiples of the photon energy $h\nu$. The energy state of atoms or molecules is described by translational, rotational and vibrational energy as well as the electric charge distribution within molecules. The probability of a photon being absorbed along the path element dl within an isotropic medium can be described by the differential optical depth for absorption $\mathrm{d}\tau_a$ as given by

$$d\tau_a(\mathbf{r}, t) = k_{a,\nu}(\mathbf{r}, t)dl \tag{2.7}$$

with the absorption coefficient $k_{a,\nu}(\mathbf{r}, t)$ for a photon frequency ν. Very important thermodynamic processes in the atmosphere are directly linked to absorption processes like for example photodissociation or stratospheric heating. The amount of both, absorption and scattering combined, is called extinction with the extinciton coefficient $k_{e,\nu}$ being defined as

$$k_{e,\nu}(\mathbf{r}, t) = k_{a,\nu}(\mathbf{r}, t) + k_{s,\nu}(\mathbf{r}, t). \tag{2.8}$$

The ratio of scattering and extinction coefficients defines the single scattering albedo $\omega_{0,\nu}$ expressed by the following equation

$$\omega_{0,\nu}(\mathbf{r}, t) = \frac{k_{s,\nu}(\mathbf{r}, t)}{k_{e,\nu}(\mathbf{r}, t)} \tag{2.9}$$

describing the amount to which scattering contributes to the total photon extinction. As an example, high albedo values often occur in the Arctic as sea ice leads to the backscattering of the incoming solar radiation. Decreasing sea ice, however, causes lower albedo and thus higher surface absorption subsequently leading to further warming and ice melting in the arctic region (Thackeray and Hall 2019). As described by (2.2) matter emits photons based on its specific emissivity ϵ_λ which equals its absorptivity a_λ under thermodynamic equilibrium. The emission of photons is mathematically expressed by introducing the emission coefficient $j_\nu(\mathbf{r}, t)$ into the equation

$$\frac{\partial N_\nu(\mathbf{r}, t)}{\partial t} \,|_{em} = j_\nu(\mathbf{r}, t)dV d\Omega d\nu \tag{2.10}$$

describing the number of photons N_ν being emitted per unit time and unit volume within the frequency interval $(\nu, \nu + d\nu)$ into the solid angle element $d\Omega$. In addition to their impact on shortwave solar radiation (scattering) atmospheric trace gases like ozone, carbon dioxide or methane also have a significant influence on the earth-atmosphere long-wave radiation budget.

As introduced in equation (2.6), the scattering phase function $P_{s,\nu}(\mathbf{r}, \mathbf{\Omega} \rightarrow \mathbf{\Omega}_s, t)$ describes the photon distribution as being provided by the Mie theory for spherical objects. The $P_{s,\nu}$ distribution is determined by only two physical parameters named the complex index of refraction $N = n + i\kappa$, with the real part n and the imaginary part κ, as well as the Mie size parameter x being defined as

$$x = \frac{2\pi r}{\lambda} \tag{2.11}$$

relating the spherical particle's radius r and the wavelength λ of the incoming radiation. Applying typical values for the particle radius (for molecules $\sim 10^{-4}$ μm) and the respective wavelength, the Mie size parameter characterizes three different scattering regimes:

- $x \ll 1$: Rayleigh scattering
- $x \sim 1$: Mie scattering
- $x \gg 1$: Geometrical scattering

Another factor characterizing a scattering process is the scattering cross-section C_s given by

$$C_s = \frac{\phi^s}{E^i} = \frac{1}{E^i} \oint_{4\pi r^2} E^s dA \tag{2.12}$$

describing the ratio of the scattered energy flux ϕ^s and the incident radiative energy E^i. C_s has the unit of (m^2) and can thus be interpreted as the area affected by a particle causing a scattering process (Zdunkowski et al. 2007).

Rayleigh scattering occurs in the earth's atmosphere due to the incoming solar radiation interacting with gas molecules. As introduced above, Rayleigh scattering is characterized by a very small Mie size parameter ($x \ll 1$) and can thus be treated as a special case of Mie scattering with the following scattering cross-section (Zdunkowski et al. 2007):

$$C_s = \frac{8\pi(N^2-1)^2}{3{k_0}^2(N^2+2)^2}{\rho_0}^6 \tag{2.13}$$

with the wave number k_0 and the factor $\rho_0 = 2\pi a\lambda^{-1}$. The variable a hereby denotes the scattering particle radius. The distribution of the ultraviolet, visual and near infrared parts of the solar radiation spectrum can be explained by means of Rayleigh scattering.

Very important from the meteorological point of view is Rayleigh scattering of microwaves at rain droplets. The reason for this is the size ratio between the electromagnetic wave and the scattering object amounting to the same magnitude compared to the interaction of radiation in the visible spectrum with air molecules. By using the backscattered radiative energy radar (radio detection and ranging) technologies allow the determination of rain intensity or rate, for example. Meteorological radars work based on the radar equation, derived by Probert-Jones (1962), describing the average reflected power received back at the radar which is denoted as $\bar{P}_r$. According to WMO (2010) a simplified equation for $\bar{P}_r$ can be used, given by

$$\bar{P}_r = \frac{C|K|^2 Z}{r^2} \tag{2.14}$$

with the radar constant C, the target refractive index factor $|K|^2$, the distance r from radar to target and the radar reflectivity factor Z. An important radar specific variable, being included in C, is the transmitted wavelength band mostly stretching in one of the following three spectral ranges (WMO 2010): 2.4 to 3.75 cm, 3.75 to 7.5 cm and 7.5 to 15 cm for X-, C- and S-band radars, respectively. The radar reflectivity Z is expressed by

$$Z = \sum_{volume} N(D)D^6 \tag{2.15}$$

with $N(D)$ being the number of drops with the respective particle diameter D. The unit for Z is mm^6m^{-3}. The amount of rain reaching the ground per hour, also called rainfall

rate R, can be calculated using the following equation (WMO 2010):

$$R = \sum_{volume} N(D) V_T \rho \frac{\pi}{6} D^3 \tag{2.16}$$

with the velocity of the falling droplets being denoted as V_T and the air density ρ. The unit of R is $mm(h)^{-1}$. There is a problem for practical purpuses as $N(D)$ is unkown. Therefore empirical formulas have been derived directly relating the radar reflectivity factor Z and the rainfall rate R. The relation given as

$$Z = 200R^{1.6} \tag{2.17}$$

is a widely used Z-R relation which was derived by Marshall and Palmer (1948) and thus also being known as Marshall-Palmer relationship.

Mie scattering is characterized by Mie size parameters $x \sim 1$ reflecting the scattering particle size and the scattered electromagnetic wave being roughly of the same length scale. The Mie phase function $P_{Mie}(\cos\theta_s)$ describes the photon distribution for Mie scattering. An approximation for $P_{Mie}(\cos\theta_s)$ is the Henyey-Greenstein phase function $P_{H-G}(\cos\theta_s)$ which is according to Zdunkowski et al. (2007) given by:

$$P_{H-G}(\cos\theta_s) = \frac{1-g^2}{(1+g^2-2g\cos\theta_s)^{\frac{3}{2}}} \tag{2.18}$$

using the asymmetry parameter g being defined by the following expression:

$$g = \frac{1}{2}\int_{-1}^{1} \cos\theta_s P(\cos\theta_s) d\cos\theta_s \tag{2.19}$$

Mie scattering occurs in the Earth's atmosphere as interaction of the incoming solar radiation ($\sim$ 400-800 nm in the visible range) and cloud or aerosol particles with a diameter being roughly in the same size range (2.5 - 20 μm) according to Pruppacher and Klett (1997).

Large Mie size parameters, i.e. $x \gg 1$, indicate geometrical scattering with scattering particle radii being much larger than the wavelength of the interacting (solar) radiation, for example. The rainbow, a well-known atmospheric phenomenon, can be explained by geometrical optics.

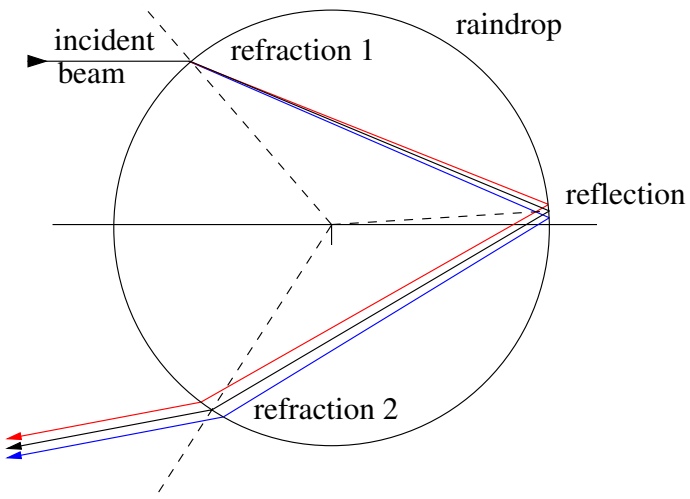

Fig. 5: Refraction and reflection of solar rays in a spherical raindrop causing the primary rainbow. Sketch leaned on Adam (2002).

According to Adam (2002) the primary rainbow results from a combination of refractions and reflections of the visible part of the incoming solar radiation taking place synchronously within a countless number of raindrops. As indicated in Fig. 5, the key mechanism leading to the fanning out of the incoming (white) solar beam into different colors is the wavelength dependent refraction at the raindrop surface. Shorter wavelengths are characterized by a significantly higher refraction index being responsible for the stronger refraction of the blue compared to the red beam (Fig. 5). Therefore, from the viewers point of view, the primary rainbow is characterized by reddish colors at its upper (outer) parts and blue colors at its inner (lower) edges.

2.3 Stratosphere and troposphere

The Earth's atmosphere consists of several layers with each layer being characterized by a different vertical temperature profile (Fig. 6). The vertical extension of each atmospheric layer depends on latitude, season and circulation systems within or between the respective layer(s). The sphere closest to the Earth's surface is called troposphere subsequently being followed, with increasing height, by stratosphere, mesosphere, thermosphere and the outermost layer called exosphere (not shown in Fig. 6). These layers are separated from each other by relatively narrow vertical transition zones named tropopause, stratopause and mesopause, respectively (e.g. Holton 2004). For mainly two reasons both troposphere and stratosphere are of particular relevance for the evaluations presented in a later chapter of the thesis at hand:

1. Firstly, processes occuring in either the stratosphere or the troposphere may strongly affect the incoming solar radiation. These processes are variations in total stratospheric ozone content and cloud meteorological impact, respectively. The aerosol concentration which can also have a significant impact on surface UV doses, however, will not be analyzed in the thesis at hand.

2. Secondly, interactions between both the stratosphere and the troposphere may result in variations of the total ozone amount and may therefore significantly affect the amount of UV radiation at surface levels. These interactions include processes like stratosphere-troposphere exchange (STE) or meteorological influences resulting from large-scale circulation patterns causing stratosphere-troposphere interactions, respectively.

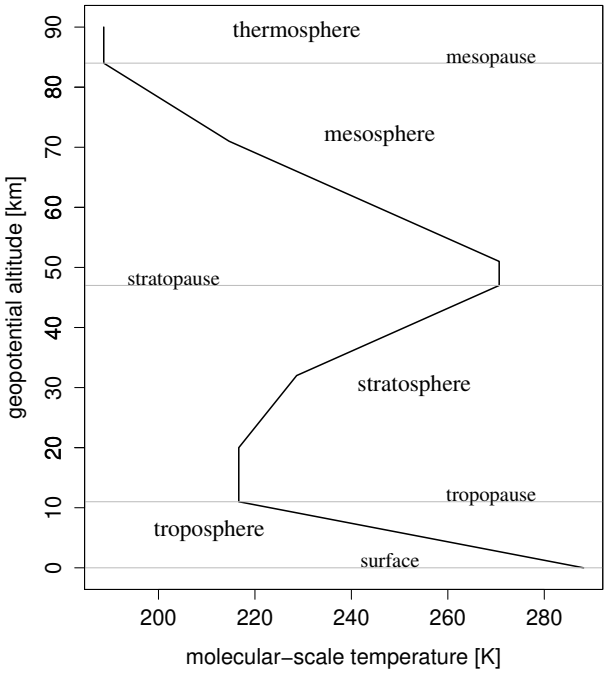

Fig. 6: Atmospheric mean temperature profile in midlatitudes (US standard atmosphere 1976)

A detailed introduction of stratosphere and troposphere is presented in the following paragraphs including dynamical features of each layer as well as interaction processes between both layers. The underlying goal is to present characteristics of both layers which may indirectly or directly affect stratospheric ozone concentration and cloud development with both processes being able to strongly modulate the amount of surface UVER.

The troposphere

The troposphere stretches from the earth's surface up to the tropopause (Fig. 6) being located at height levels between 10 and 16 km depending on latitude and season (e.g. Palmén and Newton 1969). Furthermore it contains 85% of the atmospheric mass and close to 100% of the atmospheric water (Holton 2004). The mean vertical tropospheric temperature profile is characterized by a negative lapse rate reaching to the upper tropospheric boundary which is characterized by a pronounced temperature inversion. The altitude of the inversion layer's lower boundary is often defined as the tropopause height

(Rieckh et al. 2014). According to WMO (2017) the first tropopause is defined as the altitude with a lapse rate lower than 2 $K\ km^{-1}$ under the condition of an average lapse rate being lower than 2 $K\ km^{-1}$ for the subsequent 2 km thick layer on top. The second tropopause is identified, also based on the previously given thermal definition (WMO 2017), for an average lapse rate being greater than 3 $K\ km^{-1}$ within a 1 km thick layer above the first tropopause. As alternative, the tropopause is often dynamically defined based on the PV conservation for large-scale adiabatic flow regimes with a threshold of 2 PVU (with 1 potential vorticity unit $(PVU) = 10^{-6} m^2 K s^{-1} kg^{-1}$; Stohl et al. 2003). According to Bethan et al. (1996) the strong change in ozone mixing ratio (OMR) as well as its corresponding vertical gradient (GOMR) can also be used to define the tropopause height. Hereafter the following three criteria define the tropopause height: GOMR larger than 60 $ppbv\ km^{-1}$ with the OMR being larger than 80 $ppbv$ and instantaneously larger than 110 $ppbv$ on top of the tropopause.

The strong atmospheric stability characterizing the temperature inversion at the troposphere top prevents unhindered vertical airmass exchanges with the stratosphere, except for processes described as stratosphere-troposphere exchange (STE) being discussed in a following paragraph. The lower troposphere is strongly influenced by frictional processes as part of earth-atmosphere interactions. Major consequences of surface friction are the development of the atmospheric boundary layer (ABL) and horizontal ageostrophic air flows causing mass fluxes from high to low pressure systems, for example. ABL processes can have a strong influence on our daily lives due to valley winds in mountainous regions, a strong visibility reduction during fog events and strong cooling close to the earth's surface under clear and stable conditions (Garratt 1994). The land surface ABL character can be subdivided into three different types with respect to the vertical temperature gradient named stable, neutral and unstable. A stable ABL (SBL) forms due to radiatively induced surface cooling during the night causing a near-surface inversion (Mahrt and Vickers 2006) often accompanied by a low-level jet (Davies 2000). Another mechanism causing SBL development can be warm air advection at medium tropospheric levels (Kraus and Ebel 1989). The unstable boundary layer develops due to radiatively induced surface heating leading to a super-adiabatic lapse rate near the surface (unstable character) justifying this type of boundary layer to be called the convective boundary layer (CBL). A cloud topped CBL (CTBL) downward convection is induced by radiative cooling at the cloud tops lowering the surface Bowen ratio (Stevens 2007).

The stratosphere - part of the middle atmosphere

The middle atmosphere stretches from the tropopause top up to roughly 100 km containing two separate atmospheric layers named stratosphere and mesosphere with the latter extending from the stratopause top to the mesopause being located between 80 and 100 km. (Holton 2004). The stratosphere stretches from the tropopause up to the stratopause which is located at about 50 km height (Fig. 6). Due to its strong latitudinal dependency the tropopause level ranges from between 6-8 km up to between 16-18 km at polar and tropical latitudes, respectively (Stohl et al. 2003). Hoskins (1991) introduced an approach to subdivide the atmosphere into three different parts according to the respective potential temperature (Θ) distribution. Hereafter, the 'Overworld' is defined as the atmospheric part characterized by isentropic surfaces always being located above the

tropopause. The 'Middleworld' contains isentropic surfaces crossing the tropopause but not reaching the Earth's surface. Finally, the atmospheric regime being characterized by ground-reaching isentropes is called the 'Underworld'. Thus, the stratosphere is part of the 'Overworld' being located per definition above the tropopause. A major stratosphere characteristic is the stable stratification expressed by a mean air temperature increase reaching up to the stratopause (Fig. 6). The reason for this inverse vertical temperature profile results from ozone absorption processes causing significant heat emission in the middle and upper stratosphere. The process of ozone absorption including basic ozone chemistry will be described in more detail in the next chapter (2.4).

The stratospheric circulation is mainly dynamically driven leading to higher temperatures in midlatitudes and lower temperatures in the tropics compared to the radiative equilibrium, respectively (Holton 1990). According to Holton (1990) this leads to diabatic heating and a net upward mass flux occurs in the tropics, whereby a downward mass flux accompanied by diabatic cooling occurs in the midlatitudes. Danielsen (1968) already suggested these circulation characteristics with air entering the stratosphere at low latitudes by comparing measured and estimated ozone, PV and radioactivity amounts. Thus, the midlatitude dymanical forcing, also referred to as the extratropical suction pump (Holton et al. 1995), drives the upward motion in the tropical stratosphere by pushing air poleward and back into the troposhere. The basic driving mechanism for the pumping is the Earth's rotation inducing large-scale eddies, for example Rossby waves (Holton et al. 1995). Breaking upward moving Rossby waves feed the global stratopheric circulation often being referred to as wave-driven circulation (Hoskins 1991) leading to ozone transport to higher latitudes (Haynes et al. 1991). In addition, due to the interaction of resonant Rossby waves zonal flow can be generated (Burzlaff et al. 2008).

Another stratospheric feature is the aerosol layer at height levels between 18 and 23 km (Junge et al. 1961). The layer's composition and spacial extension was elaborated based on aerial measurements conducted by balloons and planes. The results indicate a global and persistent aerosol layer consisting of particles with radii between 0.1 and 2 μm (Junge et al. 1961). Regarding its composition these measurements also indicate sulfur to be the main chemical element with relative concentrations of 85%. Further elements like silicon, aluminum, iron with relative concentrations below 10% and trace concentrations of chlorine, calcium and some more substances were detected. Junge et al. (1961) suggested the aerosol layer to be formed within the stratosphere. In their opinion both an extraterrestrial origin as well as a particle input from the troposphere could be ruled out due to the aerosol nature. Recent studies indicate the aerosol input originating from volcanic eruptions and the troposphere (McConnell and Jin 2008).

Stratospheric air can enter the troposphere through tropopause folds and then subsequently being mixed with environmental air as indicated by potential vorticity (PV) changes along its path (Danielsen 1968). In general, cross-tropopause exchange occurs either in form of troposphere to stratosphere exchange (TSE) or stratosphere to troposphere exchange (STE) with corresponding upward (Tropics) and downward net mass fluxes in the subtropics, the midlatitudes and the Arctic with a strong zonal variability (Wernli and Bourqui 2002). Deep exchange which is characterized by fast vertical airmass advection either into the troposphere down to about 700 hPa or up into the lower stratosphere (originating from lower tropospheric levels) occurs mainly during extratropical cyclogenesis with TSE maxima being localized in the western Atlantic region and the central Northwest Pacific during the boreal winter period, respectively (Wernli and

Bourqui 2002). According to Bourqui (2006) STE also occurs due to baroclinic wave breaking accompanied with a complex stratospheric air distribution entering the troposphere. This is also suggested by Holton et al. (1995) with STE taking place due to cut off cyclones or PV streamers with the low tropopause being phased out convectively, radiatively or due to turbulent mixing along the jet stream or the tropopause folding. On a global scale maxima in STE events occur along the mountain ridges of USA and Canada, the highlands of Tibet and the Andes (Škerlak et al. 2014).

Teleconnections between the Arctic and the Tropics result from meridional temperature variations which originate from the warming of the Arctic troposphere due to major mid-winter warmings (MMWs). According to Labitzke and Kunze (2009) the 11-year sunspot cycle (SC) also affects these teleconnections. As an example, the connection between the equatorial Quasi-Biennial oscillation (QBO) and northern stratospheric vortex, also being referred to as the Holton-Tan relationship (Lu et al. 2014), independently modulates the SC related signal (Camp and Tung 2007). Sudden stratospheric warming (SSW) events are another stratospheric phenomenon with major impact on the stratospheric circulation being characterized by a pronounced temperature increase in the middle and upper stratosphere amounting up to 40 K within several days. According to Maury et al. (2016), there exist two SSW types: The so-called vortex breakdown characterizing a major SSW event and the strong vortex deceleration which is typical for a minor SSW event. Butler et al. (2015) also identified two types of SSW events which is either a significant shift of the polar vortex away from the pole or a polar vortex split. The trigger leading to SSW events are planetary waves propagating upward from the troposphere and subsequently cause a strong downward feedback over several weeks (Baldwin and Dunkerton 2001) which may result in a negative North Atlantic Oscillation (NAO) period, for example (Thompson et al. 2002). SSW events also play an important role in causing strong ozone mini-holes by enhancing the lower stratospheric ozone loss due to meteorological influences as a SSW related polar vortex shift is accompanied by low ozone concentrations in the middle stratosphere (Keil et al. 2007). Compared to the southern hemisphere the larger number of SSW events on the northern hemisphere leads to a stronger ozone variability as the ozone depletion region is coupled to the stratospheric vortex area (Schoeberl and Hartmann 1991; Zhang et al. 2018). Waugh et al. (2017) highlight the differences between the two polar vortices, i.e. the tropospheric and the stratospheric polar vortex: The tropospheric polar vortex exists throughout the year while the stratospheric vortex occurs in the winter half-year of each hemisphere. Regarding the dynamical variability, the stratospheric polar vortex shows no synoptic-scale perturbations being generated by topographic influences in contrast to the tropospheric polar vortex but it can indirectly affect the tropospheric weather while being strongly disturbed und thus weakened (Waugh et al. 2017). Hartman et al. (2000) suggest a feeback mechanism of stratospheric ozone depletion and global warming which may subsequently lead to pronounced changes in the Earth's climate. A greenhouse gas (GHG) feedback is also suggested by Butchart et al. (2000). They showed a CO_2 increase to be able to overcompensate dynamical forcing from increased troposheric wave intrusion into the stratosphere by additional radiative cooling consequently leading to a more stable polar vortex, at least in the Southern hemisphere. In addition, Rind et al. (2002) showed that changes in CO_2 concentrations increase planetary wave penetration from the troposphere into the stratosphere leading to a strengthened trace gas transport into the lowest stratosphere. In relation to both the respective QBO phase and solar forcing, this may affect the Arctic oscillation in the troposphere.

2.4 Stratospheric ozone and ozone mini-holes

Global stratospheric ozone distribution

The general stratospheric circulation is characterized by a dynamical airmass advection from lower to higher latitudes (Brewer 1949). Thus, ozone being produced in the tropical stratosphere is transported poleward leading to generally higher ozone concentrations at higher latitudes (Fig. 7). The TOC seasonal pattern for Spain, for example, with higher (lower) ozone concentrations in springtime (autumn) is therefore in accordance with the global stratospheric ozone distribution (Sola and Lorente 2011). The mapping of a two-

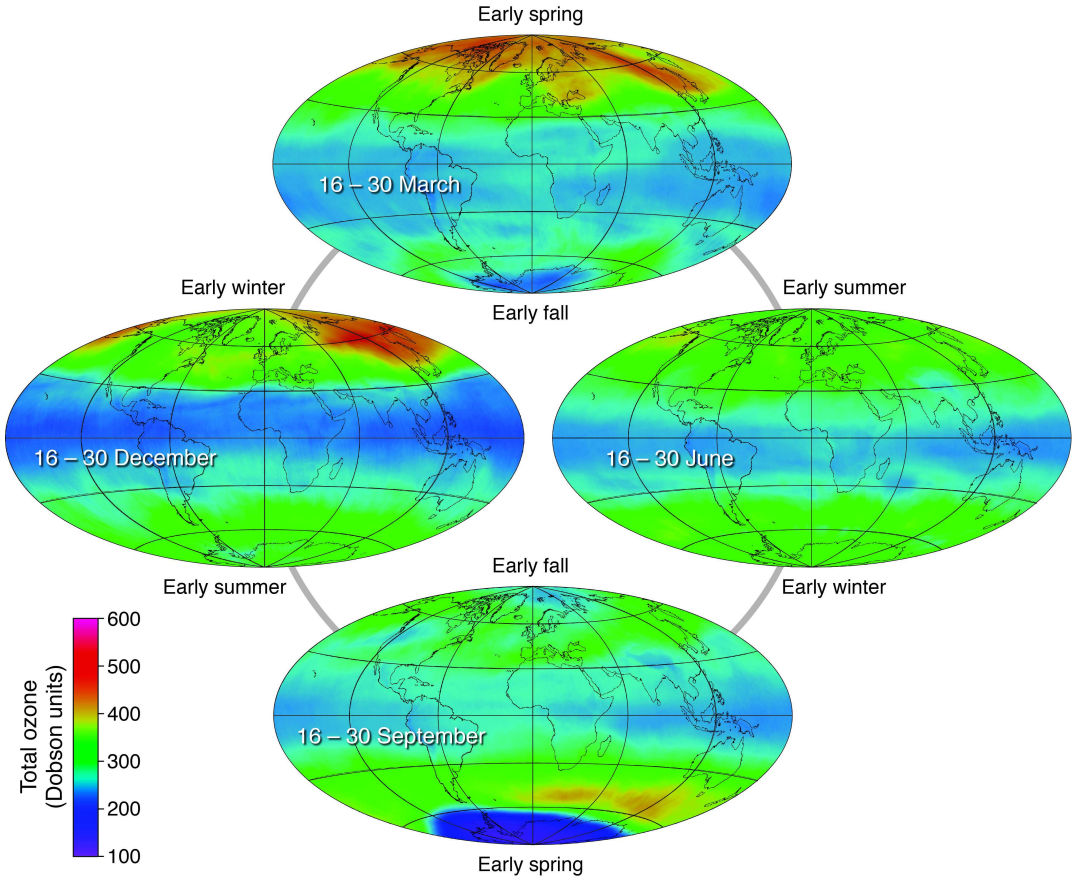

Fig. 7: Satellite data of global ozone distribution in 2009 (WMO Global Ozone Research and Monitoring Project - Report No. 52).

week mean satellite ozone data set during each season of 2009 highlights the structure and annual variations of the stratospheric ozone distribution (Fig. 7). Throughout the year, on a global perspective, the ozone concentrations are lowest in tropical regions and highest close to the respective poles due to the Brewer-Dobson circulation as briefly described above. In the tropical stratosphere the ozone contents amount close to 300 *DU* or below. The closer to the respective pole the higher the ozone concentration, in general, with a northern hemisphere maximum (minimum) in early spring (fall). There is one obvious exception occurring during the early southern hemispheric spring which is the Antarctic ozone hole being discussed later in more detail. The reason for higher ozone contents

in the early spring time of each hemisphere is the dynamically induced stratospheric circulation being much stronger during winter time of the respective hemisphere. In the early fall, after a summer period with generally less atmospheric dynamics, the midlatitude stratospheric ozone concentrations reach their annual minimum.

Ozone formation

To a large extent the amount of ultraviolet radiation reaching the earth's surface is determined by the total ozone content of the atmosphere. A large portion of the atmospheric ozone concentrates in the stratospheric ozone layer (Fig. 8) generated by the interaction

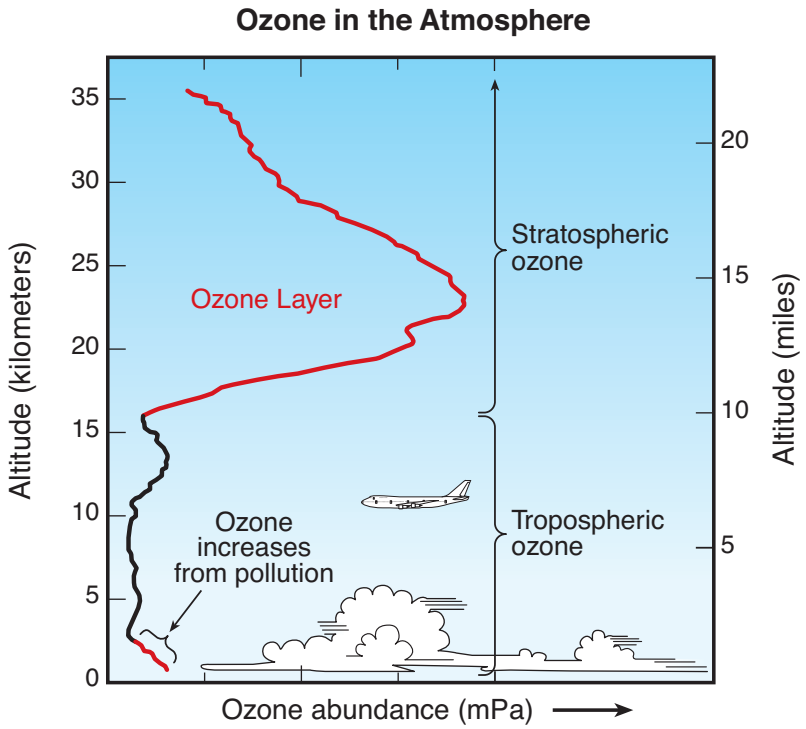

Fig. 8: Schematic atmospheric ozone profile (WMO Global Ozone Research and Monitoring Project - Report No. 52)

between high-energetic parts of the incoming solar radiation, i.e. UV-C and parts of UV-B radiation, and atmospheric oxygen molecules. The stratospheric ozone content is commonly expressed in Dobson Units (DU) being defined as the ozone layer thickness in 10^{-3} cm for a temperature of 273.15 K and an air pressure of 1 atmosphere or 1013.25 hPa (Schwartz and Warneck 1995). Thus, under standard conditions a 300 DU total ozone content equals to a 3 mm thick ozone layer. Another unit being commonly used is milli-atmospheres centimetres ($matm\ cm$) with 1 $matm\ cm = 1\ DU$ (Eisinger and Burrows 1998). In order to understand the basic interaction between solar radiation and atmospheric oxygen, the formation process of stratospheric ozone is described in the following paragraphs. The incoming solar radiation induces photolytic splitting of oxygen molecules (O_2) into oxygen atoms (O) expressed by the following chemical reaction equation (Chapman 1930; Solomon 1999)

$$O_2 + h\nu \rightarrow O + O \qquad \lambda < 250\,nm \tag{2.20}$$

with the photon energy h, its frequency ν and wavelength λ. Subsequently the O-atoms react with ambient O_2-molecules forming into ozone (O_3). This chemical reaction is the main formation process of stratospheric ozone being described by the subsequent chemical relation:

$$O + O_2 + M \rightarrow O_3 + M \tag{2.21}$$

with M denoting the concentration of air molecules (Chapman 1930; Solomon 1999; McConnell and Jin 2008). At the same time the produced ozone (c.f. equation 2.21) is often instantaneously splitted into O_2 and O by the high-energetic solar radiation via the following reaction:

$$O_3 + h\nu \rightarrow O_2 + O \tag{2.22}$$

According to McConnell and Jin (2008) this permanent O_3-O interaction can be summarized by introducing a new species called odd-oxygen ($O_x = O_3 + O$). If a (stable) O_2 molecule is formed the respective odd-oxygen vanishes consequently.

Most stratospheric ozone is produced over tropical latitudes at about 40 km height but, however, being chemically unstable and thus of short-lived nature (McConnell and Jin 2008). At altitude levels between 20 and 30 km, on the contrary, the produced ozone is chemically stable enough to be advected to higher latitudes by the general stratospheric circulation as indicated by Canadian Middle Atmosphere Model (CMAM) simulations (de GrandPré et al. 2000), for example. Because of the lack of short-wave (high-energetic) UV-C radiation at altitude levels below 20 km, photoloytic processes do not take place.

$$CO + 2O_2 \rightarrow CO_2 + O_3 \tag{2.23}$$

Instead, as expressed by equation (2.30), the O_3-formation process in the lower stratosphere and the troposphere is mainly driven by the oxidation of carbon monoxide (CO) with nitrogen monoxide (NO) serving as catalyst (McConnell and Jin 2008).

Stratospheric ozone destruction

Ozone destruction in the stratosphere results from both natural and man-made influences (McConnell and Jin 2008). Natural impact affecting the stratospheric ozone content arises for example from volcanic eruptions being responsible for a significant aerosol input into the stratosphere. Major anthropogenic influences on stratospheric ozone result from the emission of chemical substances leading to the generation of photoactive radicals, like chlorofluorocarbons for example (Solomon 1999). The impacts just introduced show both latitudinal as well as seasonal variabilities which will be discussed in the following paragraphs.

Chemical substances like the radical species HO_x, NO_x, BrO_x and ClO_x[1] are mostly generated in the stratosphere by photolysis or the chemical reaction with already existing free radicals, like the oxygen atom for example (McConnell and Jin 2008). Another example is stratospheric chlorine being produced by the oxidation of man-made hydrocarbons with chlorine components (McConnell and Jin 2008; Brasseur and Solomon 2005). The basic substances needed for the radical synthesis, like water (H_2O) and nitrous oxide (N_2O), originate from biological sources in the troposphere being transported into the stratosphere. By interaction with high-energetic solar radiation these substances are

[1] The subscript x refers to a variable number of oxygen atoms within the radical molecule or ion.

transformed into reactive molecules subsequently. In addition, solar proton events (SPE) may cause significant enhancements in the stratospheric odd-nitrogen concentration subsequently leading to an ozone depletion in the upper stratosphere amounting up to 10% (Jackman and Fleming 2000). According to Randall et al. (2007) the SPE induced ionization and dissociation processes take place in the thermosphere and mesosphere with the particles subsequently decending into the stratosphere. This process is also being referred to as energetic particle precipitation (EPP). The EPP indirect effect (EPP IE) takes place in the polar stratosphere at latitudes higher than 60° on both hemispheres affecting the stratospheric ozone chemistry for months and years (Jackman et al. 2007). Baumgaertner et al. (2010) derived an improvement for the ECHAM5/MESSy model by introducing a new parameterization which includes a height dependency of the nitrogen or NO production thus taking the SPE related particle concentration into account. Rohen et al. (2005) investigated an ozone depletion event in 2003 with ozone decreases up to 50% in the Northern Hemisphere governed by two different ozone depletion regimes (HO_x and NO_x) occurring at the same time.

According to McConnell and Jin (2008) the major ozone depletion reactions in the upper stratosphere are described by parts of the Chapman cycle (cf. eq. 2.22) and a more generalized reaction equation expressing the net reduction from O_3 to O_2 via atomic oxygen. As the amout of atomic oxygen strongly decreases with increasing air pressure (McConnell and Jin 2008) the principal chemical reactions leading to ozone reduction in the lower stratosphere include OH ions as well as chlorine/bromine oxide. Importantly, the OH ions or the chlorine/bromine oxide molecules, are reformed at the end of the respective reaction cycle thus being able to perfom several ozone destruction cycles successively.

The substances nitric acid, chlorine nitrate or hydrochloric acid are storage forms for ozone depleting molecules or atoms, often being referred to as radical reservoirs. These reservoir substances are chemically inactive with respect to ozone thus being able to temporarily remove NO_x and ClO_x from the ozone destruction cycles introduced above. An important principle in order to better understand the ozone depletion chemistry is called partitioning chemistry distinguishing between ozone destroying chlorofluorocarbons (CFC) like chlorine and the inactive fluorine (Solomon 1999). Ozone depletion in the stratosphere at midlatitudes also occurs due to particle chemistry with particles being of volcanic origin (Solomon 1999). Evidence was provided by investigating the Mt. Pinatubo eruption with liquid aerosols affecting both the chlorine and nitrogen partitioning chemistry being enhanced by higher water vapor contents in the lower stratosphere. In addition, the midlatitude ozone distribution is also affected by the polar ozone losses resulting in a transient ozone layer thinning, for example.

In the southern hemisphere the term „Antarctic ozone hole“ refers to a pronounced ozone content decrease in the polar stratosphere which was first discovered in the 1980s (Farman et al. 1985). Stolarski et al. (1986) confirmed these findings with their satellite measurements also indicating the ozone depletion to be confined to the Antarctic continent. The Antarctic ozone hole finally develops due to the ClO catalyst which originates from anthropogenic emission. The formation of polar stratospheric clouds (PSC) as activator for ozone depletion chemistry (clorine) occurs due to the low temperatures in the polar stratosphere ($\sim$ 200 K) during the Antarctic winter and spring time. PSC develop based on stratospheric aerosols and the subsequent water condensation resulting in different cloud types, like supercooled ternary solutions (STS) or the nitric acid cloud

type. According to Solomon (1999) PSCs consist mainly of water ice, nitric acid hydrates as well as of water, sulfuric acid and nitric acid solutions. Heterogeneous chemistry at PSC surfaces leads to the activation of chlorine from HCl and $ClONO_2$ reservoirs. Thus, strong ozone depletion occurs in spring when the first sun rays reach the PSCs and trigger the ozone destruction process. PSC chemistry contains adsorption of radical reservoir molecules into existing liquid or ice surfaces. Crutzen and Arnold (1986) proposed a chemical reaction with OH and HCl forming ClO_x molecules which subsequently cause severe stratospheric ozone depletion. The strength of an ozone depletion event can be determined by the amount of nitrogen content being lost by denitrification which causes a stronger ozone loss despite the decreasing chlorine-based ozone depletion (McConnell and Jin 2008). Denitrification causes more ozone depletion due to a persistent removal of HNO_3 in form of PSC particle sedimentation (Chipperfield and Pyle 1998) and therefore active chlorine is not bound into substances like $ClONO_2$ but stays active instead. In addition, nitrogen can be reduced by denoxification which is the creation of a transient NO_x reservoir by forming HNO_3 at aerosols (Waibel et al. 1999). Thus, both the NO_2 inhibition as well as the chlorine activation lead to a more steady and less temperature dependent ozone destruction process. Measurements indicate the loss in polar stratospheric ozone to mostly occur at height levels between 10 to 20 km (Solomon et al. 1986). During the Antarctic summer period, on the other hand, higher ozone concentrations result from the changed stratospheric wind regime due to radiative heating (Stolarski et al. 2006).

Aerosol effects must be considered as well as other factors like the recent ozone loss in the arctic stratosphere which may influence the total stratospheric ozone distribution recovery. The Arosa ozone time series strongly shows the relation of midlatitude ozone content and aerosol concentration suggesting a strong ozone depletion in midlatitudes occurring for another strong volcanic eruption despite a significant chlorine decrease (see Solomon 1999). Earlier studies (e.g. McKenzie et al. 2011) were convinced of the successful Montreal protocol implementation projecting an ozone layer recovery until the midst of the 21 century. Having analyzed reanalysis data from 1998 - 2016 Wargan et al. (2018) also suggested the increase in upper stratospheric ozone being accompanied by a slight ozone concentration decrease in the lower stratosphere due to circulation changes to be attributed to the Montreal protocol (Montreal protocol 1987) implementation. According to Montzka et al. (2018), however, new measurements show a slowed decline of atmospheric chlorofluorocarbon (CFC) concentrations indicating possibly illegal CFC emission into the atmosphere contradicting the goals which have been agreed to in the Montreal protocol. Without this protocol the amount of UV irradiance at midlatitudes was expected to be three times as large with all the negative consequences on the environment and human health. Thus the new results of Montzka et al. (2018) highlight the urgence for action regarding the complete phase out of CFC chemicals. The major source for large portions (40 - 60%) of the newly emitted CFC-11 concentrations can be located to eastern China as indicated by Rigby et al. (2019).

The stratospheric ozone content also depends on the atmospheric CO_2 concentration being known as an effective greenhouse gas. Model simulations with a four times enhanced CO_2-content result in an ozone decrease in the lower stratosphere, whereas almost no change occurs in the higher stratosphere and an ozone content increase has to be expected over higher latitudes which is characterized by a strong seasonal dependency (Chiodo et al. 2018). More CO_2 in the stratosphere, especially at middle and higher stratospheric levels, induces cooling up to 12 K at stratopause height which is counter-

acted by an ozone-related radiative response due to ozone mixing-ratio increases up to 20% in the stratosphere and 15% in the lower mesosphere (Jonsson et al. 2004). This chemical response results from the temperature dependency of the odd oxygen formation process which was previously introduced.

Ozone mini-holes - meteorological impact on the ozone column

Low-ozone events, also referred to as ozone mini-holes (Newman et al. 1988), result from meteorological impact on the atmospheric ozone column which mostly occurs in form of large-scale tropospheric anticyclones. In addition the anticyclonic regime is also responsible for a strong reduction or dissipation of clouds during most low-ozone events (Sola and Lorente 2011). McCormack and Hood (1997) define an ozone mini-hole to occur for total ozone contents below 300 DU lasting for few days over a specific region. According to Newman et al. (1988) ozone mini-holes are short-term (1-5 days) but significant total ozone reductions of at least 20 DU within 24 hours. They also stated ozone mini-holes to be accompanied by large-scale anticyclones on their western edge with a positive PV anomaly on the eastern side, a negative temperature anomaly in the lower stratosphere and being characterized by diameters roughly stretching between 1000 and 3000 km.

Corresponding to the large-scale circulation at the western anticyclone edge vertical uplift leads to an upward displacement of the lower stratosphere accompanied by the advection of low-ozone content tropospheric airmasses from lower latitudes consequently leading to a lower total ozone column to the north-west of the surface anticyclone (Reed 1950; Rood et al. 1992). According to Peters et al. (1995) the poleward advection of air masses from subtropical origin is strongly correlated to a potential vorticity minimum near the tropopause supporting the suggestion made by Newman et al. (1988). According to Canziani et al. (2002) the mechanism leading to transient low-ozone periods in the UT/LS (upper troposphere/lower stratosphere) region is characterized by an upward shift of the tropopause combined with a strong pressure gradient at the tropopause level. This is confirmed by a study of Antón et al. (2007) having investigated a strong low-ozone event which occurred in conjunction with a pronounced blocking anticyclone on 10 January 2004. For this case, a combination of low-ozone tropical airmass advection and a fast vertical tropopause uplift caused a 33% ozone decrease compared to the monthly mean. Here, the emphasis of a 'fast' vertical uplift is a concretisation compared to the previously mentioned suggestions (Reed 1950; Newman et al. 1988 and Rood et al. 1992). As stated by Hoinka et al. (1996) a change in tropopause height of 1 km (either upward or downward) is related to a 13 DU ozone content change which also supports the theoretical approaches given in the previously mentioned studies. Another study presenting an analysis of sounding data collected during low-ozone events at Hohenpeissenberg observatory (1966-99) shows a 60% loss in lower stratospheric ozone content due to a 50 hPa tropopause height elevation (Krzyścin 2002). The adiabatic uplift strongly contributes to both, the ozone loss and the temperature drop in the lower stratosphere as a result of the anticyclone correlated tropopause height elevation (Pérez et al. 2002; Reed 1950). According to Martínez-Lozano et al. (2011) ozone mini-holes are strongly correlated to anomalies in the vertical temperature profiles of both the upper troposphere (positive) and the lower and middle stratosphere (negative). By investigating the dynamical processes temporarily causing a drop in stratospheric ozone content Iwao and Hirooka (2006)

quantified the contributions of dynamical isentropic advection of low-ozone air masses close to the tropopause and the loss of ozone-rich air in the middle stratosphere due to the vertical uplift of isentropes to be equally large. Millán and Manney (2017) performed an investigation of ozone mini-holes represented in reanalysis data which shows a strong underestimation (34 to 83%) of the total number of mini-holes indicating a model weakness regarding the driving dynamical processes previously introduced. Ozone sonde measurements also indicate the major ozone loss during an ozone mini-hole period to occur in the lower stratosphere between below 20 km and the tropopause (Allaart et al. 2000). In the southern hemisphere only, low-ozone events are additionally caused by short-time displacements of the polar vortex being accompanied by the advection of very low-ozone content stratospheric airmasses resulting from the chemical ozone depletion processes within the polar vortex. Pérez et al. (2000) highlighted that a combination of the Antarctic ozone hole and vertical motions may lead to a decrease of (southern) midlatitude total ozone contents. The impact of extreme low or high total ozone on the seasonal mean ozone column can amount up to $\pm$ 5% (Petropavlovskikh et al. 2015).

There are currently two major theories to explain the development of ozone mini-hole events being briefly presented in the following: The first mechanism (localized upwelling hypothesis) focuses on vertical uplift corresponding to a reduced ozone layer thickness in the stratosphere due to a pronounced tropospheric anticyclogenesis (Teitelbaum et al. 2001). The second mechanism, known as far-range transport hypothesis, explains the generation of low-ozone stratospheric air by meridional transport from the tropics in the lower stratosphere (340-440 K) and from high latitudes in the middle stratosphere (530-700 K) (Koch et al. 2003). Thus, a low-ozone air column develops locally due to the advection of ozone poor air from regions being characterized by a climatologically low ozone content (Koch et al. 2002). By means of synoptic and backward trajectory analysis the results found by Bojkov and Balis (2001) also indicate the second mechanism to be mainly responsible for the formation of an ozone mini-hole, however, sometimes in conjuction with mechanism one, which is the upward lifting of low-ozone tropospherical air. They concluded by indicating an ozone mini-hole event to be the result of a hemispheric ozone redistribution instead of resulting from a 'real' depletion which occurs for the Antarctic ozone hole, on the contrary. Strong low-ozone events may develop when low-ozone stratospheric airmasses originating from the polar vortex and anticyclonically forced uplift of tropospheric airmasses subsequently causing low-stratospheric divergence lead to a combined total ozone column (TOC) reduction for a certain region (James et al. 1997). Hereby, the movement of stratospheric air occurs during a shift of the polar vortex characterizing a sudden stratospheric warming event (Keil et al. 2007).

The definition for ozone mini-holes is based on the respective monthly climatologic mean ozone content due to seasonal and long-term variabilities (Sola and Lorente 2011). For Barcelona Sola and Lorente (2011) found most ozone mini-holes to occur during winter and spring time. Their results are in accordance with the findings of James (1998) also suggesting a strong seasonal variability with most events occurring in the winter period. Bojkov and Balis (2001) identified an increased number of strong low-ozone episodes in the last decades being characterized by ozone decreases below 220 DU having compared total ozone amounts for two time periods stretching from 1957-1978 and 1979-2000, respectively. Their results are supported by a comparison total ozone data of two time periods ranging from 1952 to 1963 and from 1990 to 2000, respectively, with a much higher LOD (low ozone days: TOC below 225 DU) frequency occurring during the second time inter-

val (Brönnimann and Hood 2003). As a possible reason for this, they identified changes in both atmospheric dynamics as well as in the mean ozone column to have stong impact on the LOD abundance with a larger uncertainty for the latter effect. McCormack and Hood (1997) also found an increased number of ozone mini-holes having occurred during the 1980s. Rieder et al. (2010) investigated the occurrence of days with extreme low and high total ozone content based on extreme value theory. Using data from Arosa, they also found an increased number of extreme low ozone events and, due to the statistical approach, more information regarding dynamical or chemical impacts on the TOC variability. This statistical approach was also applied to identify periods with extreme TOC over Thessaloniki (e.g. Fragkos et al. 2016) resulting in 12(15)% of the days being characterized as low(high)-ozone events, respectively.

The significant decrease in stratospheric ozone content characterizing an ozone mini-hole leads to a significant increase of surface UVER as the absorption of shortwave radiation is reduced. The influence of UVER on human health will be discussed in chapter 2.7 in more detail. The following examples highlight both the amount of ozone decrease and the increase of surface UVER which may occur during low-ozone events. The 2011 Arctic ozone depletion event with total ozone reductions reaching about 15% in midlatitudes and up to 40% in the Arctic caused a midlatitude midday UV erythemal dose increase of 3-4 SED (Petkov et al. 2014). Another significant winter time UVER dose increase occurred on 10 Januar 2004 during a strong low-ozone event. This event is characterized by surface UVER increases of 43% and 75% compared to the same day in 2003 and 2005, respectively (Antón et al. 2007). Also in 2004, Martínez-Lozano et al. (2011) identified low-ozone events over the Valencia region with TOC decreases up to 39% leading to a respective 49% UVER increase. In order to quantify the increase in surface UVER being related to the total ozone decrease Madronich (1993) introduced the radiation amplification factor (RAF) being defined as

$$\frac{UV_1}{UV_0} = \left(\frac{TOC_1}{TOC_0}\right)^{-RAF} \tag{2.24}$$

with $UV_{0,1}$ referring to measured or estimated UV irradiances or related doses of two consecutive days as denoted by the index 0 or 1, respectively. Schwarz et al. (2018) introduced another factor, called the anomaly amplification factor (AAF), which is the slope of the regression line obtained by relating total ozone column to UV index (UVI) anomalies from the same event. Thus the AAF can be utilized to relate extreme values in TOC to extreme values in UV-B radiation at the surface.

Depending on their origin, the tropical air masses may also contain large amounts of aerosols additionally attenuating the incoming solar UVER (Marínez-Lozano et al. 2011). As measured on the island of Lampedusa, for example, aerosol particles eing advected from the Sahara desert due to large-scale anticyclonic circulation pattern led to a 25% reduction (SZA = 60°) of measured 350 nm irradiance. These results clearly highlight the significant aerosol impact on surface UVER for special meteorological conditions (di Sarra et al. 2002). Liu et al. (1991) estimated the aerosol impact on the amount of surface radiation resulting in a 5 to 18% decrease of biologically active UV-B radiation. Their results suggest a partial or complete compensation of the surface UVER increase caused by low stratospheric ozone contents in the northern hemisphere. Desert dust may lead to a direct UV irradiance decrease up to 55% but to a 40% increase in the diffuse UV radiation part due to intense Mie scattering (Román et al. 2013). Fragkos et al. (2016)

found the variability of noon UVER during clear and extreme low ozone conditions to be mainly determined by the amount of aerosols which can be expressed by the aerosol optical depth. For these events the high aerosol amounts partially compensated the UVER increases caused by low TOC. In addition, Fragkos et al. (2016) suggest a seasonality with a stronger aerosol impact in spring and summer probably caused by more effective aerosol characteristics.

2.5 Clouds and solar radiation

Cloud development occurs for supersaturated air with the condensation occurring at small aerosol particles serving as cloud condensation nuclei (CCN) or ice nuclei (IN) (e.g. Fan et al. 2016). The supersaturation reaches values up to 7% relative humidity within the inner parts of a cumulus cloud whereas in its outer parts the relative humidity may decrease to 70% due to mixing processes (Pruppacher and Klett 1997). The characteristics of clouds are determined by updraft velocities, microphysical processes and the aerosol particle constitution.

More aerosol particles in warm clouds, for example, strongly increase the cloud reflection due to a higher droplet number (Twomey 1977). Another study also highlights the strong aerosol impact, or more general expressed as air pollution, being able to almost completely inhibit warm clouds from precipitating (Rosenfeld 1999). Furthermore, aerosols can impact the heterogeneous nucleation by affecting ice crystal number concentration and size distribution (Fan et al. 2016). Scattering and absorption of solar radiation by aerosols, also known as aerosol-radiation interaction (ARI), can have significant influence on the atmospheric stratification. Strong aerosol induced scattering may lead to reduced surface temperatures, for example, whereby aerosol induced heating results in significantly increased absorption (Peng et al. 2016b). In general, ARI can be seen as the most important relationship affecting atmospheric and climate variability (Hu et al. 2017; Boers et al. 2017).

Cloud particles cover a broad size spectrum ranging from $\geq 10^{-2}\mu m$ (CCN particles) up to $\leq 10^{4}\mu m$ and $\leq 10^{5}\mu m$ for raindrops and hail particles, respectively. Cumulus clouds, for example, may show very different drop size distributions depending on development stage, surrounding cloud layers and the surface type (maritime or continental environment). Non-precipitating maritime cumulus clouds contain less smaller drops but a broader drop size spectrum (5 - 45 μm) compared to continental cumulus clouds (5 - 20 μm). Fog, on the contrary, is characterized by water contents lower than 0.2 gm^{-3} and drop sizes ranging between 2.5 to 20 μm (Pruppacher and Klett 1997). On a global scale, the most frequent cloud type is (marine) stratocumulus which strongly affects the terrestrial radiation budget mostly by reflecting the incoming solar radiation (Wood 2012). The cloud effect in modulating the Earth's radiative budget strongly depends on cloud type. According to Chen et al. (2000) stratocumulus, altostratus and cirrostratus clouds predominantly act in modulating the shotwave radiative balance whereas cirrus, cirrostratus and cumulonimbus clouds act more pronounced in changing the longwave radiation budget.

The most important effects modulating solar UV radiation next to scattering of air molecules are the influences of clouds (Foyo-Moreno et al. 2001). The presence of clouds can lead to both a pronounced attenuation of solar UV radiation and a short-term increase

due to scattering processes (Mie scattering), respectively. In spring, a combination of high cloud coverage, lower stratopheric ozone but already smaller SZA may lead to UVER increases up to 25% for a 30 min time period (Wolfram et al. 2017). Extended thin cirrus cloud influence on solar radiation at the surface shows enhanced UV-B and total irradiance ($\sim$ 40 Wm^{-2}) for several hours. During broken cumulus cloudiness enhanced solar irradiance can occur for time periods smaller than 30 min, for altocumulus the time scales reach up to 140 s and may amout up to several hundred Wm^{-2} (Thuillier et al. 2013). The effect of clouds in modulating the surface solar radiation also depends on water phase (liquid, ice) and on cloud layer altitude with a weaker attenuation for both water clouds compared to ice clouds as well as low-to-midlayer clouds compared to high clouds (Xia et al. 2018). According to Foyo-Moreno et al. (2003) cloud cover lower than 3 oktas may be considered to be negligible regarding its impact on solar UV. For increasing cloud coverage the ratio of UV irradiance to total solar irradiance also increases indicating the different cloud effect on the UV spectrum in comparison to the visible spectral range or the total solar spectrum, respectively. Matuszko (2012) investigated the effect of different cloud types on solar irradiance with attenuations ranging between 30 and 800 Wm^{-2} for Cirrus and Cumulonimbus clouds, respectively. For broken cloudiness (3-6 oktas), containing the cumulus cloud types mediocris and congestus as well as Cumulonimbus clouds, the highest radiation intensities were reached. For total cloud coverage the radiation intensity varies between 40% and 80% depending on the stratus layer thickness (Matuszko 2012).

The fact that UV-B radiation is more efficiently scattered than UV-A radiation or parts of the visible spectrum is responsible for the attenuating effect of clouds being more pronounced for the UV-A and visible parts compared to the UV-B part. In order to investigate and quantify the cloud influence affecting the incoming solar UV radiation mainly two methods are used (Calbó et al. 2005): Subjective cloud observations and global radiation measurements. Based on radiation measurements the cloud modification factor (CMF) can be defined as

$$CMF = \frac{UV_m}{UV_c} \tag{2.25}$$

with the measured solar UV radiation during cloudy conditions (UV_m) and calculated clear sky UV radiation (UV_c) quantifying the cloud meteorological influence (Calbó et al. 2005). For overcast conditions CMF values range between 0.3 and 0.7 indicating a high dispersion. In general, global irradiance measurements indicate an attenuating influence related to the presence of clouds. Nevertheless for short time intervals cloud presence can have an enhancing effect on the incoming solar radiation with its magnitude being not well known yet (Calbó et al. 2005). For broken cloudiness (in this case 5-7 oktas) total and UVER irradiances are amplified up to 113% and 133% compared to clear sky conditions, respectively. Calbó et al. (2017) found CMF values of 1.6 and 1.3 for total irradiance and UV radiation (1-min resolution), respectively. Foyo-Moreno et al. (2001) showed the cloud influence on solar radiation to depend on cloud type and coverage including a spectral dependency as well.

A total clear-sky radiation (TR_{clear}) estimate can be obtained, for example, from statistical models or artificial neural networks (Barbero et al. 2006). These statistical models use daily UV and clearness indices and the relative optical air mass as input parameters. The artificial neural networks are based on daily solar global irradiation, daily global clearness index as well as the relative optical air mass. Another method is to calculate the total clear-sky radiation using the following regression-based relation (Calbó et al.

2017; Long and Ackermann 2000):

$$TR_{clear} = \frac{a}{R^2}\cos(SZA)^b \tag{2.26}$$

with the regression parameters a and b as well as the sun-Earth distance R. Due to the strong wavelength and path length dependency of the scattering efficiency the CMF values also strongly depend on wavelength and on the solar zenith angle (SZA) especially for the diffuse solar irradiance (Mateos et al. 2015). Investigations of SZA, cloud cover and ozone content independently affecting the surface UV erythemal radiation showed the SZA to be the dominant factor but cloud cover being able to cause variabilities in the surface UVER up to 50% (McKenzie et al. 1991). The amount of solar UVER reduction by clouds depends on the cloud type which can be related, for overcast conditions, to the vertical cloud level without any geographical dependency (Cede et al. 2002).

The UV radiation data estimated by means of the *TROPOMI* (*TROPO*spheric *M*onitoring *I*nstrument) product provides daily information for the UV irradiances 305, 310, 324 and 380 nm and the corresponding erythemally and vitamin-D weighted irradiances, respectively. In addition, the data can be obtained with the actual cloudiness included or as clear-sky data only (Lindfors et al. 2018). Grant and Gao (2003) developed a model to determine the diffuse UV-A and -B radiation parts for partly cloudiness based on an empirical relation of both cloud fraction and solar zenith angles.

Irradiation is a radiative quantity denoting the amount of radiative energy (for example having accumulated during one year) per unit surface. Santos et al. (2011) found the surface total solar UV irradiation (UVT) to amount 4.2% of the global solar irradiation by evaluating surface measurements from Valladolid (Spain). Hereby, the solar elevation is the major impact for UVT to be taken care of for modelling purposes. In order to investigate the effect of cloudiness on the ratio between UV and total solar irradiation (G) Santos et al. (2011) also introduced the clearness index k_t as given by the following expression:

$$k_t = \frac{G}{G_0} \tag{2.27}$$

with G_0 referring to the extraterrestrial total solar irradiation. Analogously the ultraviolet clearness index k_{tuv} can be derived based on a measured ultraviolet irradiation and the corresponding extraterrestrial UV solar irradiation. As a result Santos et al. (2011) found an increasing UV/G ratio for increasing cloudiness thus cloud influence is acting more pronounced on G than on UVT.

According to Svensmark and Friis-Christensen (1997) the global cloud cover varies between 3-4% during a solar cycle with the cloud coverage being correlated to the cosmic ray flux. During high solar activity the cosmic ray flux is weakest and vice versa (Svensmark and Friis-Christensen 1997). According to Carslaw et al. (2002) the "ion-aerosol clear-air mechanism" is the basic physical mechanism to explain the increased cloud cover for an increased cosmic ray flux subsequently causing a higher number concentration of cloud condensation nuclei (CCN). On a decadal scale the cosmic ray-cloud interaction is suggested to influence the Earth's climate by affecting decadal phenomena, like El Niño for example (Carslaw et al. 2002).

2.6 Surface UV radiation - protection and prevention measures

UV protection measures

In order to reduce the UV radiation exposure specifically for outdoor working people protection measures are necessary and mandatory according to the general german legislation concerning health and safety at work (Diepgen et al. 2014). In Germany the health insurance providers developed a hierarchical set of protection measures called the TOP principle to be applied by the employer ensuring health and security at work (dguv.de/fbhl/sachgebiete/physische-belastungen/praevention). According to the TOP principle the protection measures are generally structured into technical (T), organizational (O) and personal (P) measures (Diepgen et al. 2012):

- Technical measures include new procedures for risk prevention as well as the separation of workers from their working device using new and more enclosed machines.
- Organizational measures consist of time or access regulations to minimize the risk exposure. Regarding the UV exposure, specifically outdoor work may be avoided during noon by applying updated shift and break plans or by working off necessary indoor work.
- Trainings, instructions and personal protection equipment (safety shoes and gloves, safety glasses and clothes, etc.) are labeled as personal measures.

Natural protection from UV radiation is largely provided by the dark skin pigmentation (eumelanin) with a much higher risk for skin cancer development for fair skinned people due to the UV caused cell mutations (D'Orazio et al. 2013). According to Sklar et al. (2013) UV-A and UV-B radiation act differently within the skin layers with UV-A being responsible for immediate and persistent pigment darkening. UV-B radiation leads to erythema and a delayed tanning reaction beginning in the basal layer and moving up with the epidermis cells. Thus the exposure to UV radiation, especially for fair skinned people, should be minimized by reducing the exposure to the sun and by minimizing artificial tanning following the UV safety tips provided by D'Orazio et al. (2013).

Institutions in Germany dealing with UV radiation

In Germany the Federal Office for Radiation Protection (BfS) is responsible to inform and advice the federal government and the public concerning all radiation protection issues. The BfS is organized as a higher federal authority within the Federal Ministry for the Environment, Nature Conservation and Nuclear Safety pooling all national radiation protection competences with its head office in Salzgitter. In addition, the BfS is tracing, operating and initiating research being represented in numerous national and international committees like the World Health Organization (WHO) or the International Atomic Energy Agency (IAEA), respectively. Further tasks the BfS is dealing with are radiation risk assessment in medidal applications, enlightenment concerning UV and mobile radio

exposure in daily routine, protection of the public in case of a radiologic emergency, measurement of the environmental radioactivity, conducting the Radiation Protection Register, conduction of the register of high-radioactive sources as well as giving advice and support concerning active nuclear-specific defense by administrative assistance (bfs.de).

Since 1993 the BfS and the Federal Environment Agency (UBA) installed the first four UV measurement stations in Germany. These stations are located in Zingst, Langen, on Schauinsland mountain and Neuherberg close to Munich, respectively. In the following years the monitoring network was gradually expanded together with associated institutions namely the Federal Institute for Occupational Safety and Health (BAuA), the University of Kiel, the German Meteorological Service (DWD), the Bavarian Environmental Agency (LfU) as well as the Lower Saxony labour inspectorate. Currently the UV monitoring system comprises ten measurement sites (Fig. 9):

Fig. 9: UV measurement sites of BfS in Germany. (http://www.bfs.de)

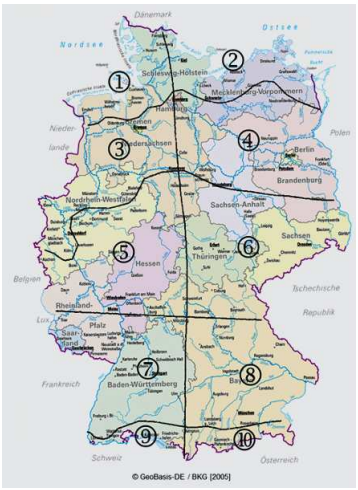

Fig. 10: UVI forecast areas in Germany. (http://www.bfs.de)

On these sites the solar UV irradiance is measured by means of spectroradiometers collecting data between 290 nm and 400 nm every 6 min. In addition pyranometers are used to collect global solar irradiance data as well. In order to provide a reasonable UV index prognosis the german territory is subdivided into ten different UV forecast regions (Fig. 10). These areas are selected based on similar climatological conditions resulting in mean UVI prognoses for each region. A number (1-10) is assigned to each region being labeled as follows (Fig. 10): The coastal area North Sea (1), the coastal area Baltic Sea (2), the North German Plain West / Bay of Cologne (3), the North German Plain East (4), the low mountain range area West (5), the low mountain range area East (6), Southern Germany West (7), Southern Germany East (8), Hochrhein / Lake Constance (9) and the Alpine area (10).

The BfS calculates the UVI prognosis based on recent UV irradiance measurements, measured UV data from past years, the total ozone concentration and a special adjusted DWD cloud cover forecast. During the seasonal time period from April to September the UVI prognoses are calculated each day as a three-day forecast product. From October to March the UVI forecast product consists of monthly maximum UVI values representing the maximum possible UVI values for clear-sky conditions. Colored numbers and protec-

tion recommendations, each corresponding to a specific UVI value range, are used as UVI forecast symbols (Fig. 11).

Fig. 11: UV index values and recommendations. (http://www.myuv.com.au)

The German Social Accident Insurance (DGUV) is the umbrella organization of the commercial employer's liability insurance associations and the public domain accident insurance providers in Germany. There are currently nine employer's liability insurance associations being assigned to specific industrial branches. The public domain accident insurance providers subdivide into 16 accident insurances, three community accident insurer associations, four fire service accident insurers as well as the accident insurance for federal and railroad affairs (UVB). For more information regarding the organization and competences of the insurance providers the reader is referred to the following link: www.dguv.de/de/wir-ueber-uns/mitglieder/index.jsp. According to its statute one major DGUV task includes the conduction, promotion and coordination of common measures and research subject to occupational injuries, diseases and health risks. For more DGUV tasks the reader is referred to the DGUV web site (www.dguv.de/de/wir-ueber-uns/aufgaben/). The inner DGUV organization is characterized by self-governance and codetermination. In the DGUV self-governance committees there is an equal number of members being elected either as representative for the employer or the employee side.

According to its organizational chart the DGUV separates into three different business units: Insurance, prevention and services. The prevention unit is subdivided into five major sections namely the staff unit prevention, the unit Safety and Health located in Sankt Augustin and Munich, the Institute for Occupational Safety and Health of the DGUV (IFA) in Sankt Augustin, the Institute for Prevention and Occupational Medicine of the DGUV (IPA) being part of the Ruhr University Bochum and the Institute for Work and Health of the DGUV (IAG) located in Dresden.

The Institute for Occupational Safety and Health (IFA)

The IFA as a DGUV research institute provides assistance to the insurance providers regarding scientific and technical topics in the range of occupational safety and health protection. The institute's main working tasks embrace the topics research, evolution and survey, inspection of products and material samples, operational measurements and advice, participation in standardization and regulation as well as providing special information and expert knowledge. In addition the IFA takes action regarding the testing and certification of products and qualitiy management systems for private companies and

manufacturers. The IFA department for radiation is, besides the Meteorological Institute of the University of Bonn, the main supporter of this research project presented in the thesis at hand by providing measurement equipment as well as access to UV data sets and campaign related partners (probands, institutes and measurement sites). Next to giving advice concerning the electromagnetic interference of active implants, the consultation regarding protection measures, performing laboratory measurements (radiation source characteristics, transmittance of filters and substances), providing expert reports in cases of occupational disease and information transfer the department's working tasks being mainly relevant for this study are:

- measurement and evaluation of radiation exposure in the workplace
- personal dosimetry

The next section includes a detailed description of the equipment provided by the IFA, the research cooperation and the measurements performed during this research collaboration.

2.7 UV exposure of different anatomical zones

An interesting research topic is about elaborating a potential relation between skin cancer occurrence and the specific solar UV exposure of anatomical zones. According to Wang et al. (2014) the risk of skin cancer strongly depends on the amount of exposure to solar UV radiation and the personal outdoor behaviour. Importantly, the body exposure to direct, diffuse and reflected UV radiation is not well known yet (Vernez et al. 2012). In order to derive adequate protection measures the dose amount of each UV part received by a specific anatomical zone would be very helpful and can be provided by model simulations based on ground irradiance measurements (Vernez et al. 2012). Wang et al. (2014) investigated the exposure of the human face to solar UV radiation being one of the most UV sensitive body parts (D'Orazio et al. 2013). Their results show that during the time interval before (10:00-11:00 h) and after (13:00-14:00 h) midday, characterized by solar elevation angles (SEA) between 63-75° and 61-73° respectively, is the most harmful time period regarding potential skin damage in the face (forehead, cheek and nose). These findings are an important supplement regarding the general information with the highest risk for skin damage occurring during midday. Wang et al. (2014) further suggest to investigate the UV exposure under different (not clear-sky) meteorological conditions as these will affect the amount of surface UV radiation.

Estimations of the personal annual UVER dose amount to a mean value of 173 SED ranging between 132 SED for indoor workers and 224 SED for gardeners, respectively, which collect 55% of their UV exposure during working days (Thieden et al. 2004). More than 50% of the UV exposure of older children and adolescents is gathered at the beach with 50% of the daily UV dose being accumulated between noon and 3 PM based on the 1.1 SED threshold value for daily UVER dose according to the the American Conference of Governmental Industrial Hygienists (ACGIH 1999). In order to reduce the diurnal occupational UV dose of working people a significant UVR reduction can be reached already by having lunch inside instead of outdoors (Thieden et al. 2004). Therefore, personal UV exposure data is an important data base in order to relate the occurrence

of skin diseases to personal behaviour. According to Herlihy et al. (1994) supervised UV dosimetry in conjuction with personal logging and environmental measurements is a suitable way to gather reliable data sets being necessary to understand the causes for sunburn and other skin diseases.

The SimUVEx model - extimating individual exposure

The SimUVEx (*Sim*ulating *UV Ex*posure) model was developed in order to simulate estimates of individual exposure to solar UV radiation and its anatomical distribution based on ground irradiation and morphological data sets (Vernez et al. 2011). To perform simulations with the SimUVEx model the following input variables are required: The direct, diffuse and surface reflected irradiance components as well as both the corresponding solar azimuth and zenith angles. For clear-sky conditions radiative transfer model (RTM) data, for example from libRadtran or TUV, may be used as model input also. Due to the high complexity of accurately describing cloud processes the RTM data is not suitable to be used under cloudy conditions (Vernez et al. 2011). The following simplifying hypotheses were applied to the SimUVEx model which characterize its model core (Vernez et al. 2011):

1. The diffuse and reflected radiation parts are assumed to be almost isotropic. (leads to less symmetric cycle of diffuse radiation during clear-sky conditions → anisotropic especially for regions near the sun and for snow-covered surfaces).

2. The model simulations are performed for year-round exposure of unprotected skin and thus overestimates the real exposure by providing an upper annual exposure (potential) → enough possibilities to predict attenuating effects of sun-protection scenarios.

3. The simulation results apply for standing postures with arms down. Thus different site-specific UV exposures may occur for several outdoor activities with a significantly different posture patterns.

In the SimUVEx model the anatomical exposure to direct and diffuse UV radiation is computed by assuming a hemispherical isotropic source for both radiation parts (Fig. 12). The diffuse UV radiance $D(t)$ originating from given direction and solid angle, covering a specific hemispheric surface element, can be expressed by the measured diffuse UV irradiance $I_D(t)$ by the following expression (Vernez et al. 2011):

$$D(t) = 2I_D(t)\frac{A_S}{2\pi} \tag{2.28}$$

with the term $A_S(2\pi)^{-1}$ representing the ratio between the solid angle of a hemispheric surface element and the total hemisphere. An anisotropy correction for $D(t)$ is implemented for surface elements near the lower boundary of the hemisphere as the diffuse radiation shows larger anisotropy close to the surface. The direct radiation part $I(t)$ is expressed in the model as a radiation source with both changing intensity and location

over time in order to approximate the diurnal solar cyle (Vernez et al. 2011). In order to develop human-like manikins with the manikin surface being composed of triangular elements Vernez et al. (2011) used the free modeling package "MakeHuman". The size of each triangle varies according to the specific location and the general mesh size which can be changed to optimize the relation between computation time and model resolution. The model performance was investigated by comparing measured and simulated daily UV exposure doses showing same magnitudes overall. The symmetric mean absolute percentage error (sMAPE) was calculated amounting to 13% for selected (reasonable) measurements (Vernez et al. 2011). The SimUVEx model has already been applied in different studies

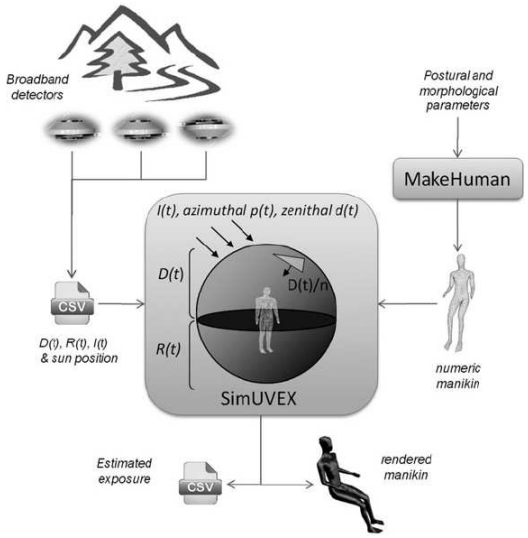

Fig. 12: Schematic illustration of the SimUVEx model extracted from Vernez et al. (2011).

examining, for example, the relative contributions of diffuse, direct and reflected UV radiation to the total annual body UV exposure (Vernez et al. 2012). These results were in good agreement regarding the exposure patterns (Wright et al. 2012; Thieden et al. 2004) or the UV exposure of different body parts (e.g. Siani et al. 2011). Milon et al. (2014) used the SimUVEx model in order to determine the occupational UV exposure which largely contributes to the longstanding personal UV exposure and therefore leading to a significantly enhanced skin cancer risk.

For the investigations presented in section 4.2 simulations with the SimUVEx model were performed to elaborate the cloud meteorological influence on the UVER exposure of manikins especially with regard to specific anatomical areas like head, face, chest or neck. Two working meetings at the Institute for Work and Health (IST) in Lausanne were set up to discuss the research conception and prepare the simulations. The SimUVEx simulations based on measured data of 16 August 2016 were executed by A. Milon during our second meeting at the IST. The simulations based on measured data of 17 August 2016 were also executed by A. Milon within the previously fixed conception. For these simulations one minute mean values of horizontally measured dosimeter data were used with the raw data being collected separately for the UV-A and UV-B spectral ranges each second, respectively. The anatomical zones of a selected human body posture (Fig. 13) can be defined specifically for each SimUVEx simulation according to possible demands.

As an example, small rectangles can be included into both the forehead and the trunk-top anatomical zones serving as points-of-interest (POI) of the manikin presented (Fig. 13). For the evaluation of the meteorological influence on individual UVER exposure which is presented in section 4, thirteen anatomical zones (Tab. 1) were selected due to their orientation towards the sun. Between both simulations a small size change of some of the selected anatomical zones unintentionally occurred amounting up to 3.6% (Tab. 1). The size change has no influence on the investigations presented later as the simulations were analyzed for both days separately by comparing clear sky (estimated) and measured data, respectively.

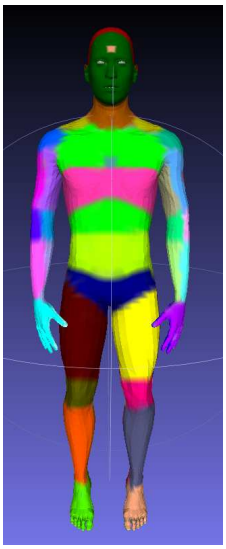

Fig. 13: Visualization of a manikin's anatomical zones being used for SimUVEx simulations (provided by A. Milon).

Tab. 1: Anatomical zone areas (cm^2)

anat. zone	zone area cm^2 (16.8.)	zone area cm^2 (17.8.)
skull	1696.59	1696.59
face	1402.36	1391.89
neck-front	433.50	443.51
trunk-top	302.09	302.091
trunk-front	5750.09	5821.64
shoulder left	443.063	443.054
lower arm ol***	341.596	341.594
shoulder right	507.693	489.749
lower arm or*	547.439	547.437
u** front leg right	1688.51	1721.52
foot right	1160.34	1160.34
u** front leg left	1603.82	1603.82
foot left	1152.62	1152.62

* outside right
** upper
*** outside left

3 Research project and equipment

Solar UV radiation can have beneficial as well as harmful effects on human health and life (section 1). Positive effects include for example the creation of vitamin D, skin tanning and a general well-being. The increasing number of skin cancer cases due to longstanding UV exposure highlight negative concequences of UV radiation in affecting human health. Especially outdoor workers accumulate high UV doses over their occupational life leading to a higher risk for skin cancer development. The department for radiation at the DGUV Institute for Occupational Safety and Health (IFA) in Sankt Augustin launched a research programme (project IFA4207) to investigate the UV exposure for people working outside. By law, assurances have to provide services in case of insured events and to provide prevention measures for employees regarding their occupational health and work safety. With regard to solar UV radiation the measurement of the actual exposure at work and the identification of endangering job activities is the basis to create a reliable data base for risk assessment. For occupational illness cases, like skin cancer for example, this data base can be used in combination with epidemiological data to derive exposure-action relations between UV exposure and the work-related occurrence.

As previously introduced the amount of UV radiation reaching the earth's surface is variable on daily to decadal time-scales. The main reasons for this behaviour include variabilities of sun's activity, the seasonal variation of the distance between the earth and the sun as well as daily and seasonal changes of the stratospheric ozone concentration. Surface UV radiation also depends on altitude, latitude, solar zenith angle (SZA) and aerosol concentration. In addition the daily weather, being often characterized by large diurnal variations of cloud amount, cloud type and humidity, also contributes to a diurnal variability of surface UV radiation. The research issues presented in the thesis at hand are to determine the actual UVER exposure of outdoor workers, to quantify the cloud meteorological influence on personal UVER exposure and to compare both the effect of a low-ozone event and the impact of shallow stratocumulus clouds on surface solar UVER at the same time.

3.1 The GENESIS-UV platform

The core of the IFA research campaign launched in 2014 is the data collection platform GENESIS-UV (*GEN*eration and *E*xtraction *S*ystem for *I*ndividual expo*S*ure) with the objective to collect a data base for individual UVER exposure. The GENESIS-UV platform consists of dosimeters collecting data, tablets serving as user interfaces and a data storage server (Wittlich et al. 2016). The participating assurance providers recruited probands of their respective member companies in order to collect different individual exposure data sets. The dosimeters were fixed at each proband's upper left arm while working outside. The multiple data sets allow the determination of the workers actual UVER exposure both in contrast to earlier UV measurements by the Federal Office for Radiation Protection (BfS) performing local stationary measurements to calculate the UVI and in contrast to earlier personal dosimetric measurements without a direct relation to the actual workers job tasks. The basic equipment for probands is a carry box containing a tablet, dosimeter(s) and further necessary tools (cf. Figs. 14, 15). The dosi-

Fig. 14: Carry box with the equipment for each proband.

Fig. 15: Gigahertz dosimeter X2012 v2

meters are produced by "Gigahertz-Optik GmbH" and designed as a mobile measurement and data logging unit. The dosimeter version X2012 v2 (Fig. 15) consists of two photodiods performing synchronous irradiance measurements in the UV-A, UV-B and UV-C spectral ranges, respectively. By factory the photodiod's diffusors can be provided with

Tab. 2: General dosimeter specifications (version X2012 v2)

parameter	specifications
power supply	via USB2.0 interface (5V, 500mA)
integral sensors	2 photodiods
magnetic sensor	1300 μT (x-,y-axis), 2500 μT (z-axis), 0.3 μT resolution
acceleration sensor	3-axes sensor, range $\pm$ 2g
temperature sensor range	-20°C to 80°C, permitted -10°C to 50°C
measuring ranges	6 (200pA to 20μA)
$\Rightarrow$ ranges:	error $\pm$ offset:
$\pm$ 20μA	0.2% $\pm$ 0.2μA
$\pm$ 2μA	0.2% $\pm$ 0.002μA
$\pm$ 200nA	0.2% $\pm$ 0.2nA
$\pm$ 20nA	0.2% $\pm$ 0.02nA
$\pm$ 2nA	0.5% $\pm$ 2pA
$\pm$ 200pA	0.5% $\pm$ 2pA

three different spectral weighting functions for both sensors to distinguish between the measurement of erythemally, effectively or radiometricaly weighted UV irradiances. In addition, each device contains an acceleration and a magnetic sensor offering the possibility to calculate the position and orientation in space. The collected parameters are stored on an internal memory being designed to gather data of a whole working week. An USB interface is used to exchange data and to recharge the accumulator. More device specification informations can be found in the corresponding operations manual.

3.2 The mobile weather station

A mobile weather station (Fig. 16) is used to collect the meteorological data during the IFA research programme. The collocation of the meteorological measurement unit was the major task prior to the GENESIS-UV campaign 2016 in order to assemble a set of meteorological instruments fulfilling the WMO Secondary Standard regarding their measurement accuracy (WMO 2010). The mobile meteorological station used during the

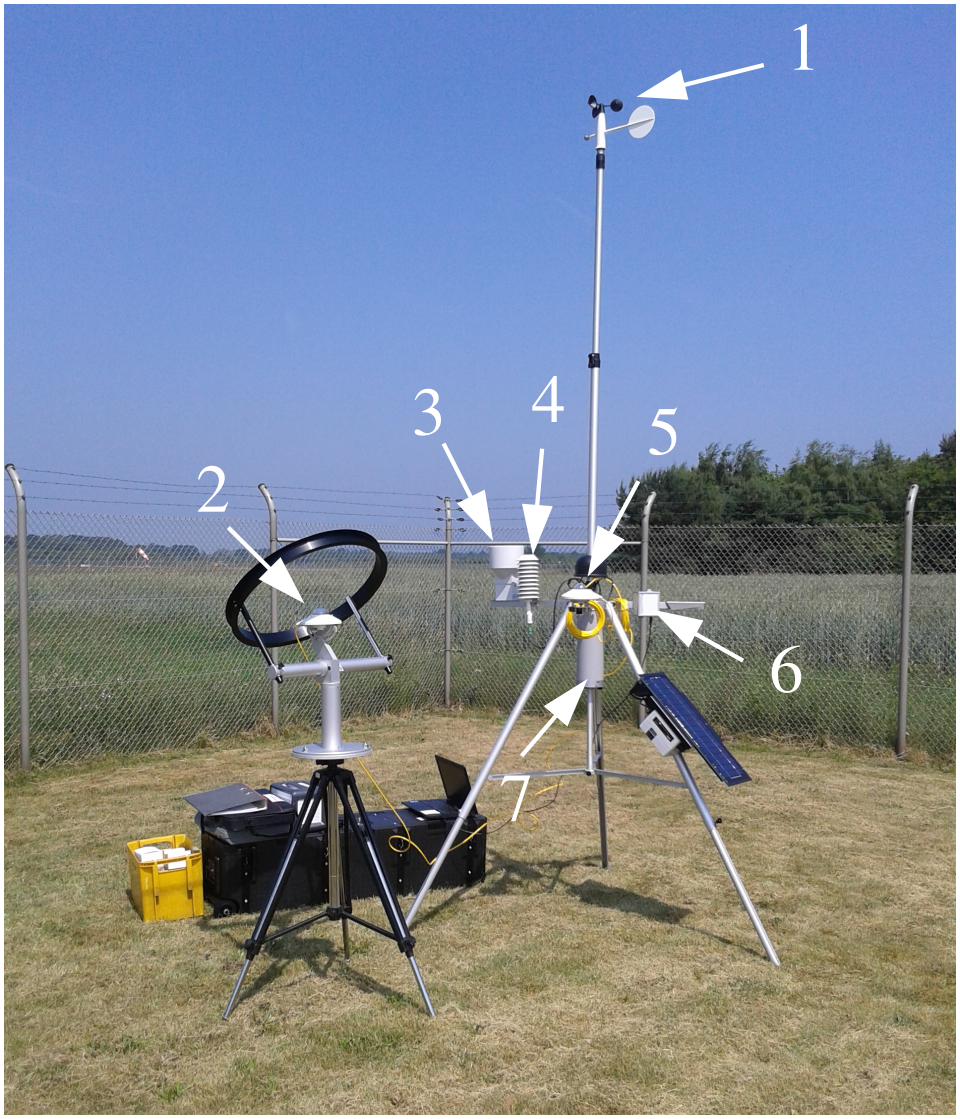

Fig. 16: The mobile weather station at the DWD site in Münster (6.6.2016, 14:41 pm). The meteorological sensors are labeled by the numbers (1-7).

2016 campaign consists of seven different sensors (1-7) attached at a tripod with a 4 m mast to collect the following meteorological variables: Wind speed and direction (1), precipitation (3), temperature and humidity (4), air pressure (7) as well as global solar irradiance (5). The sensor recording diffuse solar irradiance data (2) is mounted on an auxiliary tripod (Fig. 16). The spectroradiometer (6) is attached at a sensor bar of the mobile station gathering spectral solar UVER data. Each sensor is described in detail in the following labeled according to the corresponding sensor number (see Fig. 16):

1 Wind speed and direction are measured by a combined Vaisala sensor consisting of an anemometer and a weather vane. The anemometer collects data using a dual reed switch as transducer to generate the anemometer rotation frequency F. The transfer function $U = -0.24 + 0.699F$ allows the calculation of the wind speed U, given the frequency F. The wind speed threshold to start data gathering is below 0.4 ms^{-1} with a measuring range between 0.5 and 60 ms^{-1}. The anemometer accuracy amounts to $\pm$ 0.3 ms^{-1} for wind speeds $\leq$ 10 ms^{-1} and to $<$ 2% for wind speeds $>$ 10 ms^{-1}.

Wind direction data is collected using a potentiometer with a damping ratio of 0.3 and an overshoot ratio of 0.4. The wind speed starting threshold for gathering data is below 1 ms^{-1} and the measuring interval ranges from 0° to 360° with an accuracy of less than $\pm$ 3%.

2 Diffuse solar irradiance data is collected with a pyranometer of the Kipp & Zonen specification CMP10 mounted in the center of a shadow ring shielding the direct part of the solar radiation. This pyranometer's technical design is of Secondary Standard according to the ISO classification 9060:1990. The CMP10 sensor records solar irradiance data in a spectral interval ranging from 285 to 2800 nm with a directional error of less than 10 Wm^{-2} at 1000 Wm^{-2}. For more technical information the reader is referred to the CMP10 data sheet.

The shadow ring of the Kipp & Zonen specification CM121B prevents the pyranometer located in its center from direct solar irradiance. CM121B consists of anodized aluminium and stainless steel, its weight inclusive installed pyranometer amounts to 5.8 kg. The ring has an outer diameter of 620 mm and a width of 55 mm. For more information concerning correction factors, usage and assembling, the reader is referred to the respective technical documentation.

3 Precipitation data is collected with a rain gauge fixed on a sensor bar of the mobile station. The transducer of the gauge is a self-emptying tipping magnet with a sensitivity of 0.2 mm and a capacity of 144 mmh^{-1}. The opening area of the gauge's enclosure, made of UV-stabilized plastic, amounts to 200 cm^2. For a rain intensity of less than 24 mmh^{-1}, the accuracy of the gauge amounts to $\pm$ 5% and decreases to $\pm$ 10% for rain intensities lower than 120 mmh^{-1}.

4 Air temperature and relative humidity are measured by the "Vaisala HUMICAP® Humidity and Temperature Probe HMP155". Relative humidity (RH) is measured with a capacitive thin film HUMICAP® polymer sensor with a measurement interval ranging from 0 to 100% RH. The accuracy of the HMP155 sensor depends on the temperature of the surrounding air, for example in the temperature range from 15 to 25°C the accuracy amounts to 1% RH for a relative humidity between 0 and 90% and to 1.7% RH for relative humidity values between 90 and 100% RH.

Air temperature data is collected by means of a resistive platinum sensor (Pt100) with a measurement interval ranging from -80 to $+60$°C. The accuracy of the platinum sensor depends on the surrounding air temperature as well and has to be calculated for several temperature intervals separately. For more information the reader is referred to the HMP155 documentation.

5 Global solar irradiance data is collected with another pyranometer of the Kipp & Zonen specification CMP10. The only difference between the collection of global and diffuse solar irradiance is whether the pyranometer is shaded during the measurement or not. For more technical information, the reader is referred to item 2 of this paragraph and to the respective technical documentation.

6 Spectral global UV irradiance measurements were performed using the "Gigahertz-Optik GmbH" spectroradiometer specification BTS2048-UV-S. The spectroradiometer enclosure is attached vertically at a sensor bar of the mobile station in order to provide a horizontal position of the UV-sensor (Fig. 16). The core of this spectroradiometer is the BiTec sensor. It combines photodiode and back-thinned CCD diode array properties providing precice radiometric measurements through a bilateral correction procedure of both sensor measurements. A diffusor with a cosinus corrected field of view collects the incoming solar UV irradiance ranging from 190 to 430 nm. The optical band width of the sensor with 2048 pixels amounts to 0.8 nm. More technical information can be found in the sensor's technical documentation.

Performing measurements with the spectroradiometer requires a permanent USB connection to a laptop providing power supply and allowing data storage on the laptop's harddisk. The software to start, finish and control the spectroradiometer measurements is also installed on the same laptop offering a live visualization of the data being captured. To perfom permanent measurements lasting up to or more than seven hours an external power supply is necessary and provided by a portable accumulator in our case.

7 Air pressure data is gathered by means of the BARO-1 module using the capacitive Vaisala BAROCAP® sensor. The pressure module is mounted within the data logger enclosure of the mobile weather station positioned between the three feet of the station's tripod. The sensor collects data ranging from 500 to 1100 hPa providing a resolution of 0.1 hPa and an accuracy of $\pm$ 3% for a surrounding temperature range between -40 to $+60$°C.

The equipment of the mobile weather station contains three further components including an action camera made by DBPOWER to take photographs of the sky every ten seconds during each measurement period (Fig. 17). Thus the additional information concerning cloud coverage and development during the meteorological measurements can be used for a better interpretation of the measured data sets. To simplify the subjective interpretation all pictures are condensed to a short video sequence for each measurement day showing 25 pictures per second. Another component is the USB ventilator being attached on the sensor bar in front of the HMP155 sensor (upper arrow, Fig. 18) as a result of comparing the temperature data collected synchronously by the mobile station and the official DWD station at Münster/Osnabrück International airport. Hereafter, the MAWS temperature data is characterized by a much higher variability due to the lack of ventilation. The third component is an USB power bank (lower arrow, Fig. 18) mounted on a stabilizing cross bar of the tripod feet as power supply for the ventilator.

In addition to the above mentioned sensors, two dosimeters are attached at the mobile station during the meteorological measurements as well. For each application of the meteorological unit the same two dosimeters are used. They are fixed horizontally to col-

Fig. 17: Action camera attached at a sensor bar of the mobile weather station (Kirchheim a.N., 21.6.2016, 10:41 am)

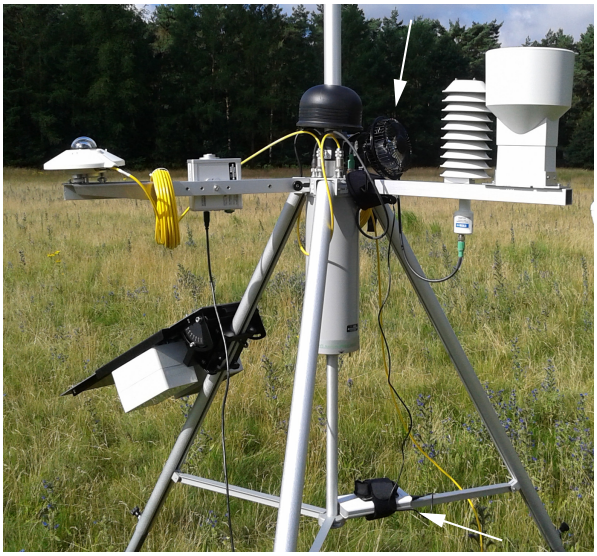

Fig. 18: Mobile weather station with USB ventilator and power bank (Münster-Handorf, 12.7.2016, 9:45 am)

lect both, the diffuse and the global solar UVER to be compared to the respective personal data sets. The dosimeter measuring the diffuse UVER data is attached to the pyranometer being mounted in the center of a shadow ring (Fig. 19). On the other hand, the dosimeter collecting global UVER data is fixed at one of the mobile station's sensor arms (see Fig. 20).

Fig. 19: Shadow ring with pyranometer and dosimeter (Kirchheim a.N., 21.6.2016, 10:40)

Fig. 20: Dosimeter and action camera on sensor arm (Kirchheim a.N., 21.6.2016, 10:41)

Besides the laptop to control the spectroradiometer measurements, another laptop is necessary to run two factory provided software tools. One tool, called "AWS Client", is made to establish a temporary connection to the station's data logger to up- and download logger setup files, to download log files and to control the logger status via shell commands. "Lizard", the second software tool, is needed to create logger setup files which exactly specify the logger configuration. For example, a configuration file includes the selection of all sensors being attached to the meteorological station and very importantly the definition of log groups containing the parameters to be collected within the same time interval.

3.3 Meteorological measurements

During the GENESIS-UV campaign 2016, lasting from April to the end of October, dosimeter measurements were performed by probands to collect individual UV exposure data. For eight selected occupational groups meteorological measurements, lasting for 5 to 7 hours at one or two days, were performed synchronously to individual dosimeter measurements. These measurements are named "accompanied measurements" because a member of the respective assurance provider took part or at least had the possibility to be part of a measurement event. Location and duration of all meteorological measurements during the 2016 campaign are listed subsequently (Tab. 3).

Tab. 3: Meteorological measurements during the GENESIS-UV campaign 2016

#	date	location	coordinates	height	occupational group
1	6.6.2016	Münster	52.1353°N 7.6978°O	47 m a.s.l.	sensor comparison
2	21-22.6.2016	Kirchheim am Neckar	49.039023°N 9.150626°O	180 m a.s.l.	track worker
3	6.7.2016	Lippstadt	51.670156°N 8.363912°O	81 m a.s.l.	cable mechanic
4	12.7.2016	Münster	52.007138°N 7.723614°O	51 m a.s.l.	surveying technician
5	19.-20.7.2016	Karlsruhe	49.013866°N 8.329999°O	115 m a.s.l.	scrapyard worker
6	26.7.2016	Jork	53.504820°N 9.755103°O	1 m a.s.l.	fruiter
6	27.7.2016	Drochtersen	53.711367°N 9.263469°O	-3 m a.s.l.	fruiter
7	2.-3.8.2016	Sassnitz	54.538476°N 13.602672°O	121 m a.s.l.	chalk factory worker
8	16.-17.8.2016	Jena	50.934044°N 11.566115°O	174 m a.s.l.	beachvolleyball player
9	23.-24.8.2016	Buxtehude	53.479437°N 9.692135°O	3 m a.s.l.	kindergartner
10	14.11.2016	Münster	52.1353°N 7.6978°O	47 m a.s.l.	sensor comparison

During the GENESIS-UV campaign 2017, lasting from April to the end of October, dosimeter measurements were performed by probands to collect individual UV exposure data. For two selected occupational groups meteorological measurements lasting for 5 to 7 hours at one or two days were performed synchronously to individual dosimeter measurements. These measurements are named "accompanied measurements" with a member of the respective assurance provider being part of or having the possibility to take part of a meteorological measurement. All meteorological measurements during the 2017 campaign are listed below (Tab. 4).

Tab. 4: Meteorological measurements during the GENESIS-UV campaign 2017

#	date	location	coordinates	height	occupational group
1	5.-7.4.2017	Didcot	51.574979°N 1.31768°W	123 m a.s.l.	-*
2	1.6.2017	Münster	52.1353°N 7.6978°O	47 m a.s.l.	-**
3	4.7.2017	Mannheim	49.508966°N 8.440027°O	100 m a.s.l.	fuel depot worker
4	18.-19.7.2017	Profen	51.129026°N 12.189568°O	150 m a.s.l.	coal worker

* Measurement of a low-ozone event.
** Sensor comparison at the aerial DWD station

Sensor functionality check

The first application of the mobile meteorological station took place on 6 June 2016 at the official DWD weather station at Münster/Osnabrück International Airport (Figs. 21, 22). The measurement was set up in order to check the functionality and accuracy of the (new) meteorological station by comparing each meteorological parameter to the respective counterpart which was collected by the official DWD station. The final meteorological

Fig. 21: Aerial picture of the DWD aerial weather station at Münster/Osnabrück airport and position of the mobile station (arrow) (www.bing.com/maps)

Fig. 22: Mobile weather station and official DWD station (12:45 pm)

measurement in 2016, after the regular GENESIS campaign, was performed again at the DWD station of Münster/Osnabrück International airport. The reason for this measurement was to get an update of the unit's accuracy and functionality after numerous meteorological measurements (Tab. 3). A third comparison measurement at the same DWD station took place on 1.6.2017 (cf. Tab. 4). For each of these comparison measurements the mobile unit was rigged up near the official instruments of the DWD station (Figs. 21, 22). The DWD station in Münster was chosen as reference station because of its relatively easy accessability not being located within the airport's security zone. The mobile meteorological station was rigged up close to the DWD sensors within the official "weather garden" zone bounded by a fence.

The comparing measurement on 1.6.2017 results show that all sensors, except for the pyranometers, work quite well and reasonably collect data like during the previously performed measurements (6.6.2016, 14.11.2016). Due to a sensor failure of the DWD station's irradiance sensors (pyranometers), unfortunately no comparison between the MAWS pyranometer data and the respective DWD data can be presented here. The comparison results for all meteorological sensors of the MAWS, the respective accuracy according to the producer as well as the respective mean difference values derived from all three comparing measurements are listed below (Tab. 5):

Tab. 5: Comparison of the MAWS sensor mean differences* (MD)

sensor	accuracy	MD 6.6.16	MD 14.11.16	MD 1.6.17
anemometer	$\pm$ 0.3 ms^{-1} ($\mathbf{v} \leq 10ms^{-1}$) < 2 % ($\mathbf{v} > 10ms^{-1}$)	0.9 ms^{-1}	1.2 ms^{-1}	0.6 ms^{-1}
potentiometer	$\pm$ 3%	10°	12°	-
pyranometer	diffuse irradiance 10 Wm^{-2} (direction)	-**	8%	-****
pyranometer	global irradiance 10 Wm^{-2} (direction)	5%	8%	-****
HMP155 (RH)	1% (0 - 90% RH) 1.7% (90 - 100% RH)	1% RH	4% RH	1.7% RH
HMP155 (T)	-80 to +20°C $\pm$(0.226 - 0.0028 $\times$ T)°C	-0.4 K	-0.35 K	-0.9 K
HMP155 (T)	+20 to +60°C $\pm$(0.055 + 0.0057 $\times$ T)°C	-0.8 K	-***	-0.6 K
BAROCAP®	$\pm$ 3% -40 to +60°C	-0.4 hPa	-0.45 hPa	-0.44 hPa

* The mean difference is calculated as (DWD-MAWS).
** Could not be determined due to wrong setup programming.
*** Air temperature below 20°C during the measurement.
**** No DWD data due to sensor failure.

4 Results

4.1 UVER exposure of outdoor workers

The measurement results regarding the UVER exposure of outdoor workers are presented and discussed in the following section. Due to the almost perfect clear sky conditions on both measurement days the fifth measurement of the GENESIS-UV campaign 2016 (Tab. 2) is picked as an example of how each of the accompanied measurements was analyzed. The results of the other accompanied measurements (Tab. 2, 3) will be summarized and discussed at the end of this paragraph (Tab. 8(1,2)).

The fifth meteorological measurement within the GENESIS-UV campaign 2016 took place in the inland port of Karlsruhe on 19 and 20 July 2016 (Fig. 23). The GENESIS probands working on a scrapyard were equipped each with a dosimeter to collect their individual exposure. The mobile meteorological unit was built up on the uppermost level of a car park (15 m height) being the most undisturbed location close to the probands working places (Fig. 24).

Fig. 23: Aerial picture of the MAWS location in Karlsruhe (arrow) (www.bing.com/maps)

Fig. 24: Mobile weather station on uppermost car park level (19.7.2016, 8:59 am)

The synoptic situation on 19 July 2016 was characterized by a shortwave ridge over France and high surface pressure over Germany (Fig. 25). Largescale subsidence supressed cloudiness over southwest Germany with temperatures climbing up to 35 °C. Over night the ridge moved further eastward over Germany leading to an increasing influence of the surface low located west of the British Isles over Central Europe (Fig. 26). Governed by the large scale flow warm airmasses from the Mediterranean were advected to Central Europe urging a further temperature rise up to 37 °C. A low-level convergence occurred in the

evening of 20 July 2016 forcing a squall line formation from Belgium to eastern France. As a result thin anvil cirrus clouds were advected from the west to the Karlsruhe region in the afternoon. The UV hazard prognosis chart for 19 July 2016 shows very high danger

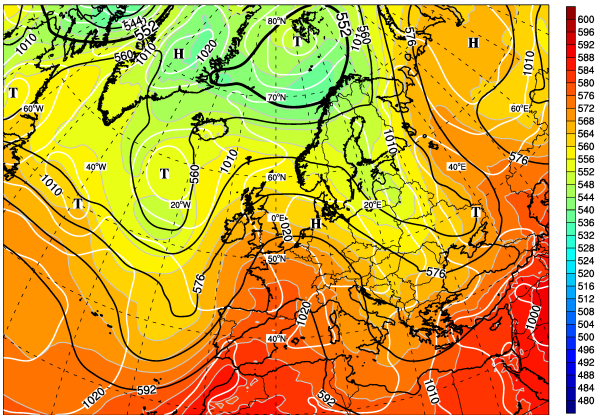

Fig. 25: 500 hPa geopotential [gpdam], surface pressure [hPa], relative topography 500-1000 [gpdam], 19 July 2016, 12 UTC (NCEP-GFS model analysis)

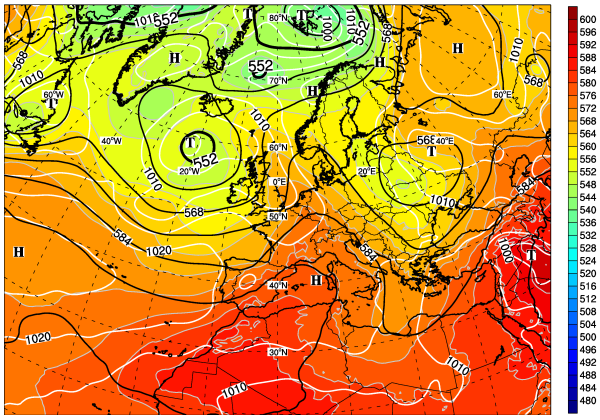

Fig. 26: 500 hPa geopotential [gpdam], surface pressure [hPa], relative topography 500-1000 [gpdam], 20 July 2016, 12 UTC (NCEP-GFS model analysis)

levels in Southern, Central and Western Germany (Fig. 27). These high UV danger levels result from clear conditions and the relatively low noon solar zenith angle in July. In the northeastern part of Germany the UV endangerment reaches low to medium levels. These parts of Germany are still weakly influenced by an upper trough over eastern Europe generating shallow cloud cover. On 20 July 2016 the UV danger levels are still very high extending further northeastward compared to the 19 July (Fig. 28). The reason for this development is the eastward movement of the ridge and subsequently less cloudiness due to large scale subsidence in the eastern parts of Germany.

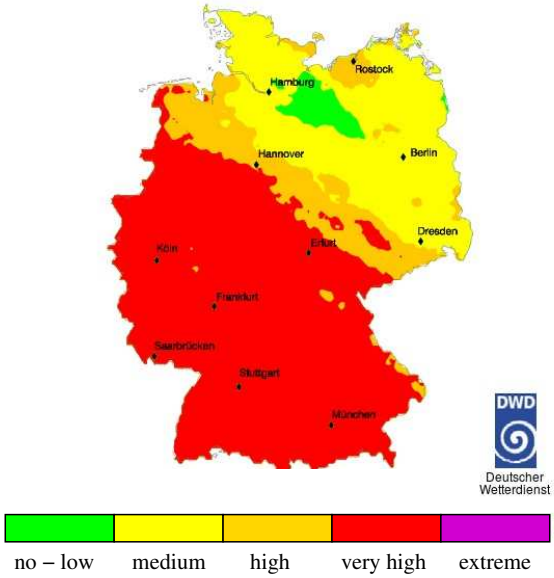

Fig. 27: UV hazard prognosis for 19.7.2016 (www.dwd.de)

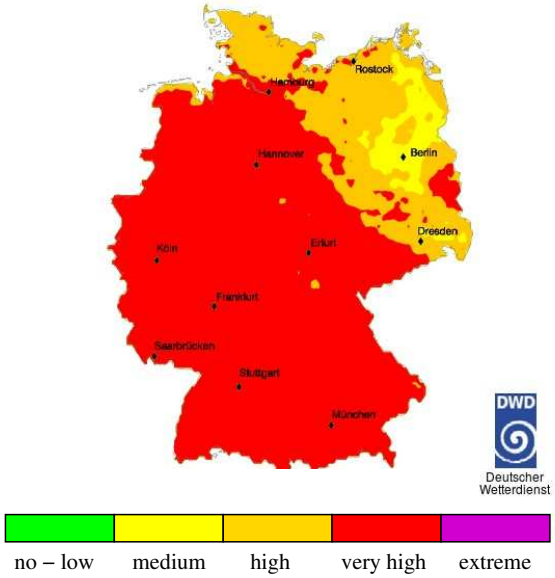

Fig. 28: UV hazard prognosis for 20.7.2016 (www.dwd.de)

The UVI values derived from dosimetric measurements amount to 9 on both measurement days (Fig. 29) justifying the high UV danger prognosis for both days (Fig. 27, 28). They also confirm the DWD UVI prognosis for the Karlsruhe region having predicted UVI values up to 9 for both days. The advection of anvil cirrus clouds, as previously mentioned, causes a total UVER dose decrease of 0.98 SED on 20 July (Fig. 29, right). By splitting

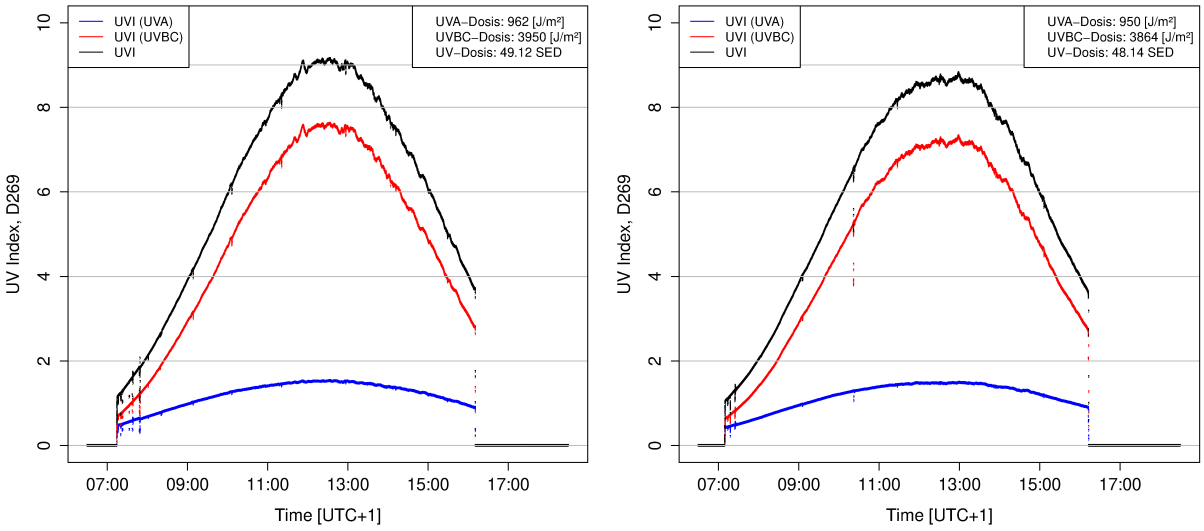

Fig. 29: UVI and global UVER doses on 19 (left) and 20 (right) July 2016 in Karlsruhe.

the UVI with respect to its UV-A and UV-B spectral part, the measurements of both days show the absolute UV-B contribution being roughly four times as large as the respective UV-A contribution around noon (Fig. 29). The total UVER dose during the measurement period amounts to 49.12 (48.14) SED on 19 (20) July. In order to determine the total UVER dose during midday the one hour time interval embracing the moment of maximum solar elevation is considered on both days. The resulting dose amounts to 8.14 SED or 16.6% (7.77 SED or 16.1%) on 19 (20) July, respectively. For a two hour time interval the respective doses amount to 16.02 SED or 32.6% (15.41 SED or 32.0%) highlighting the importance of this specific time period of the day regarding the maximum dose amount to be received by oudoor working people. The results of both the horizontally measured

Tab. 6: Meaning of abbreviations used in Tab. 7, 8(1) and 8(2)

abbreviation	meaning
#	couter of meteorological measurements as introduced in Tabs. 2, 3.
diffM	measured diffuse dose
globM	measured global dose
% globM	ratio of selected dose and globM [%]
reflM	measured reflected dose
prob	proband during a GENESIS-UV campaign (e.g. April - October)
1d	proband during one measurement within a GENESIS-UV campaign

UVER exposure as well as the dosimetric data collected by the scrapyard workers are summarized in table 7 with the abbreviations used herein and in tables 8(1,2) being introduced in table 6. The selected time interval differs for each measurement day as the time period of synchronous data gathering by both the probands at work and the stationary measurements varies for organizational reasons. During their working shifts on 19

(20) July the probands received between 6.4 and 15.8% (4.3 and 10.3%) of the maximum possible dose amount (Tab. 7) with the differences being attributed to different job tasks.

Tab. 7: UVER doses measured in Karlsruhe on 19. and 20.7.2016

#	dosimeter	type	UV-A [Jm^{-2}]	UV-B [Jm^{-2}]	UV [SED]	% globM
a) 19.7.2016, time interval: 7:14 - 16:10 UTC+1, proband job: scrapyard worker						
5	089/14867	diffM	422	1793	22.15	45.1
5	269/15066	globM	962	3950	49.12	100.0
5	14974	prob	58	232	2.9	6.4
5	15059	prob	75	274	3.49	7.1
5	15072	prob	163	613	7.76	15.8
5	15137	prob	97	316	4.14	8.4
b) 20.7.2016, time interval: 7:09 - 16:12 UTC+1, proband job: scrapyard worker						
5	089/14867	diffM	426	1752	21.78	45.2
5	269/15066	globM	950	3864	48.14	100.0
5	14974	prob	41	166	2.07	4.3
5	15059	prob	63	233	2.96	6.1
5	15072	prob	82	290	3.72	7.7
5	15137	prob	122	372	4.94	10.3

Regarding all data sets, the highest UVER doses collected during the respective time interval of synchronous measurements amount to 7.76 SED (15.8%) for a scrapyard worker (Tab. 7a), to 7.55 (22.2%) and 7.94 SED (23.4%) for track workers (Tab. 8(1)b) and to 7.29 SED (38.6%) for a fruiter (Tab. 8(1)f) which is almost the same level regarding the absolute doses. High relative dose amounts, however, indicate much less UVER protection for fruiters and track workers, for example. Some fruiters working during the same respective time interval only received 0.54 and 0.56 SED (Tab. 8(1)e,f). These significant differences within the same worker group result from different job tasks and better protected work places, like within a driver cabin for example. The lowest UVER doses were collected by probands working as kindergartners with dose amounts ranging between 0.07 and 2.33 SED (Tab. 8(2)k,l). The very low exposure values of some kindergartners are a result of their mainly indoor work, whereas several hours of outdoor work led to the significantly higher UVER doses. The UVER doses collected by coal workers in Profen reach up to 2.45 SED during the respective shifts (Tab. 8(2)r,s). The results of one coal worker (dosimeter 15019), however, are considered non-representative as the corresponding exposure data sets of both days are characterized by time periods with almost no variability stretching from several minutes up to roughly one hour (not shown). This behaviour almost certainly results from an unmoved dosimeter only happening if it is being pulled off from the upper arm during the respective time periods.

By comparison, measured and forecasted UV index values for the respective measurement show the best agreement for clear conditions or during conditions with shallow broken low-level cloudiness (Fig. 29 and Tab. 8(2)l,q). For these cases measured and forecasted UVI values were identical. In eight cases with broken cumulus cloudiness during the day (Tabs. 8(1)d,e,f,g,i,j, and 8(2)p,s) the UVI values based on measurements exceeded the DWD prognosis by at least one and in one case by two UVI units. Thus, in this case a systematic underestimation is observed regarding the UVI forecasts. For two cases large differences between measured and forecasted UVI values occurred amounting up to 8 (Tab. 8(1)a) and 4 (Tab. 8(2)k) UVI units, respectively. The conditions during the first of these two cases were characterized by strong cloud cover (7-8 oktas) in low and medium levels. During short time periods (up to 30 min) the low-level clouds disap-

Tab. 8(1): UVER doses measured in 2016 (cf. Tab. 2)

#	dosimeter	type	UV-A [Jm^{-2}]	UV-B [Jm^{-2}]	UV [SED]	% globM	UVI (DWD)	UVI (meas.)
a) Kirchheim am Neckar, 21.6.2016, time interval: 8:51 - 15:24 UTC+1, proband job: track worker								
2	089/14867	diffM	359	1333	16.93	76.8	-	-
2	269/15066	globM	443	1763	22.05	100.0	2	10
2	056/14973	1d	92	441	5.06	22.9	-	-
2	239/15083	1d	48	187	2.36	10.7	-	-
2	297/15096	1d	132	513	6.45	29.3	-	-
b) Kirchheim am Neckar, 22.6.2016, time interval: 8:57 - 14:08 UTC+1, proband job: track worker								
2	089/14867	diffM	285	1244	15.29	45.0	-	-
2	269/15066	globM	646	2754	34.0	100.0	-	10
2	056/14973	1d	130	625	7.55	22.2	-	-
2	239/15083	1d	44	169	2.13	6.3	-	-
2	297/15096	1d	165	629	7.94	23.4	-	-
c) Lippstadt, 6.7.2016, time interval: 7:15 - 15:16 UTC+1, proband job: cable mechanic								
3	089/14867	diffM	418	1193	16.11	59.2	-	-
3	269/15066	globM	690	2033	27.23	100.0	-	8
3	14969	prob	23	76	0.99	3.6	-	-
d) Münster/Handorf, 12.7.2016, time interval: 8:16 - 14:15 UTC+1, proband job surveying technician								
4	089/14867	diffM	338	974	13.12	57.5	-	-
4	269/15066	globM	583	1700	22.83	100.0	6	7
4	14965	prob	94	255	3.5	15.3	-	-
e) Jork, 26.7.2016, time interval: 9:19 - 14:09 UTC+1, proband job: fruiter								
6	089/14867	diffM	275	934	12.09	60.5	-	-
6	269/15066	globM	465	1535	20.0	100.0	6	7
6	056/14973	1d	45	150	1.95	9.8	-	-
6	101/14881	1d	17	38	0.54	2.7	-	-
6	239/15083	1d	83	241	3.23	16.2	-	-
6	273/15123	1d	43	141	1.84	9.2	-	-
6	297/15096	1d	77	242	3.19	16.0	-	-
6	14997	prob	64	565	6.29	31.5	-	-
f) Drochtersen, 27.7.2016, time interval: 9:08 - 14:05 UTC+1, proband job: fruiter								
6	089/14867	diffM	332	948	12.80	67.8	-	-
6	269/15066	globM	474	1415	18.89	100.0	5	6
6	056/14973	1d	165	564	7.29	38.6	-	-
6	101/14881	1d	123	352	4.76	25.2	-	-
6	239/15083	1d	114	333	4.47	23.7	-	-
6	273/15123	1d	67	211	2.78	14.7	-	-
6	297/15096	1d	34	99	1.33	7.0	-	-
6	14962	prob	17	39	0.56	3.0	-	-
g) Sassnitz, 2.8.2016, time interval: 11:59 - 18:29 UTC+1, proband job: chalk factory worker								
7	089/14867	diffM	137	194	3.31	69.2	-	-
7	269/15066	globM	181	297	4.78	100.0	5	6
7	273/15123	1d	26	35	0.61	12.8	-	-
7	297/15096	1d	49	63	1.12	23.4	-	-
h) Sassnitz, 3.8.2016, sensor error								
7	089/14867	diffM	-	-	-	-	-	-
7	269/15066	globM	-	-	-	-	3	-
7	273/15123	1d	0	0	0	-	-	-
7	297/15096	1d	0	0	0	-	-	-
i) Jena, 16.8.2016, time interval: 10:10 - 14:37 UTC+1 (no GENESIS-UV campaign measurement)								
8	089/14867	diffM	242	887	11.29	50.6	-	-
8	269/15066	globM	335	1896	22.31	100.0	6	8
j) Jena, 17.8.2016, time interval: 9:59 - 14:40 UTC+1 (no GENESIS-UV campaign measurement)								
8	089/14867	diffM	231	822	10.53	45.3	-	-
8	269/15066	globM	479	1844	23.23	100.0	5	7

Tab. 8(2): UVER doses measured in 2016 and 2017 (cf. Tab. 2, 3)

#	dosimeter	type	UV-A [Jm^{-2}]	UV-B [Jm^{-2}]	UV [SED]	% globM	UVI (DWD)	UVI (meas.)
k) Buxtehude, 23.8.2016, time interval: 7:48 - 15:19 UTC+1, proband job: kindergartner								
9	089/14867	diffM	258	784	10.42	82.3	-	-
9	269/15066	globM	308	1058	13.66	100.0	2	6
9	056/14973	1d	45	178	2.23	16.3	-	-
9	101/14881	1d	36	111	1.47	10.8	-	-
9	239/15083	1d	43	128	1.71	12.5	-	-
9	273/15123	1d	9	28	0.37	2.7	-	-
9	297/15096	1d	34	102	1.36	10.0	-	-
9	14949	prob	4	14	0.18	1.3	-	-
9	16489	prob	2	5	0.07	0.5	-	-
l) Buxtehude, 24.8.2016, time interval: 8:03 - 15:43 UTC+1, proband job: kindergartner								
9	089/14867	diffM	261	1024	12.85	42.4	-	-
9	269/15066	globM	645	2384	30.29	100.0	6	6
9	056/14973	1d	40	154	1.94	6.4	-	-
9	101/14881	1d	41	118	1.59	5.2	-	-
9	239/15083	1d	9	28	0.37	1.2	-	-
9	273/15123	1d	11	29	0.40	1.3	-	-
9	297/15096	1d	62	171	2.33	7.7	-	-
9	14949	prob	3	13	0.16	0.5	-	-
9	16489	prob	7	19	0.26	0.9	-	-
m) Münster/Osnabrück, 14.11.2016, time interval: 10:29 - 15:07 UTC+1 (sensor comparison)								
10	089/14867	diffM	99	119	2.17	90.0	-	-
10	269/15066	globM	102	139	2.41	100.0	1	1
2017								
n) Didcot (England), 6.4.2017, time interval: 6:30 - 18:30 UTC+1 (low-ozone event)								
1	089/14867	diffM	492	1082	15.75	66.7	-	-
1	269/15066	globM	713	1648	23.61	100.0	3	5
o) Didcot (England), 7.4.2017, time interval: 6:30 - 15:33 UTC+1 (low-ozone event)								
1	089/14867	diffM	405	1198	16.04	66.4	-	-
1	269/15066	globM	593	1822	24.14	100.0	3	6
p) Münster/Osnabrück, 1.6.2017, time interval: 8:25 - 13:46 UTC+1 (sensor comparison)								
2	089/14867	diffM	273	1010	12.83	42.3	-	-
2	269/15066	globM	671	2360	30.31	100.0	7	8
q) Mannheim, 4.7.2017, time interval: 7:16 - 14:00 UTC+1, proband job: fuel depot worker								
3	089/14867	diffM	384	1348	17.33	53.0	-	-
3	269/15066	globM	711	2559	32.7	100.0	9	9
3	297/15096	reflM	11	31	0.42	1.3	-	-
3	056/14973	1d	35	151	1.86	5.7	-	-
3	101/14881	1d	24	70	0.94	2.9	-	-
3	239/15083	1d	58	183	2.41	7.4	-	-
3	273/15123	1d	55	180	2.35	7.2	-	-
r) Profen, 18.7.2017, time interval: 7:00 - 13:00 UTC+1, proband job: coal worker								
4	089/14867	diffM	359	1128	14.87	55.4	-	-
4	269/15066	globM	623	2062	26.84	100.0	7	9
4	297/15096	reflM	13	33	0.46	1.7	-	-
4	14690	prob	54	191	2.45	9.1	-	-
4	15019	prob	107	576	6.83	25.4	-	-
4	15094	prob	35	192	2.28	8.5	-	-
s) Profen, 19.7.2017, time interval: 7:00 - 13:00 UTC+1, proband job: coal worker								
4	089/14867	diffM	332	1032	13.64	52.2	-	-
4	269/15066	globM	622	1990	26.12	100.0	7	8
4	297/15096	reflM	13	32	0.45	1.7	-	-
4	14690	prob	46	177	2.23	8.5	-	-
4	15019	prob	138	677	8.15	31.2	-	-
4	15094	prob	9	43	0.52	2.0	-	-

peared allowing UVER to penetrate down to the surface and causing high (short-term) UVI values up to 10. The conditions during the second case were characterized by high cloud cover (8 oktas) during the morning and noon period which, however, almost completely disappeared in the afternoon. Consequently, the UVI values were also significantly higher in the afternoon reaching values up to 6. The same UVI was also reached one day later (Tab. 8(2)l), a day being almost entirely characterized by clear conditions. Relatively large differences between measured and forecasted UV index values also occurred during the two measurement days in Didcot (Tab. 8(2)n,o) amounting to 2 and 3 UVI units, respectively. Both days were characterized by shallow stratocumulus cloud coverage from the late morning until the early afternoon. The cloudiness could have caused an underestimation of the forecasted UVI up to two UVI units which was also observed for the measurements performed in Jena (Tab. 8(1)i,j) and Profen (Tab. 8(2)r). Another important factor, however, is a low-ozone event which occurred only on the second day of the Didcot measurements. A detailed investigation of both cloud impact and a low-ozone event modifying the incoming UVER at the same time will be presented in section 4.3. For this case, the total observed 3 UVI unit difference between measured and forecasted UVI values for the second day is explained as a combined effect of both cloud influence and short-time low stratospheric ozone contents. Other factors affecting the surface UVER like aerosols, altitude or albedo contributions were not present in this case.

The DWD UVI forecast is based on a calculation method which includes the influences of ozone, aerosol, altitude, albedo and cloudiness in modifying the clear sky UVI. The accuracy of this method is $\pm$ 1 UVI unit for 80% of the forecasts (Staiger and Koepke 2005) with the main error source being attributed to the cloud contribution. Based on the previously presented measurement results the accuracy of the corresponding DWD UVI forecasts can be addressed in more detail: For all cases presented earlier the UVI forecast either equals or underestimates the measured UVI, whereas no overestimation was observed. In nine out of sixteen cases (56%) the corresponding measured UVI is underestimated by 1 UVI unit or less indicating an accurate UVI forecast. For three cases out of sixteen the differences between UVI forecasts and measurements are larger than 2 UVI units. By analyzing the respective meteorological conditions the reasons for this behaviour can be attributed to (1) overlapping effects of cloudiness and short time low stratospheric ozone contents (Didcot case), to (2) short time intervals characterized by the absence of optically thick clouds as well as to (3) a too early cloud disappearing due to a change in the synoptic situation in contrast to the original forecast. These results confirm the concluding remarks given by Staiger and Koepke (2005) regarding the reasons for the cloudiness contribution being the main error source in their UVI calculation method. From these results it is concluded that for clear and conditions characterized by broken shallow cloudiness the UVI forecast is an appropriate tool to inform the public about the actual UV hazard. For conditions with strong cloud coverage (7-8 oktas) of optically thick clouds, however, the UVI forecast may largely underestimate the actual measured surface UVI values and is therefore inappropriate as a public warning instrument without additional information. One suggestion to solve this problematic may be to provide both the UVI forecast for cloudy and clear conditions at the same time for spreads being larger than 1 UVI. Large spread values would indicate a potentially high UVER exposure if there were no clouds. This would include the main risk for receiving high UVER doses despite a low UVI forecast which is being exposed to high UVER amounts for short (up to 1 hour) time periods resulting from a strong short term cloud cover reduction.

4.2 Estimation of cloud influence on personal UVER exposure

Equipment and measurements

The mobile weather station (Fig. 30, left), being set up as introduced in section 3.1, is used to collect the basic meteorological variables. Two dosimeters (Version: X2012 v2) made by Gigahertz Optics GmbH and being of the same type as during the GENESIS-UV campaigns are attached to the meteorological station as well. One of these dosimeters is horizontally mounted on top of a sensor bar to stationarily collect global UVER data. The second dosimeter is horizontally attached to the pyranometer which is mounted in the centre of the shadow ring in order to collect diffuse UVER data.

The dosimeters in use consist of two sensors, named UVA and UVBC, collecting the UV-A (320 - 400 nm) and UVBC (UV-B and UV-C, 250 - 320 nm) erythemal radiation parts, respectively. Because UV-C radiation does not reach the ground, the UVBC data will be labeled UV-B in the following. All data were measured every ten seconds, except for the two wind variables and the dosimeter data being collected each second.

Fig. 30: *Left*: Mobile weather station in Jena (16 August 2016, 1120 LT). *Right*: Aerial picture of the MAWS location in Jena (arrow) (www.bing.com/maps)

The stationary meteorological measurements were performed next to a beachvolley court in Jena (Fig. 30, right) on 16 August from 1100 LT (LT: local time = UTC + 2 h) after having rigged up the unit next to both the football ground and the beachvolley court lasting until 1600 LT. On 17 August the meteorological measurements were performed during the same time interval.

Synoptic situation

On 16 August 2016 the synoptic situation in Central Europe is characterized by a trough located over Southern Scandinavia, Poland and the Baltic Sea (Fig. 31, left). Western Europe is influenced by a ridge extending from the Iberian Peninsula up north to the west

coast of Norway. This pressure pattern leads to an advection of cooler airmasses from the Baltic region to Eastern Germany including the Jena area. The decreased atmospheric stability over the Jena area corresponding to the upper level trough is responsible for cumulus cloud development during the day. On 17 August 2016 the trough has moved

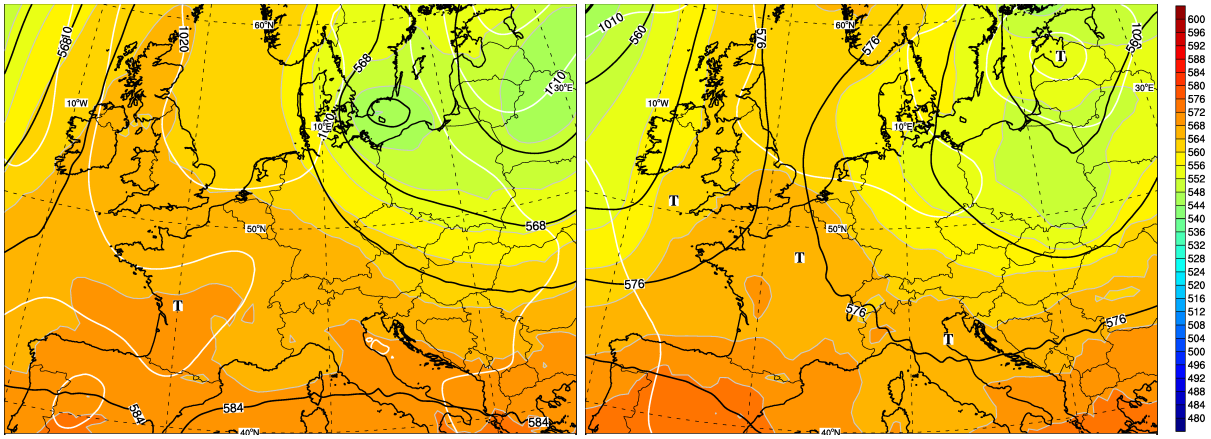

Fig. 31: 500 hPa geopotential [gpdam], surface pressure [hPa] and relative topography 500-1000 [gpdam], 16 (left) and 17 (right) August 2016, 12 UTC (data source: NCEP-GFS model analysis)

further southeastward compared to the day before and the corresponding trough axis has now shifted over southeast Poland (Fig. 31, right). Thus, the advection of maritime air from the Baltic Sea is continuing and still leading to almost the same meteorological conditions in the Jena region as the day before. With the trough now being located further eastward the atmospheric stability (Bott 2016) has increased compared to the day before resulting in generally less cloud cover.

Methods

The meteorological influence on personal UVER exposure is quantified by evaluating SimUVEx model simulations of different anatomical zones of a human body posture (cf. Fig. 13, section 2.7). The simulations are performed based on both measured and estimated dosimetric UV-A and UV-B data sets. In order to obtain a clear sky estimate of the UVER data for the same time period a non-linear regression is performed which is based on the undisturbed parts of measured UVER data of both days. A gaussian function of the type

$$f(x) = k_0 exp\left(-\frac{(x-\mu)^2}{2\sigma^2}\right) \tag{4.29}$$

is fitted to the selected UV-A and UV-B data sets, respectively, with μ the expected value, σ^2 the variance and k_0 a constant. The model simulations were performed around midday of both days with the respective time period stretching from 10:11 to 14:38 LT (9:50 to 14:40 LT) on 16 (17) August 2016. In order to analyze the cloud meteorological influence on the UVER exposure of specific anatomical zones, in this case all of which are on the front side of a human posture, the SimUVEx simulations were performed assuming

a moving posture with skull or chest always being oriented towards the solar disk. In order to visualize the cloud meteorological effect a color scheme consisting of four colors (blue, green, red, white) is used. The threshold values to assess the shifts within the color scheme are the mean dose values of all (front side) anatomical zones based on measured (hereafter: mean_measured) and estimated (hereafter: mean_clear) data, respectively. Both values are calculated based on the simulation results for each data set, i.e. for global and diffuse UVER (UV-A, UV-B), separately. For all postures presented in the following those parts of anatomical zones with dose values (much) lower than mean_measured are colored green (blue), the parts with dose values greater than mean_measured but lower than mean_clear are colored red and the anatomical zone parts with dose values exceeding mean_clear are colored white.

Simulation results (16.8.2016)

The simulation results for 16 August 2016 show significant cloud meteorological influence on the individual exposure to global solar UVER. By comparing the visualized simulation results for measured (Fig. 32, left) and estimated (Fig. 32, right) global UVER significant dose increases are obvious for face and head, the upper trunk, the upper legs as well as both feet. The strongest relative global UVER dose increase amounts to 19.2% (237.3 Jm^{-2}) for the anatomical zone named trunk front. The largest absolute global UVER dose increase amounts to 371 Jm^{-2} (18.9%) for the trunk top anatomical zone (table 9).

Fig. 32: Global individual UVER exposure. Based on measurements (left) or clear-sky estimate (right).

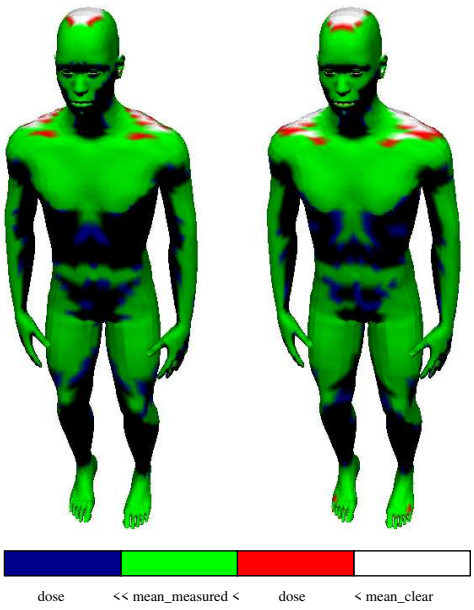

Fig. 33: Diffuse individual UVER exposure. Based on measurements (left) or clear-sky estimate (right).

The comparison of the visualized simulation results for measured (Fig. 33, left) and estimated (Fig. 33, right) diffuse UVER shows no qualitative difference of the total body exposure pattern being caused by the meteorological influence. For clear conditions the maximum diffuse dose increase occurs for the anatomical zone trunk top amounting to

36.7 Jm^{-2} (3.6%). Interestingly all anatomical zones show the same relative diffuse dose increase of 3.6% (table 10).

Tab. 9: Global (g) UVER doses and changes [Jm^{-2}]

zone	clear_g	meas_g	incr_g	%
skull	1145.3	1016.1	129.2	12.7
face	1136.1	972.5	163.6	16.8
neck-front	1188.4	1013.7	174.7	17.2
trunk-top	2336.5	1965.5	371.0	18.9
trunk-front	1470.3	1233.0	237.3	19.2
shoulder left	1555.1	1349.6	205.5	15.2
lower arm ol	1098.2	955.6	142.6	14.9
shoulder right	1504.5	1304.0	200.5	15.4
lower arm or	1147.0	986.0	161.0	16.3
u front leg r	1437.7	1210.8	226.9	18.7
foot right	1016.5	870.4	146.1	16.8
u front leg l	1468.3	1233.8	234.5	19.0
foot left	1063.3	910.0	153.3	16.8

Tab. 10: Diffuse (d) UVER doses and changes [Jm^{-2}]

zone	clear_d	meas_d	incr_d	%
skull	728.1	703.0	25.1	3.6
face	546.1	527.3	18.8	3.6
neck-front	555.9	536.7	19.2	3.6
trunk-top	1065.7	1029.0	36.7	3.6
trunk-front	607.5	586.6	20.9	3.6
shoulder left	878.9	848.6	30.3	3.6
lower arm ol	600.6	579.9	20.7	3.6
shoulder right	832.8	804.1	28.7	3.6
lower arm or	567.6	548.0	19.6	3.6
u front leg r	617.5	596.2	21.3	3.6
foot right	485.8	469.1	16.7	3.6
u front leg l	618.9	597.6	21.3	3.6
foot left	512.1	494.4	17.7	3.6

Focusing on the simulation results of the global UV-A spectral part the same qualitative individual exposure pattern are obtained for measured (Fig. 34, left) and estimated (Fig. 34, right) data compared to the gobal UVER exposure pattern (Fig. 32). The strongest absolute (relative) global UV-A dose increase amounts to 56.4 Jm^{-2} (19%) and occurs for the trunk top (trunk front) anatomical zone (table 11). Analogously to the

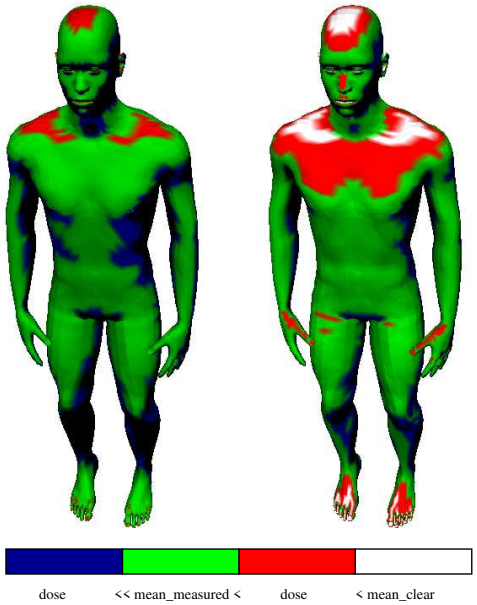

Fig. 34: Global individual UV-A exposure. Based on measurements (left) or clear-sky estimate (right).

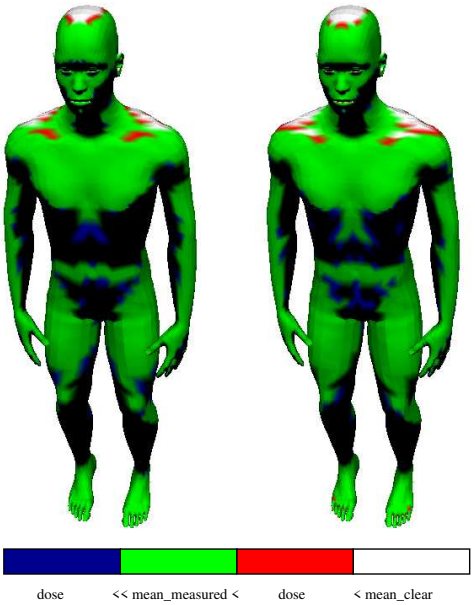

Fig. 35: Diffuse individual UV-A exposure. Based on measurements (left) or clear-sky estimate (right).

personal diffuse UVER exposure (Fig. 33) the comparison of the measured (Fig. 35, left) and estimated (Fig. 35, right) diffuse individual UV-A exposure also shows no qualitative change. For clear sky conditions the strongest increase of the individual diffuse UV-A exposure amounts to 5.4 Jm^{-2} for the trunk top anatomical zone. For all anatomical zones the relative diffuse UV-A exposure increase amounts to $2.4 - 2.5\%$ (table 12) being significantly smaller than the relative increase for diffuse UVER exposure (table 10).

Tab. 11: Global (g) UV-A doses and changes [Jm^{-2}]

zone	clear_g	meas_g	incr_g	%
skull	203.5	183.6	19.9	10.8
face	185.4	160.0	25.4	15.9
neck-front	192.0	165.0	27.0	16.4
trunk-top	365.9	309.5	56.4	18.2
trunk-front	227.9	191.5	36.4	19.0
shoulder left	262.2	231.0	31.2	13.5
lower arm ol	186.0	164.0	22.0	13.4
shoulder right	253.2	222.5	30.7	13.8
lower arm or	189.1	164.1	25.0	15.2
u front leg r	225.2	190.4	34.8	18.3
foot right	166.7	143.9	22.8	15.8
u front leg l	228.7	192.7	36.0	18.7
foot left	174.1	150.3	23.8	15.8

Tab. 12: Diffuse (d) UV-A doses and changes [Jm^{-2}]

zone	clear_d	meas_d	incr_d	%
skull	154.3	150.6	3.7	2.5
face	115.7	113.0	2.7	2.4
neck-front	117.8	115.0	2.8	2.4
trunk-top	225.9	220.5	5.4	2.4
trunk-front	128.8	125.7	3.1	2.5
shoulder left	186.3	181.8	4.5	2.5
lower arm ol	127.3	124.2	3.1	2.5
shoulder right	176.5	172.3	4.2	2.4
lower arm or	120.3	117.4	2.9	2.5
u front leg r	130.9	127.7	3.2	2.5
foot right	103.0	100.5	2.5	2.5
u front leg l	131.2	128.0	3.2	2.5
foot left	108.5	105.9	2.6	2.5

In analogy to the simulation results for global UVER and global UV-A the results for the global UV-B spectrum also show an individual exposure pattern (Fig. 36) with head, trunk top and front and the upper legs receiving the highest global UV-B dose amount (table 13). The highest relative dose increase is observed for the trunk front anatomical zone (18.6%), the highest absolute dose increase occurs for the trunk top zone. Regarding the difference of the simulated individual exposure to diffuse UV-B radiation based on measured (Fig. 37, left) and estimated (Fig. 37, right) data the same exposure pattern is observed as for both, the simulation results based on diffuse UVER (Fig. 33) and diffuse UV-A radiation (Fig. 35). The maximum absolute diffuse UV-B dose increase amounts to 31.4 Jm^{-2} for the trunk top zone with the relative diffuse dose increase amounting to 3.9% for all anatomical zones (table 14).

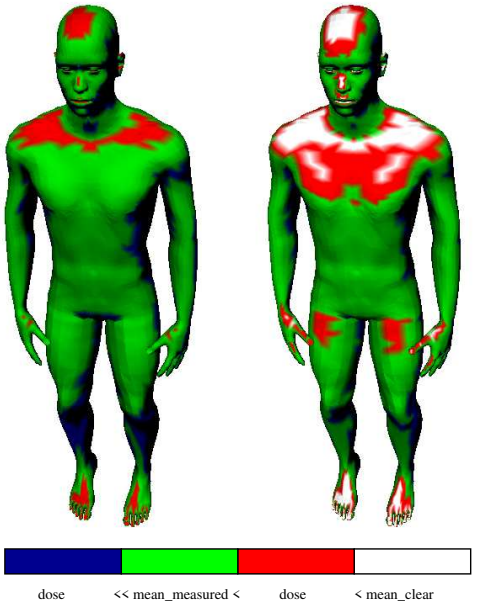

Fig. 36: Global individual UV-B exposure. Based on measurements (left) or clear-sky estimate (right).

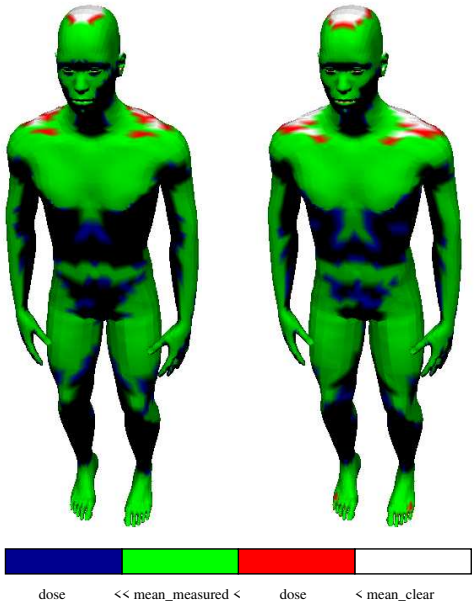

Fig. 37: Diffuse individual UV-B exposure. Based on measurements (left) or clear-sky estimate (right).

Tab. 13: Global (g) UV-B doses and changes [Jm^{-2}]

zone	clear_g	meas_g	incr_g	%
skull	941.7	835.1	106.6	12.8
face	950.5	816.1	134.4	16.5
neck-front	996.1	852.5	143.6	16.8
trunk-top	1970.8	1665.6	305.2	18.3
trunk-front	1242.2	1047.2	195.0	18.6
shoulder left	1292.8	1123.5	169.3	15.1
lower arm ol	912.0	794.6	117.4	14.8
shoulder right	1251.2	1086.0	165.2	15.2
lower arm or	957.7	825.3	132.4	16.0
u front leg r	1212.3	1025.9	186.4	18.2
foot right	849.6	729.4	120.2	16.5
u front leg l	1239.4	1046.7	192.7	18.4
foot left	888.9	762.9	126.0	16.5

Tab. 14: Diffuse (d) UV-B doses and changes [Jm^{-2}]

zone	clear_d	meas_d	incr_d	%
skull	573.8	552.4	21.4	3.9
face	430.4	414.3	16.1	3.9
neck-front	438.1	421.7	16.4	3.9
trunk-top	839.9	808.5	31.4	3.9
trunk-front	478.8	460.9	17.9	3.9
shoulder left	692.7	666.8	25.9	3.9
lower arm ol	473.3	455.6	17.7	3.9
shoulder right	656.3	631.8	24.5	3.9
lower arm or	447.3	430.6	16.7	3.9
u front leg r	486.6	468.5	18.1	3.9
foot right	382.9	368.6	14.3	3.9
u front leg l	487.7	469.5	18.2	3.9
foot left	403.5	388.5	15.0	3.9

Simulation results (17.8.2016)

The simulation results of estimating the meteorological influence on individual UVER exposure on 17 August 2016 is summarized in the following section. In general, the

Tab. 15: Global (g) UVER dose changes

zone	clear_g	meas_g	incr_g	%
skull	1061.2	1007.1	54.1	5.4
face	1070.7	998.0	72.7	7.3
neck-front	1128.4	1049.7	78.7	7.5
trunk-top	2204.6	2034.0	170.6	8.4
trunk-front	1400.6	1291.6	109.0	8.4
shoulder left	1492.0	1397.7	94.3	6.7
lower arm ol	1083.3	1016.2	67.1	6.6
shoulder right	1365.8	1281.7	84.1	6.6
lower arm or	1049.8	981.4	68.4	7.0
u front leg r	1367.0	1263.3	103.7	8.2
foot right	945.9	881.3	64.6	7.3
u front leg l	1397.9	1290.4	107.5	8.3
foot left	1006.6	937.1	69.5	7.4

Tab. 16: Diffuse (d) UVER dose changes

zone	clear_d	meas_d	incr_d	%
skull	656.6	654.2	2.4	0.4
face	492.5	490.7	1.8	0.4
neck-front	501.3	499.5	1.8	0.4
trunk-top	961.1	957.6	3.5	0.4
trunk-front	547.9	545.9	2.0	0.4
shoulder left	792.6	789.7	2.9	0.4
lower arm ol	541.6	539.6	2.0	0.4
shoulder right	751.1	748.3	2.8	0.4
lower arm or	511.9	510.0	1.9	0.4
u front leg r	556.9	554.8	2.1	0.4
foot right	438.1	436.5	1.6	0.4
u front leg l	558.2	556.1	2.1	0.4
foot left	461.8	460.1	1.7	0.4

Tab. 17: Global (g) UV-A dose changes

zone	clear_g	meas_g	incr_g	%
skull	216.8	213.5	3.3	1.5
face	214.4	208.6	5.8	2.8
neck-front	225.3	219.0	6.3	2.9
trunk-top	434.3	420.3	14.0	3.3
trunk-front	276.5	267.2	9.3	3.5
shoulder left	299.6	292.7	6.9	2.4
lower arm ol	218.1	213.3	4.8	2.3
shoulder right	275.0	269.1	5.9	2.2
lower arm or	211.0	205.8	5.2	2.5
u front leg r	270.6	261.9	8.7	3.3
foot right	189.6	184.6	5.0	2.7
u front leg l	276.3	267.2	9.1	3.4
foot left	201.4	195.9	5.5	2.8

Tab. 18: Diffuse (d) UV-A dose changes

zone	clear_d	meas_d	incr_d	%
skull	141.5	143.4	-1.9	-1.3
face	106.1	107.6	-1.5	-1.4
neck-front	108.0	109.5	-1.5	-1.4
trunk-top	207.2	209.9	-2.7	-1.3
trunk-front	118.1	119.7	-1.6	-1.3
shoulder left	170.8	173.1	-2.3	-1.3
lower arm ol	116.7	118.3	-1.6	-1.4
shoulder right	161.9	164.1	-2.2	-1.3
lower arm or	110.3	111.8	-1.5	-1.3
u front leg r	120.0	121.6	-1.6	-1.3
foot right	94.4	95.7	-1.3	-1.4
u front leg l	120.3	121.9	-1.6	-1.3
foot left	99.5	100.9	-1.4	-1.4

simulation results for total UVER , the UV-A and the UV-B spectral parts reflect the significantly smaller cloud influence on the individual UVER exposure. Compared to the day before the UVER doses of 17 August 2016 amount to less than half (cf. tables 9, 15) with the maximum dose increase for the diffuse UVER being negligibly small amounting to only 3.5 Jm^{-2} (0.4%) (cf. table 16). The main difference between the simulation results of both days occurs for the UV-A dose increase which is positive (negative) for the global

(diffuse) UV-A spectral part, respectively. Thus, in contrast to the previous paragraph the description of the 17 August simulation results focuses on the UV-A spectral only.

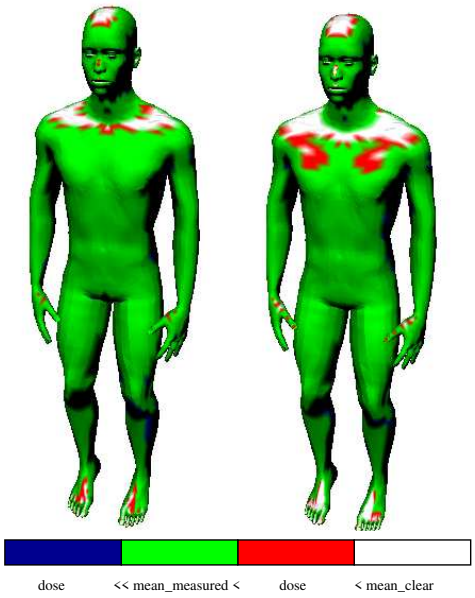

Fig. 38: Global individual UV-A exposure. Based on measurements (left) or clear-sky estimate (right).

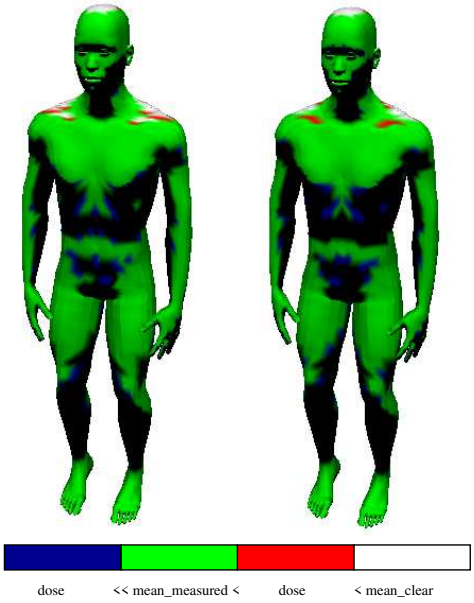

Fig. 39: Diffuse individual UV-A exposure. Based on measurements (left) or clear-sky estimate (right).

The exposure pattern for global UV-A radiation on 17 August (Fig. 38) shows qualitatively a very similar character like the respective pattern on 16 August (Fig. 34). The anatomical zone with the strongest relative UV-A dose increase is the upper front leg left (3.4 %) whereas the trunk top zone received the strongest absolute UV-A dose increase amounting to 14 Jm^{-2} (cf. tab. 17). In contrast to the global UV-A spectral part the diffuse UV-A doses for clear-sky conditions decrease for all anatomical zones by nearly the same relative amount ranging between 1.3 and 1.4 % (table 18). The strongest absolute diffuse UV-A dose decreases occur for the left shoulder (-2.3 Jm^{-2}) and the trunk top (-2.7 Jm^{-2}), respectively.

Discussion

As indicated by the results presented in the previous paragraph personal exposure to solar UVER is strongly affected by cloud meteorological influence, especially the respective global parts. Regarding the observed global and diffuse UVER dose increases (Tab. 9, 10) for clear conditions on 16 August 2016 two major findings can be discussed: First, the global UVER dose increases much stronger than the diffuse UVER dose. The reason for this behaviour is the strongly enhanced direct solar UVER irradiance component during clear sky conditions. Secondly, the relative diffuse UVER dose increase amounts to 3.6% for all anatomical zones considered which reflects the isotropic treatment of diffuse radiation in the SimUVEx model as introduced in section 2.7. Analogously, these conclusions are valid for both, the UV-A and the UV-B components (global and diffuse), respectively.

The comparison of UVER, UV-A and UV-B doses (global and diffuse) indicates much lower UV-A doses (cf. Tab. 9, 11 and 13) reflecting the fact that the respective data sets

represent erythemally weighted doses. Thus, due to a small overall erythemally weighted global (diffuse) UV-A dose, the global (diffuse) UVER dose is dominated by a strong global (diffuse) UV-B contribution. With respect to the diffuse UV-A and UV-B dose increases, the relative diffuse UV-A dose increase on 16 August 2016 is smaller (2.4 - 2.5%) compared to the respective relative UV-B dose increase (3.9%). Based on the Rayleigh scattering theory these results can be explained by stronger scattering to occur for shorter wavelengths. In contrast to 16 August 2016, the meteorological conditions on 17 August

Tab. 19: Dose increases (%) on 16. and 17.8.2016 (horizontal)

date	UV-A		UV-B		UVER	
	global	diffuse	global	diffuse	global	diffuse
16.8.	23.5	2.5	19.0	4.1	19.7	3.8
17.8.	3.5	-1.3	10.1	1.1	8.7	0.3

2016 were characterized by less cloud coverage as indicated by the much smaller differences between measured and estimated doses of global and diffuse UVER (Tab. 15, 16), respectively. The trunk-top anatomical zone, for example, is characterized by a total UVER dose increase of 371 (170.6) Jm^{-2} on 16 (17) August 2016 indicating the cloud influence to be half on the second day. In addition to the previously discussed conclusions of the 16 August results being also valid for the data sets of 17 August 2016 another observation occurs for the diffuse UV-A dose only. Contrary to an increasing global UV-A dose (Tab. 17) the diffuse UV-A dose decreases (Tab. 18) for clear sky conditions. Based on the results of 16 August 2016 (cf. Tab. 12) the diffuse UV-A dose is also expected to increase as described above. The now observed diffuse UV-A dose decrease results from the weaker Rayleigh scattering in the UV-A spectral range being overcompensated by the increased direct radiation component for clear conditions in this case.

The comparison of the relative anatomical zone dose increases of global and diffuse UVER (UV-A, UV-B) for both days with the respective relative horizontal dose increase of global and diffuse UVER (UV-A, UV-B) (Tab. 19) shows the respective relative horizontal dose increase to be a conservative estimate for the anatomical zone being characterized by the strongest relative UVER (UV-A, UV-B) dose change due to cloud meteorological influence. For example, the relative global trunk front anatomical zone UV-A dose increase on 16 August 2016 amounts to 19% (Tab. 11) with the corresponding horizontal global UV-A dose increase amounting to 23.5% (Tab. 19), respectively. From these results it is concluded that a conservative estimate of the cloud meteorological impact on individual UVER exposure, in this case the relatively most affected anatomical zone, can be provided by calculating the respective relative dose changes for horizontally measured UVER data sets.

By comparing the simulated global and diffuse UV-A (UV-B) doses for different anatomical zones a pronounced dependency regarding the respective dose magnitude (global, diffuse) and the body location of the considered anatomical zones can be observed. Regarding this behaviour the simulation results indicate significant differences for both the trunk front and shoulder left anatomical zones of 16 August 2016 being discussed in the following. The shoulder left diffuse UV-A dose fraction amounts to 71.1% (78.7%) for clear (cloudy) conditions whereas the trunk front diffuse UV-A dose fraction only amounts to 56.5% (65.6%), respectively (cf. Tab. 11, 12). Thus, the diffuse UV-A dose fraction is larger than the direct component for both anatomical zones (direct = global - diffuse).

As expected the diffuse UV-A dose fraction is relatively higher for cloudy conditions due to the generally higher cloud induced scattering. The shoulder left diffuse UV-B dose fraction amounts to 53.5% (59.4%) whereas the trunk front diffuse UV-B dose fraction amounting to 38.5% (44.0%) for clear (cloudy) conditions, respectively (cf. Tab. 13, 14). Analogously to the results for the UV-A spectral part the diffuse UV-B dose fraction of both anatomical zones is significantly lower for clear conditions. However, the relative UV-B dose differences (clear vs. cloudy) are generally smaller than the corresponding relative UV-A dose differences of the respective anatomical zone. The relative diffuse UV-B dose fraction of both anatomical zones is also observed to be significantly lower compared to the relative diffuse UV-A dose fraction for both clear and cloudy conditions. In contrast to the results for the UV-A spectal part the trunk front relative direct UV-B dose fraction is actually larger than the corresponding diffuse fraction for both clear and cloudy conditions. By concluding, these results show the magnitude of both the relative direct and diffuse UV-A (UV-B) dose fraction to strongly depend on the specific location of an anatomical zone. For the case presented, the relative diffuse dose fractions are significantly larger during cloudy conditions. Hereby the cloud influence is twice as large for the relative diffuse UV-A compared to the corresponding relative UV-B doses. For all anatomical zones investigated in this case, the UV-B contribution to the total individual UVER exposure is nearly five times larger than the UV-A part. Thus, a strong reduction of the total individual UVER exposure can be reached by especially reducing its UV-B contribution. For cloudy conditions especially the diffuse UVER must not be underestimated due to a higher relative contribution to the global UVER dose.

4.3 The impact of a low-ozone event and stratocumulus clouds on personal UVER exposure

Synoptic situation and ozone measurements

On 6 April, the synoptic situation over the British Isles was characterized by an extended high pressure system with the surface anticyclone centered over South Ireland (Fig. 40, left). On 7 April, the high pressure system had moved further eastward over the British Isles and slightly weakened with respect to its surface pressure (Fig. 40, right). Thus, there was no major change in the general synoptic pattern over England from 6 April to 7 April. On the other hand two major large scale developments occurred: First, the trough over eastern Europe moved further south now being located over Romania. Second, a strong extratropical cyclone formation took place over the Atlantic subsequently approaching Iceland.

On both measurement days (6 and 7 April 2017) the atmospheric state was characterized by two major features: Large scale subsidence due to the governing anticyclone in conjunction with a general northwesterly flow on the one hand and a planetary boundary layer (PBL) with turbulent mixing on the other hand. The adiabatic warming of the descending airmasses within the anticyclone was responsible for cloud dissipation at high and medium tropospheric levels as well as for the development of a strong temperature inversion at the PBL top being roughly located at 900 hPa as indicated by the radio soun-

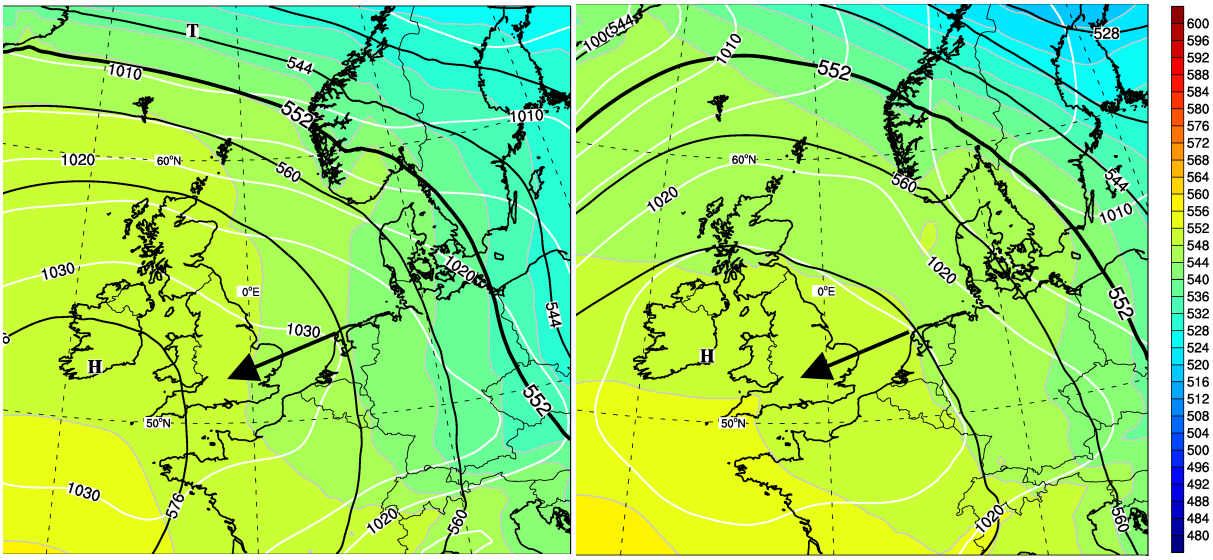

Fig. 40: 500 hPa geopotential [gpdam] (black isopleths), surface pressure [hPa] (white isopleths) and relative topography 500-1000 [gpdam] (isoareas), 6 April 1200 UTC (left) and 7 April 1200 UTC (right). data source: NCEP-GFS model analysis. The Didcot area is indicated by black arrows.

ding data of Camborne for both days (not shown). Radiatively induced turbulence generated a well-mixed airmass within the PBL being characterized by a dry adiabatic lapse rate. With increasing radiative forcing until noon the turbulent mixing strengthened. The radio soundings show relatively humid air within the PBL resulting from the generally weak advection of maritime air southward. SSC development started at 1150 LT on 6 April and at 1050 LT on 7 April as indicated by distinct UVER attenuation periods (see Fig. 42). On both days the cloud occurrence lasted until about 1500 LT when radiative turbulence forcing had weakened. Clear conditions occurred during the morning hours, the late afternoon, in the evening and in the night period. The very similar cloud and airmass characteristics on both days are also confirmed by the meteorological measurements indicating a very similar diurnal temperature cycle (not shown) and temperature range of about 13 K (4 - 17 °C on 6 April and 3 - 16 °C on 7 April). Moreover, the measured wind data indicates a weak generally westerly flow ($< 1\ ms^{-1}$ mean speed) with low variability during the night and mean wind speeds ranging between 1 - 2 ms^{-1} with high variability during the diurnal turbulent mixing period (not shown).

The reason for predominantly clear conditions over southern England and especially in the Didcot area on both days, except for the turbulence induced SSC, is a significant orographic influence. Several mountain ridges in England, such as the Pennies and Cotswold Hills, the Chiltern Hills, the North Wessex Downs, the Shropshire Hills and the northern welsh mountains, stretch mainly in a southwest-northeast direction or at least some parts of them have a west-east orientation. Because of the relatively shallow PBL, reaching not higher than 900 hPa, these mountain ridges significantly influence the northwesterly flow and especially the cloud layer in form of weak foehn effects (Bott 2016) without precipitation on the windward side yielding westerly winds as indicated by measured data (wind shift) and cloud free areas (satellite imagery) alee. Based on the above arguments, on 6 and 7 April the mesoscale meteorological conditions (Orlanski 1975) may be treated as rather similar, thus justifying a direct comparison of the measured radiation data. In

addition the cloud optical depths on both days ranged between 0.05 - 0.6 (global) and 0.05 - 0.2 (diffuse), respectively, indicating almost identical cloud characteristics for the respective time periods on both days. On 6 April, lower ozone contents were observed over the western parts of Europe with a global hemispheric minimum over the northern

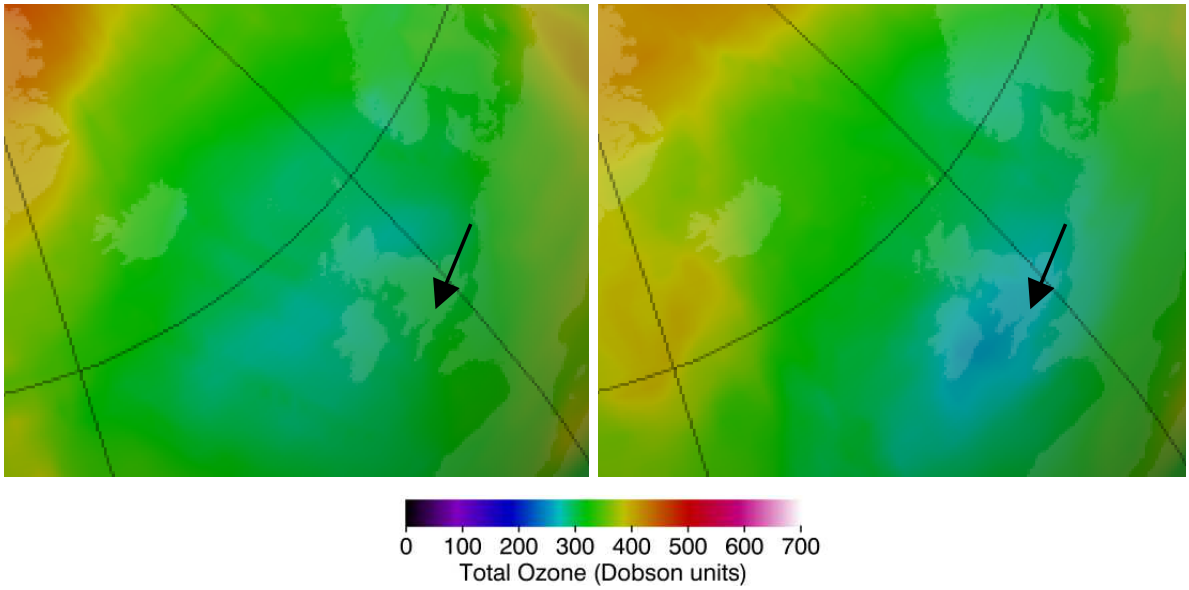

Fig. 41: Stratospheric total ozone content over the British Isles, 6 April (left) and 7 April (right). Source: https://ozonewatch.gsfc.nasa.gov/NH.html. The arrows indicate the Didcot area.

parts of the British Isles (Fig. 41, left). The ozone content over the Didcot area in southern England, where the dosimetric measurements were performed, amounted to more than 300 *DU*. Higher total ozone content values at higher latitudes result from the general stratospheric circulation dynamically advecting air masses from the ozone generating regions in the tropics poleward (Brewer 1949).

On 7 April, the large-scale stratospheric ozone distribution showed no change in its general behaviour, however, a distinct minimum occurred over the British Isles compared to the day before clearly indicating the presence of a low-ozone event (Fig. 41, right). Now, the total ozone amount over large parts of Great Britain including the measurement site on Harwell campus was distinctly below 300 *DU*. Stratospheric ozone measurements at Reading (about 35 *km* south-east of Didcot), offered by the Department for Environment, Food & Rural Affairs of the British Government (Data source: https://uk-air.defra.gov.uk/data/ozone-data), showed a decrease of the total ozone column from 315 *DU* on 6 April to 281 *DU* on 7 April indicating an ozone mini-hole according to McCormack and Hood (1997). In addition, the 34 *DU* drop of total stratospheric ozone indicates a low-ozone event based on the definition given by Newman et al. (1988). The measurement period is characterized by an ozone content being more than two times lower than the ozone content standard deviation from the long-term monthly mean of the measurement site. The long-term (14 years) monthly mean for stratospheric ozone in April at Reading site amounts to 369 *DU* with a standard deviation of 16 *DU*. Thus the ozone mini-hole during the measurement period occurs during a more general low-ozone episode. Comparing the stratospheric ozone distribution (Fig. 41) to the location of the high pressure system (Fig. 40) indicates a strong correlation between both events as suggested in previous studies (Hoinka et al. 1996; Iwao and Hirooka 2006).

Methods and results

In this section the results of comparing the UVER datasets of 6 April and 7 April are described. First the meteorological influence in form of SSC coverage affecting the daily UVER dose will be investigated for both days. Next, the low-ozone event's effect on the UVER dose amount is quantified to be able to estimate its influence on the meteorological effect. The method used to quantify the meteorological influence is to compare the measured UV-A and UV-B dosimeter data to an estimated dataset for clear sky conditions for the same time period by means of the cloud modification factor (CMF). Calbó et al. (2005) defined the CMF as

$$CMF = \frac{UV_m}{UV_e} \tag{4.30}$$

where UV_m is the measured and UV_e the estimated irradiance or related doses assuming clear sky (In eq. 4.30, 4.31 and 4.33, the term $UV_{(...)}$ indicates either total UV, UV-B or UV-A, respectively). The ozone mini-hole impact on UVER will be analyzed based on the calculation of the radiation amplification factor (RAF) as given by (Madronich 1993)

$$\frac{UV_{e,1}}{UV_{e,0}} = \left(\frac{TOC_1}{TOC_0}\right)^{-RAF} \tag{4.31}$$

with $TOC_{0,1}$ the total ozone contents of 6 April (index 0) and 7 April (index 1). The clear-sky estimation during cloudy conditions is obtained by combining measured data (morning hours) and non-linear regression analysis data. The regression was performed based on the undisturbed parts of measured UVER data during the morning (until 1100 LT on 6 April and 1050 LT on 7 April) and the afternoon (after 1700 LT on 6 April and 1450 LT on 7 April, see also the vertical red lines in Fig. 35) by fitting a gaussian function of the type

$$f(x) = k_0 exp\left(-\frac{(x-\mu)^2}{2\sigma^2}\right) \tag{4.32}$$

to the selected measured UVER data with μ the expected value, σ^2 the variance and k_0 a constant. To be able to compare the UVER doses for both days the same time intervals were chosen for the calculation of CMF, RAF and the UVER doses stretching from 0630-1530 LT (long time interval, hereafter LI) as well as from 1100-1500 LT (short time interval, hereafter SI). In order to evaluate the low-ozone event's effect and the SSC influence in independently modifying the UVER doses, the CMF (eq. 4.30) will be included into the RAF defining equation (eq. 4.31) resulting in a RAF split introduced by

$$\frac{log\left(\frac{CMF_0}{CMF_1}\right)}{log\left(\frac{TOC_1}{TOC_0}\right)} + \frac{log\left(\frac{UV_{m,1}}{UV_{m,0}}\right)}{log\left(\frac{TOC_1}{TOC_0}\right)} = -RAF = -(COF + RAF_m) \tag{4.33}$$

with the Radiation Amplification Factor RAF_m calculated based on measured UVER doses and the new cloud ozone factor COF. The COF is defined as the logarithmic ratio of the change in cloud attenuation expressed by the CMF ratio as well as the change in total stratospheric ozone. Thus, the COF describes the weight of the two independently acting processes (cloud attenuation and ozone decrease) in modifying surface UVER doses for the selected event.

Meteorological influence on UVER doses

As mentioned above, clear-sky diffuse and global UVER estimates will be compared to the corresponding measured data by calculating the corresponding *CMF*. The comparison clearly shows the SSC meteorological influence on the amount of UVER reaching the ground as indicated by the attenuated measured data during noon and afternoon of 6 and 7 April (Fig. 42).

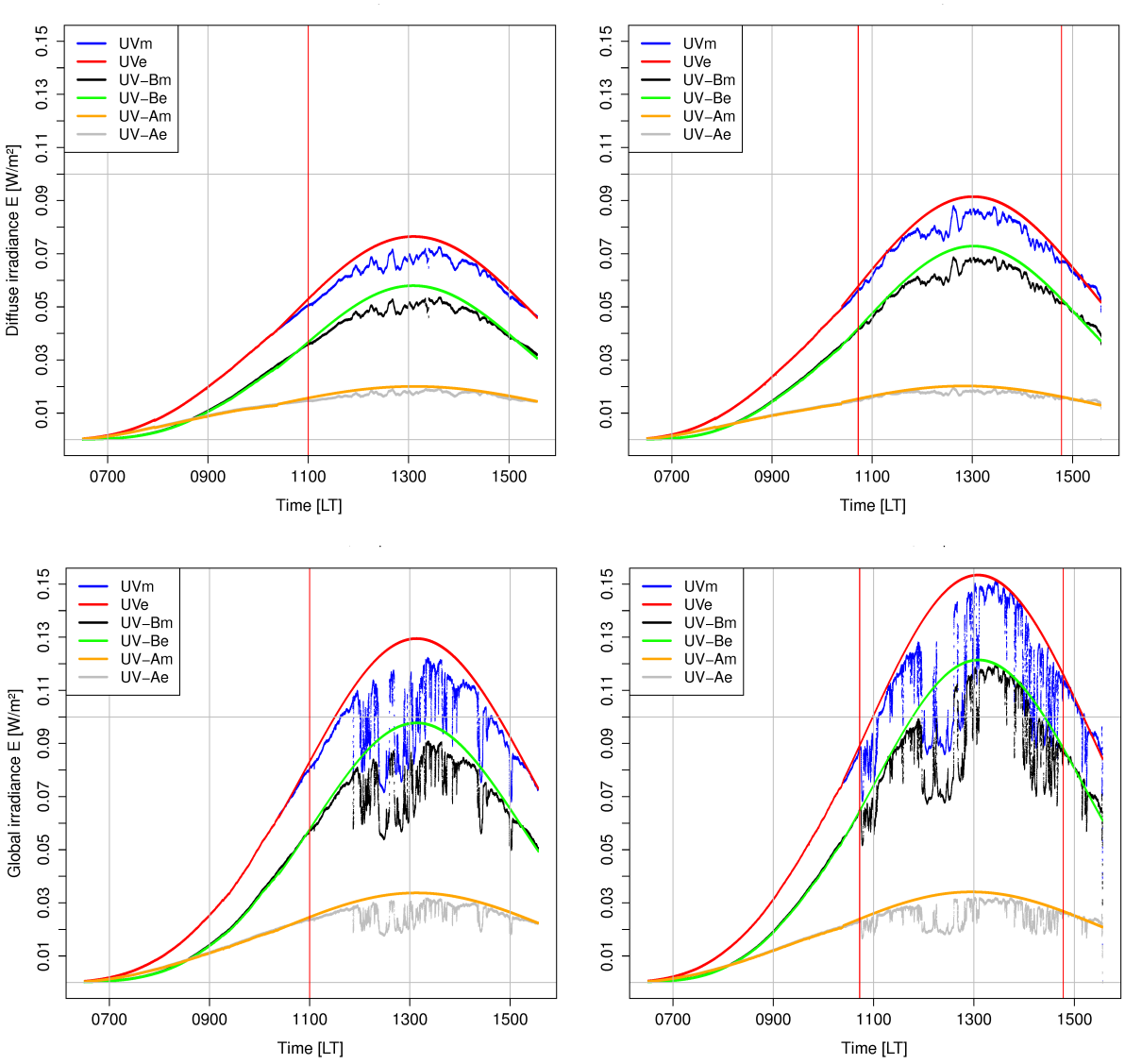

Fig. 42: SSC influence on diffuse surface UVER on 6 (upper left) and 7 April (upper right) as well as on global surface UVER on 6 (lower left) and 7 April (lower right). The separation between the undisturbed (morning and afternoon) and the cloudy time periods is indicated by vertical red lines.

The resulting estimated effects of SSC in attenuating the total global and diffuse UVER doses as well as its UV-A and UV-B parts are summarized in the following table (Tab. 20).

Tab. 20: UVER doses and *CMF* on 6 and 7 April

	6 April			7 April		
	UV	UV-B	UV-A	UV	UV-B	UV-A
0630 - 1530 LT (LI)	diffuse UVER doses					
measured [Jm^{-2}]	1334	936	398	1604	1198	405
estimated [Jm^{-2}]	1411	990	421	1678	1254	424
CMF	0.945	0.945	0.945	0.956	0.955	0.955
1100 - 1500 LT (SI)	diffuse UVER doses					
measured [Jm^{-2}]	915	671	244	1106	859	248
estimated [Jm^{-2}]	988	723	265	1177	912	266
CMF	0.926	0.928	0.921	0.94	0.942	0.932
0630 - 1530 LT (LI)	global UVER doses					
measured [Jm^{-2}]	2030	1441	589	2414	1821	593
estimated [Jm^{-2}]	2263	1604	659	2695	2023	672
CMF	0.897	0.898	0.894	0.896	0.90	0.882
1100 - 1500 LT (SI)	global UVER doses					
measured [Jm^{-2}]	1420	1047	373	1688	1318	369
estimated [Jm^{-2}]	1645	1206	440	1950	1507	444
CMF	0.863	0.868	0.848	0.866	0.875	0.831

A significant difference occurs especially between the UV-A and the UV-B spectral ranges concerning the irradiance amplitude. While the erythemally weighted UV-A irradiance reaches values up to 0.02 Wm^{-2}, the erythemally weighted UV-B irradiance reaches peak values close to 0.05 Wm^{-2}. These differences result from the application of the erythemal action spectrum on the measured UV data, thus leading to much higher contributions in the UV-B. The stronger Rayleigh scattering effect on the UV-B part is especially obvious before 0900 LT with UV-B irradiance values being lower than those of the UV-A part (Fig. 42) and a subsequently much stronger increase until noon due to the shorter penetration path through the atmosphere and, thus, less efficient scattering.

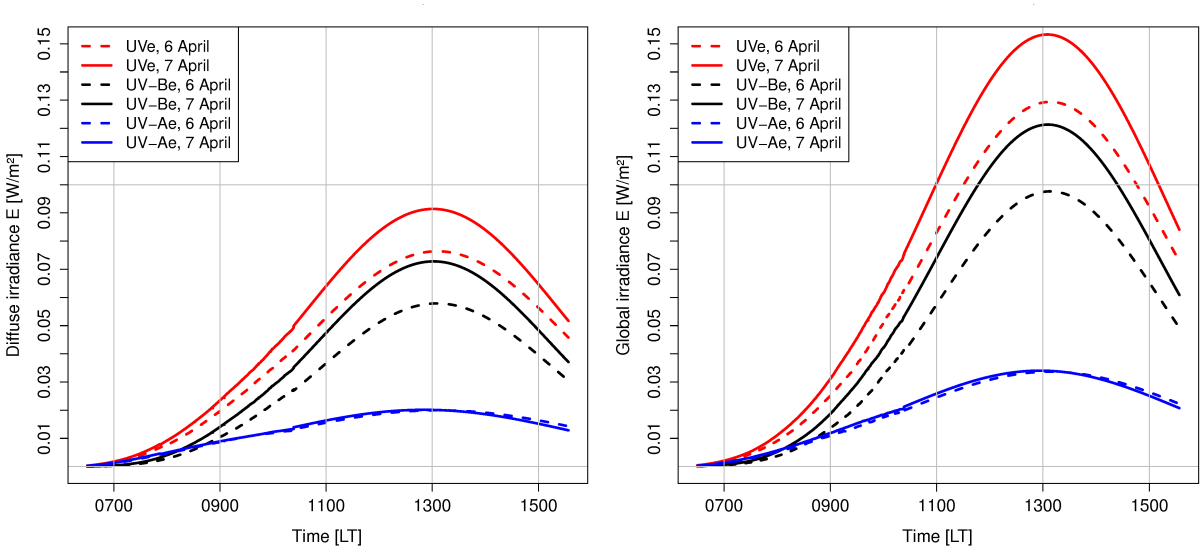

Fig. 43: Estimated diffuse and global UV irradiances for 6 and 7 April 2017.

Low-ozone event and UVER doses

The ozone mini-hole effects will be investigated by comparing the estimated clear sky UVER doses of 7 April with those of 6 April. To avoid some confusion analyzing those effects the estimated diffuse and global UVER doses of both days will be visualized separately. The visualization of the estimated UVER doses of 6 April and 7 April clearly shows the different behaviour for UV-A and UV-B spectral parts (Fig. 43). The differences between the estimated UVER doses as well as the values for RAF, RAF_m and COF (eqs. 4.31 and 4.33) are summarized in table 21.

Tab. 21: Estimated UVER dose increases, RAF and COF

	UV	UV-B	UV-A	UV	UV-B	UV-A
	diffuse			global		
0630 - 1530 LT (LI)	dose increases					
[Jm^{-2}]	267	264	3	432	419	13
%	18.9	26.7	0.7	19.1	26.1	2.0
RAF	1.52	2.07	0.06	1.51	2.03	0.17
RAF_m	1.62	2.16	0.15	1.52	2.06	0.05
COF	-0.10	-0.09	-0.09	-0.01	-0.03	0.12
1100 - 1500 LT (SI)	dose increases					
[Jm^{-2}]	189	188	1	305	301	4
%	19.1	26.0	0.3	18.5	25.0	1.0
RAF	1.53	2.03	0.03	1.49	1.95	0.08
RAF_m	1.66	2.16	0.14	1.51	2.02	-0.10
COF	-0.13	-0.13	-0.11	-0.03	-0.07	0.18

These results clearly indicate strong dose increases for the diffuse and global UV and UV-B parts during the low-ozone event but almost no changes for the diffuse and global UV-A portions. Therefore, the total UVER dose differences may almost completely be attributed to the strong UV-B dose increases. The calculation of the RAF, RAF_m and COF values, as previously introduced, is based on measured total ozone contents of 315 DU (6 April) and 281 DU (7 April).

Discussion

Low-ozone events are strongly correlated to large scale dynamic anticyclones as described in previous studies (Reed 1950; Newman et al. 1988; Iwao and Hirooka 2006). According to Iwao and Hirooka (2006) and Pérez et al. (2002) a combination of low-ozone isentropic airmass transport originating from lower latitudes and vertical upward motion causes a decrease in the lower stratospheric ozone content due to airmass losses on isentropic layers. The strong correlation between the high pressure system's location centred over the Irish Sea and the area of minimum ozone contents on 6 and 7 April is evident, both having moved further towards the southeast. Together with total ozone measurements from Reading a low-ozone event on 7 April is evident.

As expected, the results presented earlier indicate a clear distinction between the impact of SSC and the low-ozone event on measured surface UVER doses, both in magnitude and characteristics. While the SSC impact causes significant surface global and diffuse UVER dose decreases on both days, the lower stratospheric ozone contents lead to a strong surface UVER dose increase on 7 April (Table 20). The cloud influence shows a

highly variable behaviour on a timescale of seconds and minutes whereas the low-ozone effect seems to depend mainly on the solar zenith angle (SZA). By comparing the impacts of the ozone mini-hole and the SSC coverage on 7 April, the low-ozone event caused a diffuse (global) UV-B dose increase of 264 (419) Jm^{-2} while the SSC coverage yielded a reduction of only 55 (202) Jm^{-2}. Hence, compared to the SSC effect the low-ozone effect is five times larger for the diffuse UV-B part but only two times larger for the global UV-B part. For the UV-A part, on the other hand, the results show a six times larger SSC effect acting on both the diffuse and global LI doses.

The results given in Table 21 indicate the different behaviour of the two processes modifying the surface UVER doses, namely the SSC influence and the low-ozone event's effect. During the actually cloudy SI period significantly higher RAF values for the UV-B interval indicate the strong effect of decreased total ozone leading to increased diffuse and global UV-B doses. In comparison the RAF values for the respective UV-A parts remain negligibly small indicating that the effect of the low-ozone event is almost completely acting on the diffuse and global UV-B parts. Based on total LI UVER doses the RAF amounts to 1.52 indicating a relatively strong low-ozone event compared to mean RAF values of 1.29 ± 0.2 for ozone mini-holes over Valencia (Martínez-Lozano et al. 2011) or RAF values up to 1.25 at the island of Lampedusa (di Sarra et al. 2002). By introducing the CMF into the RAF defining equation (eq. 4.31), the RAF is decomposed into two parts called COF and RAF_m (cf. eq. 4.33). The new COF describes the ratio between the change in the SSC influence (CMF ratio) and the change in total ozone (TOC ratio). Thus, the relative strength of both processes acting during the same event but independently of each other can be determined. Regarding the SI period, the relative strength of the SSC influence is almost twice as large for the diffuse UV-B part ($COF = -0.13$) compared to the global UV-B interval ($COF = -0.07$) with a decreased cloud influence as indicated by the negative COF values. For the SI UV-A doses, on the other hand, a negative COF (-0.11) indicates weakened SSC influence for the diffuse part while an increased cloud influence is indicated for the global interval ($COF = 0.18$).

In addition, the defining equation of the COF (eq. 4.33) provides an adjusted RAF, called RAF_m, which is derived based on measured instead of estimated UVER doses. For a hypothetical low-ozone event with clear-sky conditions ($CMF = 1$) on both days, the COF vanishes according to equation 4.33 and thus RAF_m would be equal to RAF. The COF resumes positive (negative) values for an increased (decreased) cloud influence during the low-ozone event. It should be emphasized here, that a change in cloud influence is a result of meteorological processes and thus independent of changes in the total ozone amount. Assuming positive (negative) COF values and thus an increased (decreased) cloud influence on the second day, the RAF_m values would fall below (exceed) the RAF values, which is an over-(under)estimation of the RAF, respectively.

Considering the actually cloudy SI period and the diffuse UVER part for the case presented, the COF is characterized by negative values (Tab. 21). The correspondingly higher RAF_m values demonstrate the higher relative increase for measured compared to estimated UVER doses (Tab. 20). Regarding the global SI UVER part the COF and RAF_m behaviour can be described analogously except for the UV-A part. The application of equation 4.33 for the UV-A data results in a positive COF (0.18) indicating an increased SSC influence and a negative RAF_m (-0.10). In this case the negative RAF_m values indicates the overcompensation of the low-ozone event induced (small) UV-A dose increase by the increased SSC attenuation. From these results it is concluded that the

SSC influence is relatively smaller than the low-ozone event's effect as expressed by the *COF*. Especially for the UV-B spectral interval the SSC influence plays a minor role compared to the much stronger low-ozone related UVER dose increase. From a health protection and prevention point of view only the total UVER dose amounts matter in causing sunburn or even skin cancer after long-term UV exposure. In the present case, the total UVER dose was increased by 4.32 SED due to a low-ozone event while being attenuated by 2.81 SED as a result of SSC coverage finally indicating an additional erythemally active dose amount of 1.51 SED on 7 April (LI interval). Thus the SSC impact on UVER must not be underestimated being able to reduce the total UVER dose increase caused by the low-ozone event by about 65% for the case presented[2].

Application of the COF to spectral UVER data

In addition to the dosimeter measurements performed on 6 and 7 April 2017 spectral UV irradiance data was also gathered during the same time interval (Fig. 44, left). The spectroradiometer used for the measurements (Fig. 44, right) is of the type BTS2048-UV-S and newly fabricated by Gigahertz Optics GmbH. For further technical details the reader is referred to the user manual (www.gigahertz-optik.de/de-de/produkt/BTS2048-UV).

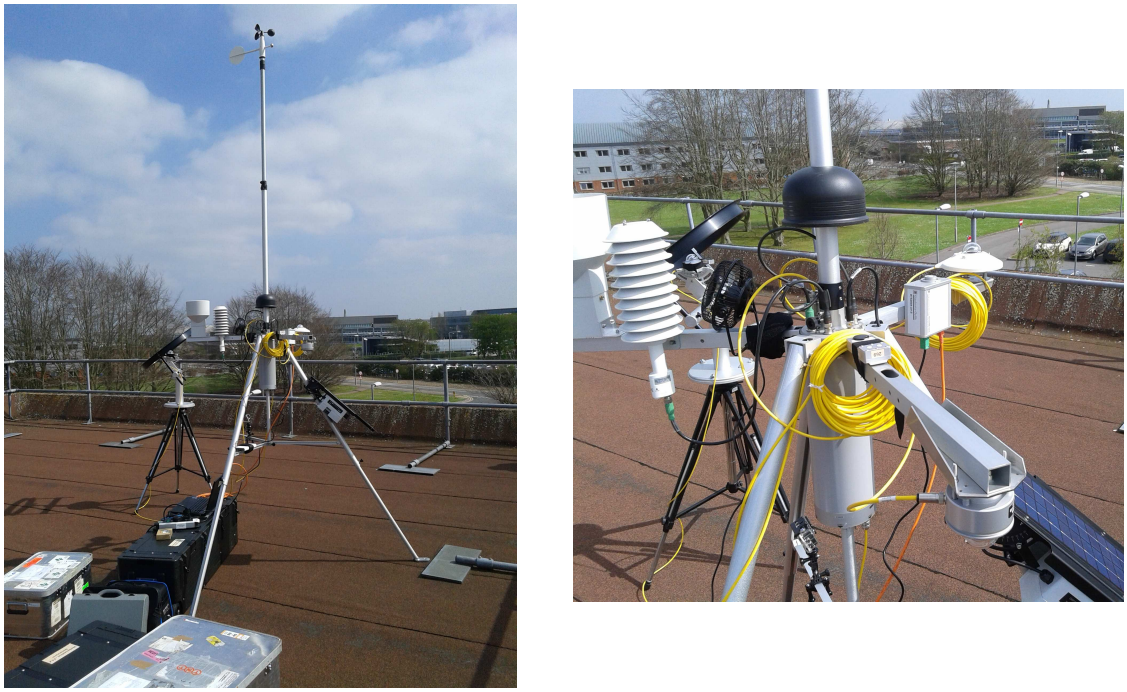

Fig. 44: The mobile weather station on 6 April 2017 on top of the PHE building in Didcot, England (left). The spectroradiometer gathering UV radiation (white box) was assembled on the sensor bar next to the pyranometer (right).

On 6 (7) April 2017 the spectroradiometer data was gathered from 9:52 - 17:08 (9:35 - 16:17) UTC+2 thus covering the radiatively most intense period of the respective day.

[2]The previously discussed results have already been published in Kelbch et al. (2019).

The measurements were taken every minute during the respective time interval of both days with each measurement being the average of three individual scans. The sensor gathered UV irradiance within the wavelength interval stretching from 200 - 400 nm with a 0.2 nm increment. As UV-C radiation does not reach the ground only the spectral interval ranging from 280 - 400 nm is considered for the following investigations.

In the previous paragraph both the cloud influence as well as the effect of an ozone mini-hole on the exposure to surface UVER were evaluated and discussed. This analysis was mainly based on the comparison of time-integrated dosimetric UVER data, i.e. UVER doses of the total UV, the UV-A and the UV-B spectral parts, respectively. In the following the impact of both effects (clouds and low-ozone event) on the amount of surface UVER will be evaluated based on UV spectroradiometer data by calculating the mean SI spectral COF. For this, the erythemal action spectrum (CIE, 1987) is applied to the measured spectral UV irradiances. Next, the considered UV interval (280 - 400 nm) is subdivided into six parts ranging from 280 - 299.8 nm, 300 - 319.8 nm, 320 - 339.8 nm, 340 - 359.8 nm, 360 - 379.8 nm as well as from 380 - 400 nm, respectively. There is no specific reason for choosing six spectral intervals other than to create reasonable parts of the considered total UV interval with the first two parts covering the UV-B and the other four parts covering the UV-A range. The spectral lines with the largest variability is determined for each of the six spectral parts by applying the R-package funtion stat.desc() whereby the six lines with the highest standard deviation were selected. The underlying assumption is to attribute the temporal UVER variability during the measurement period of both days to the cloud influence only. Consequently the most cloud sensitive spectral lines of each of the six spectral intervals are obtained (Fig. 45). Compared to 6 April the

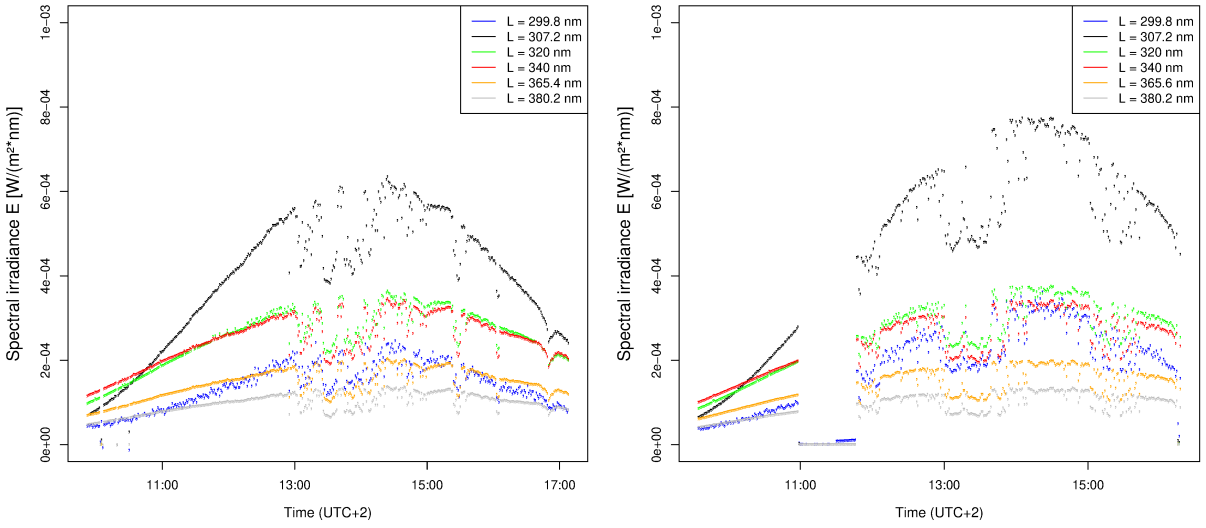

Fig. 45: Spectral UVER measurements of the most sensitive spectral lines (L) of each of the six spectral parts on 6 (left) and 7 (right) April 2017 in Didcot.

spectral UVER is significantly more intense on 7 April which is due to the low-ozone event occuring on the second day only. On both days the SZA dependency of the Rayleigh scattering is evident in the morning and afternoon hours, respectively, with stronger scattering occurring the shorter the wavelength. Unfortunately a spectroradiometer failure between 10:56 and 11:48 (UTC+2) on 7 April 2017 lead to some data loss (Fig. 45, 46 right).

Most importantly for the further investigations the spectral line with wavelength 307.2 *nm* (hereafter: SL307.2) is the spectral line with both the highest cloud sensitivity and radiative intensity of the whole UVER spectrum. Thus SL307.2 was selected to determine the time periods with clear conditions being subsequently used for a nonlinear regression to derive a clear sky estimate for both days. As previously introduced, e.g. equation (4.32), a gaussian function was fitted to the selected measured clear sky data sets. Measured data from the morning and afternoon hours (clear conditions) are combined with regression data (cloudy time periods) of both days resulting in an estimated clear sky data set for each day (e.g. Fig. 46 for SL307.2). The minimum cloud modification factor

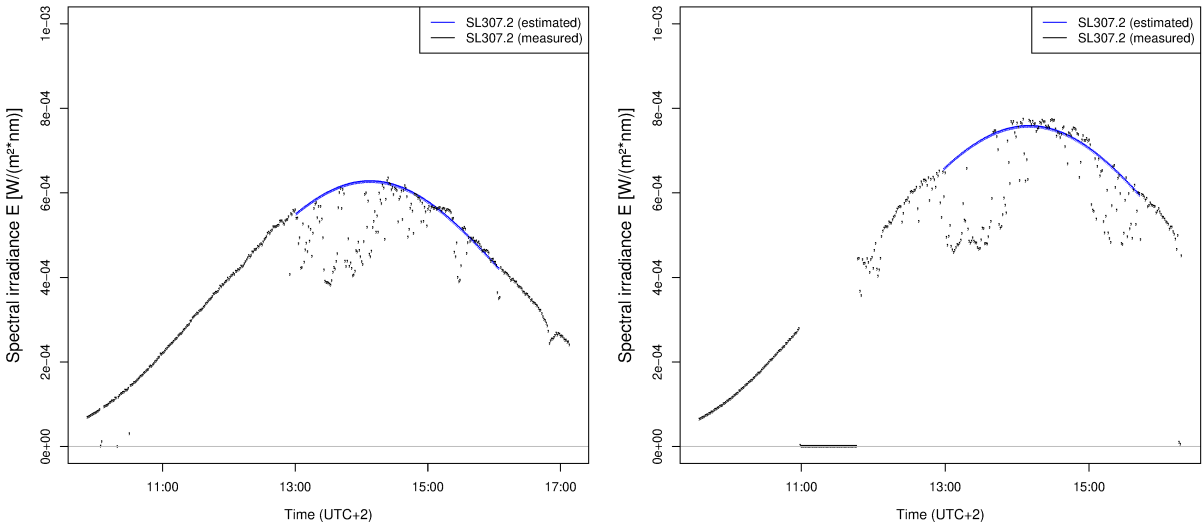

Fig. 46: Measured and estimated SL307.2 on 6 (left) and 7 (right) April 2017 in Didcot.

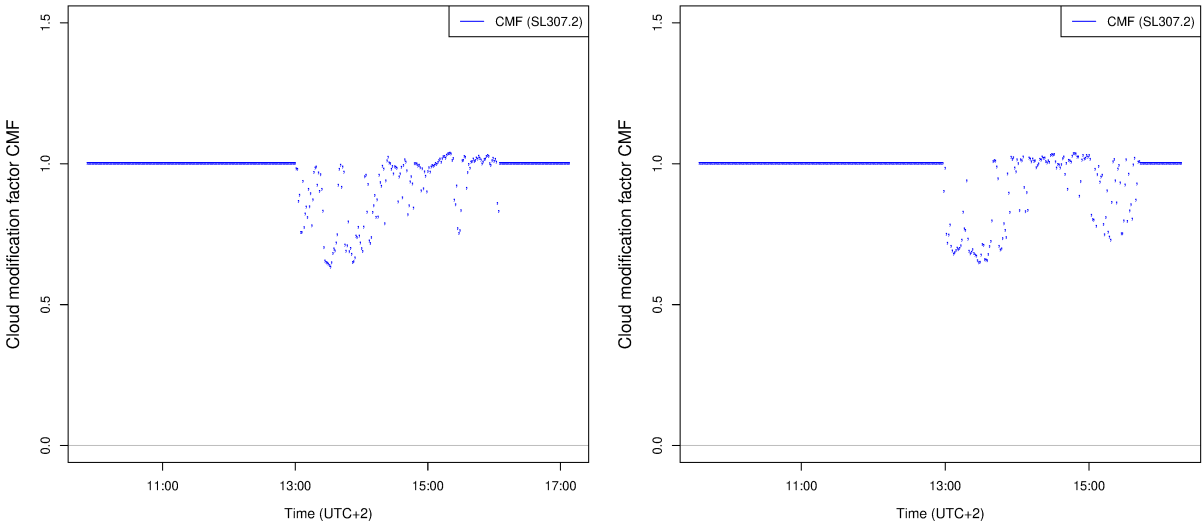

Fig. 47: CMF values of SL307.2 on 6 (left) and 7 (right) April 2017 in Didcot.

of SL307.2 (CMF) is calculated based on (4.30) for both days to determine the moments of maximum cloud coverage during both measurement periods with minimum CMF amounting to 0.632 (0.648) at 13:32 (13:28) UTC+2 on 6 (7) April (Fig. 47). The reason for CMF

equaling exactly zero during the morning and afternoon of both days is that the clear sky estimate data set is composed of measured data during those time periods. As the incoming radiation is most attenuated at 13:32 (13:28) UTC+2 on 6 (7) April the spectral cloud modification factors (CMF_s) are calculated for the respective time (Fig. 48). The CMF_s may be interpreted as the 'spectral finger print' of shallow stratocumulus clouds at the time of maximum coverage on both measurement days which is roughly during the radiatively most intense time period around noon. The high CMF variability for spectral

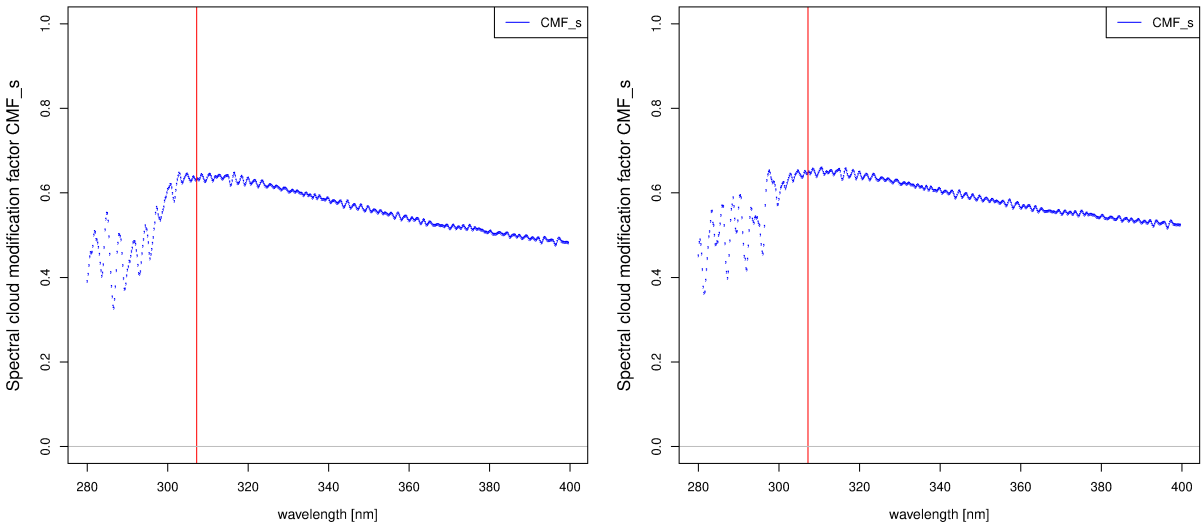

Fig. 48: Spectral CMF at 13:32 UTC+2 on 6 (left) and at 13:28 UTC+2 on 7 (right) April 2017 in Didcot.

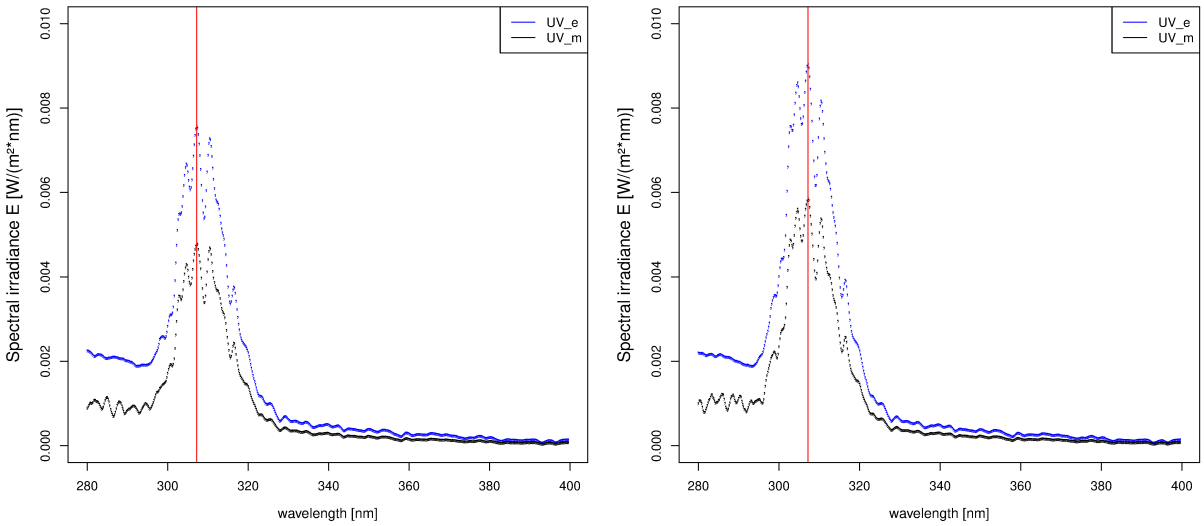

Fig. 49: Spectral UVER at 13:32 UTC+2 on 6 (left) and at 13:28 UTC+2 on 7 (right) April 2017 in Didcot.

lines below 300 nm can be attributed to the sensor related measurement uncertainty which is increasing to 10% or higher for wavelengths smaller than 300 nm according to the calibration by factory. Therefore only the spectral interval 300 and 400 nm will be

interpreted subsequently. On both days the highest CMF_s values representing the smallest cloud impact can be observed in the UV-B spectral part with SL307.2 being marked by the vertial red line (Fig. 48). In the UV-A spectral interval the CMF_s values decrease with increasing wavelength. The cloud influence on 6 and 7 April is visualized for both measured and estimated spectral UV erythemal irradiance data at the moment of maximum cloud cover (Fig. 49). SL307.2 (vertical red line Fig. 49) shows the highest radiative energy of all spectral lines in the considered UV spectral interval. The UVER peak occurring in the UV-B spectral interval results from the application of the erythema action function.

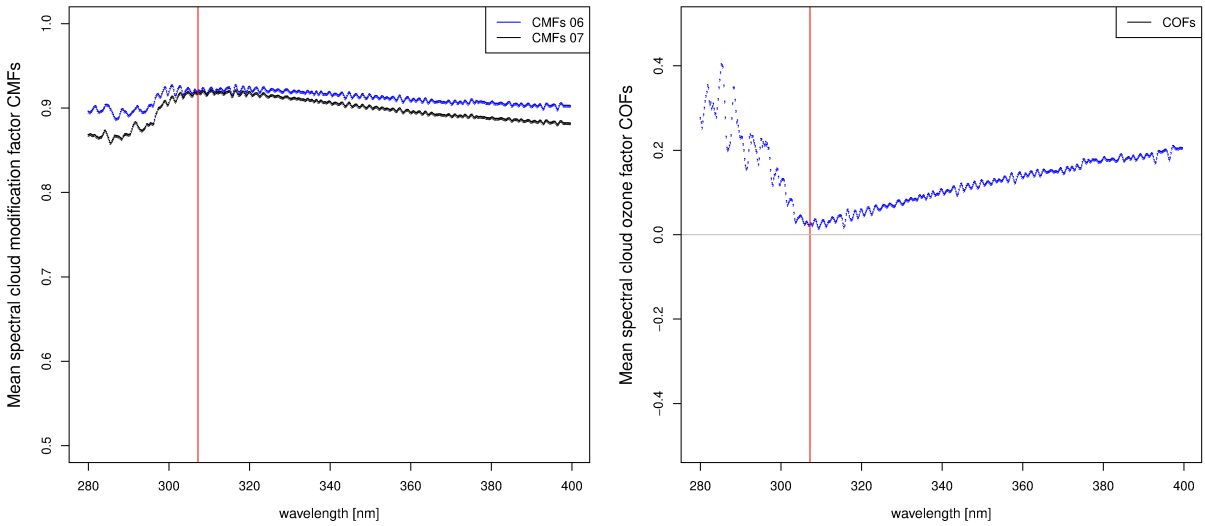

Fig. 50: *Left:* SI mean CMF_s (left) on 6 and 7 April 2017 in Didcot. *Right:* SI mean COF_s.

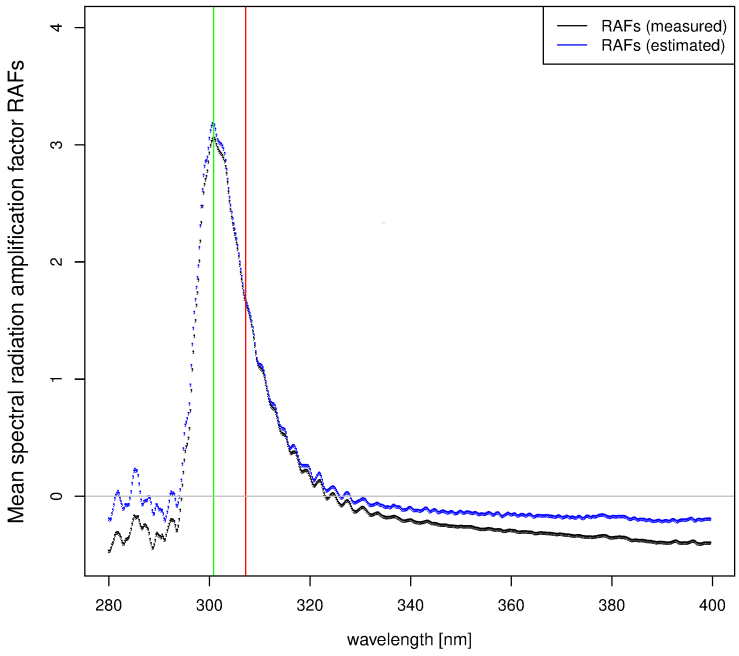

Fig. 51: Estimated and measured SI mean RAF_s.

The cloud impact on the incoming UVER is investigated by calculating and comparing the mean spectral cloud modification factor for the same time period on both days. Analogously to the previously presented dosimeter data analysis the SI time interval, stretching from 12:00 to 16:00 UTC+2 and representing the radiatively most intense period, is chosen for the spectral analysis as well. Comparing the SI mean CMF_s of both days (Fig. 50, left) leads to two important observations: Firstly, the SI mean CMF_s values between 305 and 310 nm are almost identical (0.92) on both days. Secondly, the cloud influence is stronger in the UV-A than in the UV-B spectral part on both days as indicated by generally lower SI mean CMF_s decreasing to 0.87 on 7 April. The mean spectral cloud ozone factor (COF_s) is calculated in order to determine the relative (spectral) weight of both the influence of clouds and the change in total ozone (TOC) on the amount of surface UVER on 6 and 7 April. In analogy to the derivation of the dose related COF (cf. eq. 4.33) the COF_s (Fig. 50, right) is calculated based on the mean CMF_s of both days (Fig. 50, left) and the TOC ratio as introduced in section 4.3. The COF_s has its minimum values (~ 0.01) in the spectral range between 305 and 310 nm (SL307.2 indicated by the vertical red line) and with its maximum values reaching 20% for longwave UV-A irradiances. Considering SL307.2 and assuming a vanishing logarithmic ratio of the mean CMF_s in this case, equation (4.33) reduces to

$$\frac{log\left(\frac{UV_{\lambda,m,1}}{UV_{\lambda,m,0}}\right)}{log\left(\frac{TOC_1}{TOC_0}\right)} = -RAF_{\lambda,m} = -RAF_{\lambda} = \frac{log\left(\frac{UV_{\lambda,e,1}}{UV_{\lambda,e,0}}\right)}{log\left(\frac{TOC_1}{TOC_0}\right)} \tag{4.34}$$

with the subscript λ indicating $UV_{\lambda,m,(0,1)}$ ($UV_{\lambda,e,(0,1)}$) to be the measured (estimated) SI SL307.2 dose on 6 (index 0) and 7 (index 1) April, respectively. Entering the SL307.2 do-

Tab. 22: SL307.2 doses and RAF

12:00 - 16:00 UTC+2 (SI)		
	UV_m [$Jm^{-2}nm^{-1}$]	UV_e [$Jm^{-2}nm^{-1}$]
6 April (index 0)	1.52545	1.65834
7 April (index 1)	1.84054	2.00639
RAF	1.6439	1.6680

ses of the case presented (Tab. 22) into equation (4.34) shows that the RAF calculated based on estimated doses almost equals the RAF calculated based on measured doses (Tab. 22) with the difference being smaller than 1.5%. The maximum mean SI RAF_s values for this event, however, are observed for SL300.8 (vertical green line, Fig. 51) amounting up to 3.05 (3.18) based on measured (estimated) doses, respectively.

Discussion

The comparison of the previously presented results based on spectral UVER data with the results derived based on dosimetric UVER data (Tab. 21) leads to the following conclusions: The increased relative cloud impact for longer wavelengths being expressed by increased COF values is found in both data sets (dosimetric and spectral). However, differences occur with respect to the COF sign being negative (-0.07) for the dosimetric

SI global UV-B dose indicating a weakened relative cloud impact on the second day. On the contrary, the spectral COF calculated based on the respective SI UVER doses is still slightly positive within the UV-B range (Fig. 50, right) indicating a slightly stronger cloud induced UVER dose attenuation on the second day. One reason for these differences may be the broader data base of measured dosimetric clear sky data from the morning and afternoon hours of both days which was used to calculate the clear sky estimate data set. Due to organisational reasons the respective dosimeters were fixed to the measurement station throughout the measurement period. The spectroradiometer, however, had to be removed and remounted to the tripod on each measurement day to avoid condensation and subsequently a potential sensor damage during the night period. Another reason causing the previously mentioned differences could be the different measurement frequency with the dosimetric data being collected secondly, whereas the spectral data is measured once per minute. As the cloud cover is highly variable on short time scales (seconds) it may not be correctly represented in respective spectral doses.

The investigation of spectral UVER data gathered during the low-ozone event on 6 and 7 April 2017 in Didcot, England, was performed by calculating the SI mean spectral cloud ozone factor (COF_s). Based on this analysis almost identical SI SL307.2 dose ratios were calculated for both measured and estimated UVER doses, respectively. From this result it is concluded that the impact of this low-ozone event on surface UVER can be described by two almost identical radiation amplification factors if calculated based on either measured or estimated SL307.2 UVER data. This behaviour is confirmed by evaluating equation (4.34) assuming a vanishing COF for SL307.2. Thus, it is suggested to characterize the impact of ozone mini-holes on surface UVER based on SL307.2 data in general. For low-ozone events with similar cloud meteorological conditions throughout the event, thus showing similar CMF values, this suggestion would mean that only measured SL307.2 data were necessary to derive the corresponding radiation amlification factor for clear conditions. This would be a significant simplification as no clear sky estimate UVER data set were necessary. As introduced earlier, ozone mini-holes occur in conjunction with synoptic scale anticyclones generally leading to rather similar meteorological conditions for a specific location over one or two days. This also supports the previously made suggestion regarding the simplified method to derive the event's clear sky radiation amplification factor. However, despite similar large scale metereorological conditions during such an event, mesoscale meteorological phenomena, like fog events or boundary layer clouds for example, have to be kept in mind as they are hardly to predict and as they may significantly modify the incoming solar UVER. For this, further case studies are necessary to evaluate the applicability of the presented method which could potentially provide a procedure to characterize the purely ozone content related impact of a low-ozone event on surface UVER based on cloud influenced measured SL307.2 data.

5 Summary and outlook

Combined dosimetric and meteorological measurements were performed during the GENESIS-UV campaigns 2016 and 2017 with each of these measurements lasting for one or two days. The dosimetric data was gathered both by probands during their respective work outdoors and by horizontally oriented dosimeters which were fixed to the mobile weather station in use. The goal of these measurements was to collect a data base in order to elaborate and determine the actual UVER exposure of outdoor workers. The stationary dosimeter measurements were conducted synchronously to provide the actual maximum possible UVER dose which could have been received by outdoor workers during the respective time interval. The highest absolute UVER doses gathered during the working period amount to 7.76 SED for a scrapyard worker, to 7.94 SED for a track worker and to 7.29 SED for a fruiter. The corresponding fractions of the maximum possible UVER doses amount to 15.8%, 23.4% and 38.6%, respectively, indicating significantly different actual exposures for different occupational groups. In order to better protect outdoor workers further investigations may be performed based on the created data base to estimate their UVER exposure during specific job tasks.

Based on the stationary dosimeter measurements the UV index is calculated and compared to the corresponding DWD UVI forecast. In 56% of the cases measured and forecasted UVI agree within the accuracy of the prediction method ($\pm$ 1 UVI). The results also indicate a general underestimation of the actual measured UVI. As expected, the largest differences between measured and forecasted UVI occurred for measurement days characterized by strong (7-8 okta) and in one case by multi-layer cloud coverage. In these cases especially short time periods (up to one hour) with reduced cloud coverage caused significantly higher UVER exposure as originally predicted. Another reason causing a significant difference between measurend and predicted UVI values is a change of the meteorological conditions. In one case a frontal system dissolved earlier than predicted as did the accompanied cloud cover which subsequently lead to higher UVER at the surface. In order to improve the UVI as a simple tool to inform the public about the expected UV hazard it is suggested to provide both the UVI for cloudy and clear conditions at the same time for spreads larger than 1 UVI.

The cloud influence on personal exposure to solar UVER is estimated based on horizontally collected diffuse and global UVER dosimeter data. The corresponding measurements took place on 16 and 17 August 2016 in Jena. A clear sky UVER exposure data set was generated by a non-linear regression performed based on cloud free measured dosimeter data. Based on both data sets SimUVEx model simulations were performed in order to calculate the individual exposure to solar UVER. As a result the UVER exposure of different anatomical zones was compared. The results are also visualized for a human body posture for global and diffuse UVER (UV-A, UV-B) data, separately. By comparing the results based on measured and estimated data sets the strongest relative global UVER dose increase (19.2%) is observed for the trunk front and the weakest occurs for the skull anatomical zone (12.7%), respectively. The relative diffuse UVER dose increase amounts to 3.6% for all anatomical zones being generally much smaller than the respective relative global dose increase. The comparison of relative diffuse UV-A and UV-B dose increases results in a 2.4-2.5% increase for the UV-A and a 3.9% increase for the UV-B spectral part, respectively. The cloud influence derived from horizontally collected data and the

simulation results of the anatomical zone with the highest relative dose changes are also compared. From these results it is concluded that the horizontally collected data provides a conservative estimation of the cloud impact on personal UVER exposure as the relative differences are larger for all spectral intervals and fractions (global, diffuse). By comparing the diffuse dose fraction of UV-A (UV-B) for clear and cloudy conditions the following conclusions can be drawn: The diffuse dose fraction significantly varies depending on the body location being generally larger in the UV-A than in the UV-B spectral part and the relative diffuse doses of both spectral parts are 5-8% larger for cloudy conditions. By comparing the absolute UV-A and UV-B doses of each anatomical zone, the absolute UV-B doses are generally found to be 4-5 times larger compared to the respective UV-A doses. Further investigations are recommended to elaborate the effectiveness of UVER protection measures like sun glasses, shirts, hats etc. in reducing or compensating UVER dose increases being related to reduced cloudiness or stratospheric ozone amounts.

On 7 April 2017 a low-ozone event occurred over southern England, Wales and Ireland. Ozone measurements from Reading indicate a ozone reduction from 315 *DU* on 6 April to 281 *DU* on 7 April. Both meteorological and dosimetric measurements were performed on 6 and 7 April on the roof of the PHE (Public Health England) building on Harwell Campus (Didcot). In conjunction with the low-ozone event a strong anticyclone characterized the synoptic situation over the British Isles leading to large-scale subsidence and a strong temperature inversion at the top of a well-mixed planetary boundary layer (PBL). Additional lee effects south of the english and welsh mountain ridges together with the large scale setting caused very similar meteorological conditions over the Didcot area on both days. The early morning hours, the later afternoon, the evening as well as the nighttime were characterized by clear conditions. During noon shallow stratocumulus clouds (SSC) formed as a result of radiatively forced turbulent mixing within the PBL. The goal of the two day measurements is to investigate the ozone mini-hole effect and the SSC influence both independently affecting the diffuse and global surface UVER dose amounts. For this, estimated and measured UVER doses were used to calculate the corresponding CMF values. As innovation the RAF is splitted to quantify the SSC influence in comparison to the change in total ozone during a low-ozone event. The UVER dose estimates were calculated for the two time intervals 0630-1530 LT (LI) and 1100-1500 LT (SI), i.e. the cloudy time period of the two days. The results show clear differences between the behaviour and impact of the low-ozone event and the meteorological influence in form of SSC coverage. During the LI interval the SSC coverage caused total diffuse (global) UVER dose reductions of 0.77 (2.33) SED on 6 April, and 0.74 (2.81) SED on 7 April. In contrast to this the low-ozone event on 7 April caused diffuse (global) UVER dose increases of 2.67 (4.32) SED. Thus on 7 April, the SSC coverage compensated almost 65% of the low-ozone induced total global UVER dose increase highlighting the strong cloud influence on the daily UVER doses. The newly introduced splitting of the RAF into two compensating factors (COF, RAF_m) results in two major conclusions regarding the low-ozone event's influence: First the SSC influence is more pronounced acting on the diffuse than on the global UV-B part as indicated by a COF value with a magnitude being twice as large as for the global UV-B interval. Nevertheless, the relatively high RAF_m values indicate the logarithmic dose ratio being the dominant term for the UV-B spectral range. Secondly, compared to the diffuse UV-A part the SSC influence is enhanced for the global UV-A part as indicated by a positive COF. Spectral UVER data was also gathered during the previously mentioned low-ozone event. Analogously to the

dosimetric data sets the collected spectral data sets were analyzed for the SI time period focusing on both the cloud and the ozone mini-hole impact, respectively. The results show almost vanishing mean SI COF_s values for the spectral range between 305 and 310 nm. Regarding the 300 - 400 nm spectral interval the mean SI COF_s amounts up to 20%. The highest spectral intensity is observed for 307.2 nm with this wavelength also being characterized by a mean SI COF close to zero despite cloudy conditions. The maximum mean SI RAF_s is observed for SL300.8 amounting to 3.05 (3.18) based on measured (estimated) doses. Generally a very strong RAF_s wavelength dependency for the total UV spectrum is observed. More low-ozone events should be analyzed in order to evaluate the previously presented results regarding the special characteristics of SL307.2, SL300.8 and the SI mean COF_s.

Appendix

Meteorological measurements - preparations and procedure:

In general, the application of the mobile station during the GENESIS-UV campaigns 2016 and 2017 required several recurrent working steps. To get an overview of how the meteorological measurements were performed and which preparations were necessary, essential steps being relevant for each measurement are listed chronologically in the next paragraph:

One or two days before the departure:

- Get into contact with a representative of the respective assurance provider and with a representative of the executive company on site including the appointment of the time schedule and a meeting on the day before the meteorological measurements.
- Checking the general weather situation to ensure at least dry and at best sunny conditions for the meteorological measurements.
- Preparation of the equipment including the configuration and charging of all necessary dosimeters, charging of the other accumulators, the creation of a new setup file, hotel booking, reservation of a staff car and preparing the protocol templates.
- Packing and stowing the equipment into the staff car as well as preparing the route.

Arrival day at the site:

- Brief weather check and travel to the meeting point.
- Get into contact with the responsible persons and probands to clarify the measurement time schedule and to handle the mandatory paperwork in advance.
- Visit at the envisaged measurement site to get to know the area and to finally check its adequacy. Obtain the approval to rig up the mobile station.

Measurement day(s):

- Rigging up the meteorological station in the early morning with the general target to start the measurements prior to 9 am (local time).
- Monitoring of the measurements: This includes protocolling of incidents during the measurements (as far as possible), to change the action camera accumulators every 1 to 1.5 hours, to check the measurements of the spectroradiometer and to take photographs of the measurement unit for documentation.
- Subjective observation and protocolling of the meteorological conditions with focus on the cloud cover.
- Disassembling of the weather station after having collected data during noon and the early afternoon to cover the radiatively most intense diurnal time interval.

Return trip to the IFA:

- The return to Sankt Augustin was either directly after having disassembled the station or, if the distance was too long, in the morning of the next day.
- An IFA staff car was used to transport the whole equipment and to travel to the measurement sites.

Back at the IFA:

- The equipment was stored away after having secured the logged data of all sensors and after having sent all dosimeter data via tablet to the IFA server.
- All accumulators were recharged for the next event.
- The action camera images were condensed to a short video sequence and the handwritten protocols were rewritten into a pdf-document.
- After having evaluated some basic data, a report was drafted for of each measurement event.

Sensor comparison at Münster/Osnabrück International Airport:

The first application of the mobile meteorological station took place on 6 June 2016 at the official DWD weather station at Münster/Osnabrück International Airport (Figs. 52 and 53). The measurement was set up in order to check the functionality and accuracy of the (new) meteorological station by comparing each meteorological parameter to the respective counterpart being collected by the official DWD station. On 6 June the synoptic situation in Central Europe is characterized by two surface high pressure systems covering the North Sea and the Baltic Sea. These pressure patterns govern a weak southeasterly surface wind regime over Germany (Fig. 54). High pseudopotential temperature values over Southern and Central Germany indicate a relatively warm and humid airmass compared to the airmass within the two high pressure systems. The corresponding airmass boundary extends from Aachen to Hanover and further southeastward to Dresden (Fig. 54). Thus the Münster/Osnabrück region was influenced by the cooler and drier maritime airmass over the North Sea with clear conditions at the site after the morning fog had disappeared. The DWD UV hazard prognosis chart (Fig. 55) shows high to very high danger levels for entire Germany, especially for the eastern and southeastern regions.

Fig. 52: Aerial picture of the DWD aerial weather station at Münster/Osnabrück airport and position of the mobile station (arrow) (www.bing.com/maps)

Fig. 53: Mobile weather station and official DWD station (12:45 pm)

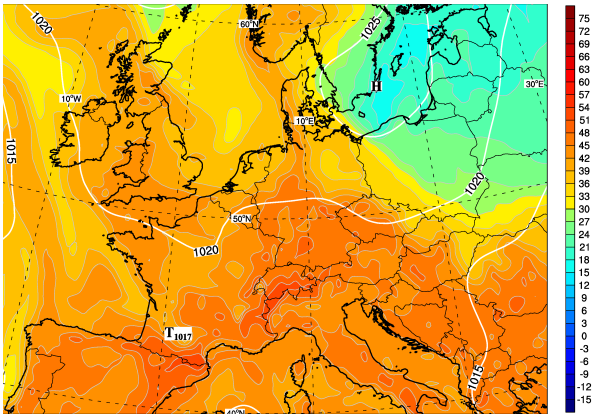

Fig. 54: 850 hPa pseudopotential temperature [°C], surface pressure [hPa], 6 June 1200 UTC (NCEP-GFS model analysis)

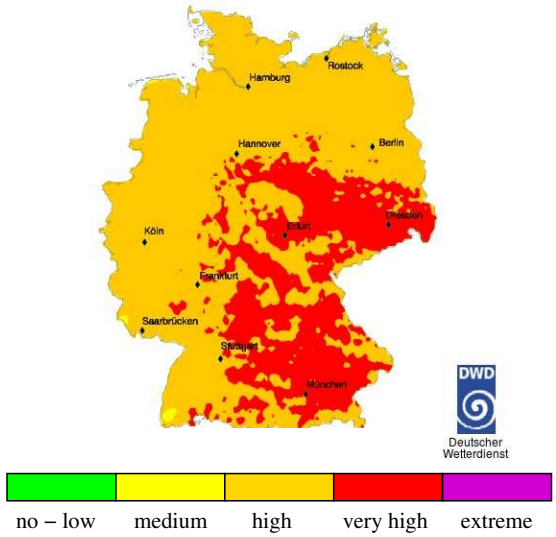

Fig. 55: UV hazard prognosis for 6 June 2016 (www.dwd.de)

The results of comparing each meteorological parameter show the proper functionality of each mobile weather station sensor. The comparison of the air pressure data shows the synchronous behaviour of the DWD and MAWS sensor (Fig. 56) with a mean absolute difference value of 0.4 hPa (Fig. 57) resulting from the 4 m height difference between the two pressure sensors. The comparison of the 10 min mean temperature values (Fig. 58)

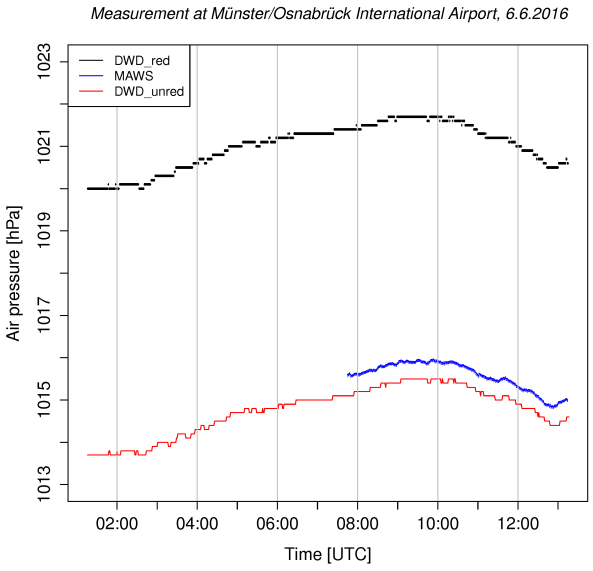

Fig. 56: Surface pressure of DWD station and MAWS.

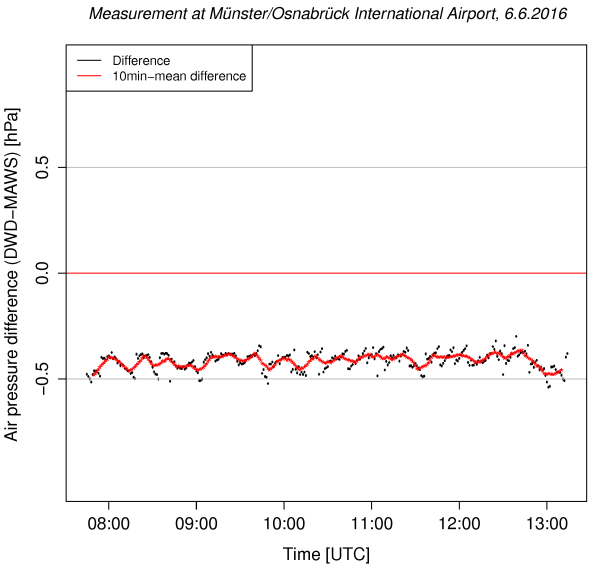

Fig. 57: Difference of surface pressure values of DWD and MAWS.

shows good agreement despite some time intervals with relatively high variability (e.g. around 10 and 12 UTC). The mean difference of both data sets amounts to 0.6 K (Fig. 59). A reason for the temporarily high variability is the lack of ventilation of the MAWS sensor. To reduce this variability for future measurements, an USB ventilator was attached in front of the MAWS temperature sensor providing a constant current of surrounding air.

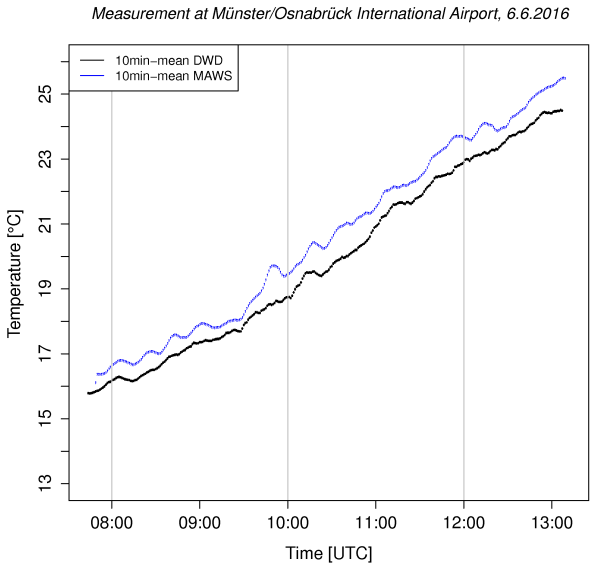

Fig. 58: 10min mean temperature values of DWD and MAWS.

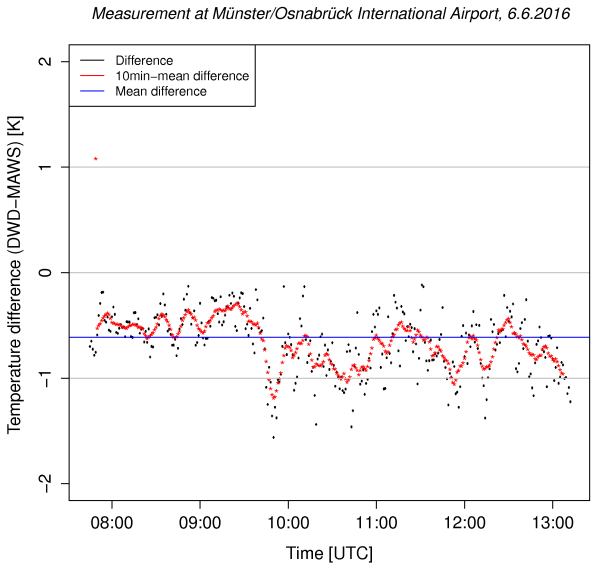

Fig. 59: Difference of the 10min mean temperature values of DWD and MAWS.

Measurements with the spectroradiometer are performed every minute by taking three scans. The mean irradiance value of three scans is calculated by the instrument for each wavelength between 200 and 430 *nm* (Fig. 60). The spectral data is weighted by applying the official erythemal action spectrum (black curve in Figs. 60 and 61) to calculate the UV erythemal radiation (UVER, red curve in Figs. 60 and 61). The relatively high amount of UVER between 300 and 315 *nm* clearly highlights the effectiveness of UV-B irradiance in causing erythema. The large UVER values for wavelengths lower than 280 *nm* are of artificial nature resulting from scattering effects and should be neglected.

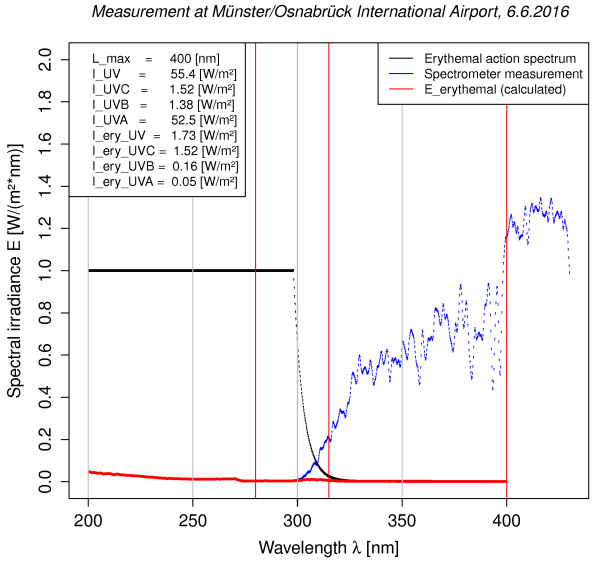

Fig. 60: Spectralradiometer measurement (11:13 UTC).

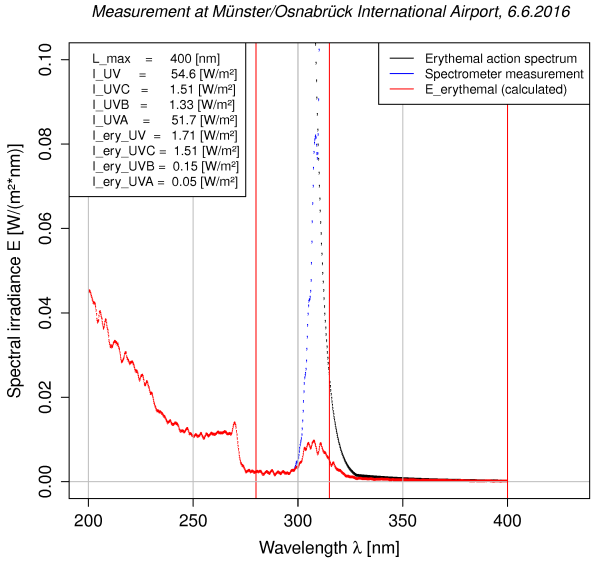

Fig. 61: Spectralradiometer measurement (11:13 UTC, y-axis scale changed).

On 14 November 2016 the final meteorological measurement after the GENESIS campaign 2016 took place at the official DWD station of Münster/Osnabrück International airport. The measurement was performed to directly compare each meteorological parameter of the mobile meteorological station with the respective parameter collected by the official DWD station to get an update of the unit's accuracy and functionality after the numerous meteorological measurements of the 2016 GENESIS campaign (Tab. 2). The mobile unit was rigged up near the official instruments of the DWD station being located at but not within the southern enclosure of the airport's security zone (Figs. 62, 63). The same DWD station was already visited for the previous tests with the mobile weather station before its application during the GENESIS campaign.

Fig. 62: Aerial picture of the DWD station and the location of the MAWS station (arrow) (www.bing.com/maps)

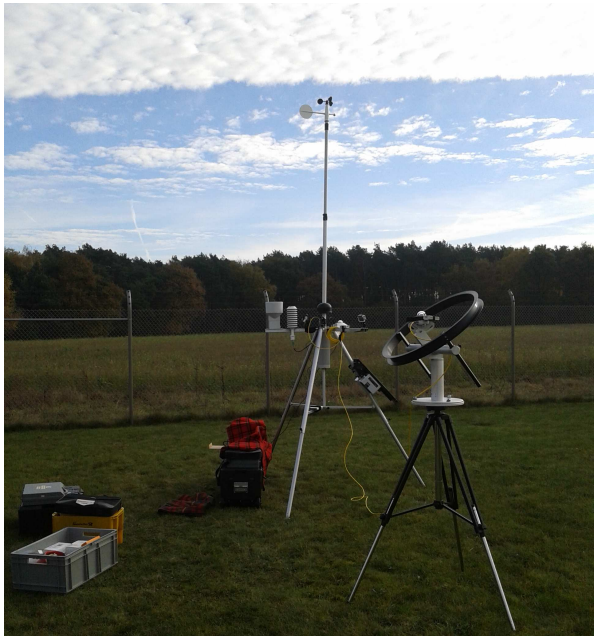

Fig. 63: Mobile weather station at the airport Münster/Osnabrück (14.11.2016, 10:42 am)

On 14 November the synoptic situation over Central Europe is characterized by a strong surface high pressure system centered over southeastern Poland (Fig. 64). This anticyclone governs the wind regime over Germany resulting in mostly weak revolving winds close to the surface. The coastal regions on the other side are already influenced by the wind regime of an intense frontal system corresponding to an approaching low pressure system from the British Isles. Relatively low pseudopotential temperature values indicate a cold and dry airmass over Central and Eastern Europe (Fig. 64). In the morning of 14 November the first indications of the approaching warm front emerged as a thin cirrus cloud band from the West. This cirrus shield was sharply separated from the forerunning clear air (Fig. 63, on top). The UV hazard prognosis chart indicates no UV danger for entire Germany (Fig. 65). These low danger levels result from the large solar zenith angle in November at noon and the cloud shield due to the approaching warm front as just mentioned. Despite the low UV endangerment the measurement results are important concerning the functionality check of the mobile unit. In the following paragraph the most important comparison results are briefly discussed.

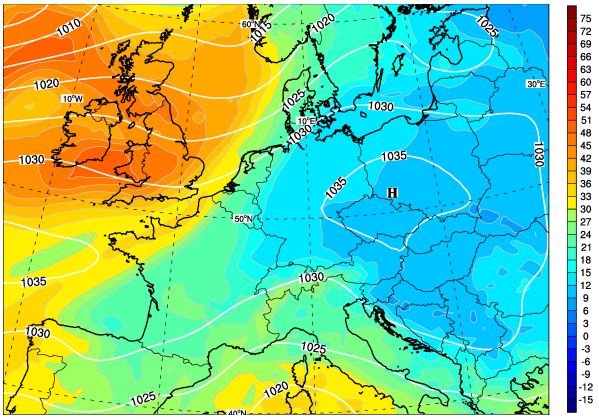

Fig. 64: 850 hPa pseudopotential temperature [°C], surface pressure [hPa], 14 November 2016, 12 UTC (NCEP-GFS model analysis)

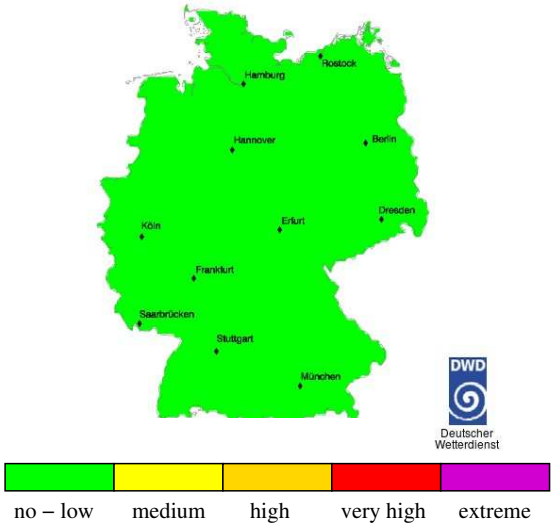

Fig. 65: UV hazard prognosis on 14.11.2016 (www.dwd.de)

The comparison of air pressure data collected by the official DWD station and MAWS shows a synchronous behaviour during the time interval covered by both sensors (Fig. 66). The 10 *min* mean difference of both time series amounts to 0.45 *hPa* (Fig. 67) as a result of the height difference (4 *m*) between both sensors. Comparing the results of the temper-

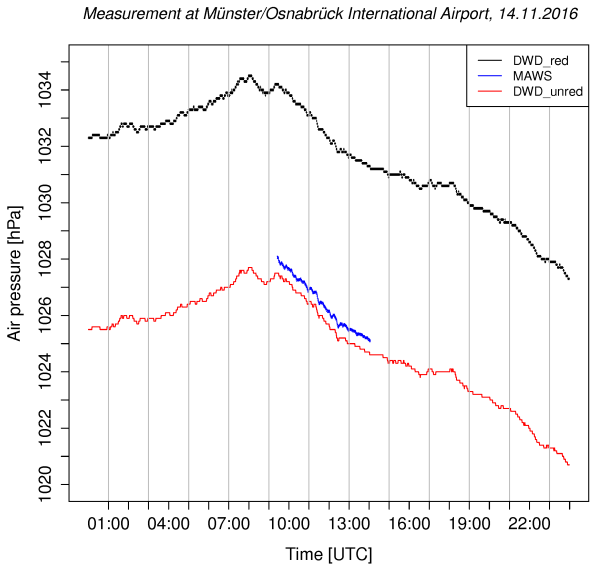

Fig. 66: Surface pressure of DWD station and MAWS.

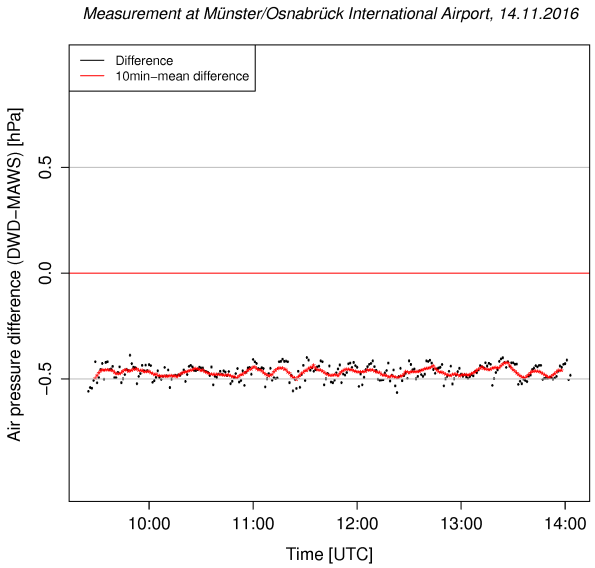

Fig. 67: Difference of surface pressure values of DWD and MAWS.

ature measurement of both stations yields a very good agreement with the MAWS temperature values being slightly higher than the corresponding DWD data (Fig. 68). The 10 *min* mean difference of both time series amounts to 0.35 *K* (Fig. 69). The MAWS temperature sensor shows much higher temperature values just for the first ten minutes after having started the data logging. The reason for this behaviour is the relatively high sensor temperature directly after its unpacking.

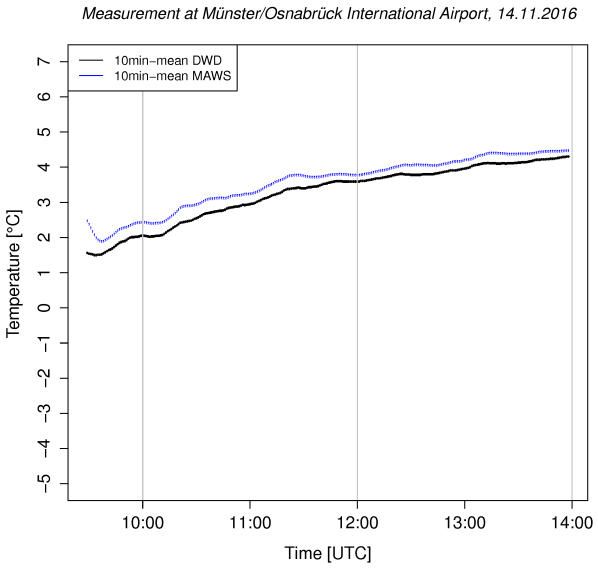

Fig. 68: 10min mean temperature values of DWD and MAWS.

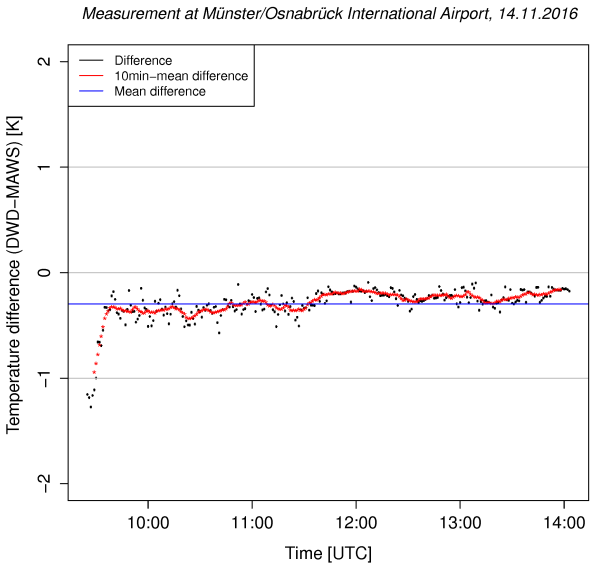

Fig. 69: Difference of the 10min mean temperature values of DWD and MAWS.

The mean difference values for each sensor for both comparing measurements framing the 2016 meteorological measurements are listed subsequently:

Tab. 23: Mean differences* of the MAWS sensors after two comparing measurements

sensor	accuracy	mean diff. 6.6.16	mean diff 14.11.16
anemometer	$\pm$ 0.3 ms^{-1} ($\mathbf{v} \leq 10\ ms^{-1}$) $< 2\%$ ($\mathbf{v} > 10\ ms^{-1}$)	0.9 ms^{-1}	1.2 ms^{-1}
potentiometer	$\pm$ 3%	10°	12°
pyranometer	diffuse irradiance 10 Wm^{-2} (direction)	-**	8%
pyranometer	global irradiance 10 Wm^{-2} (direction)	5%	8%
HMP155 (RH)	1% (0 - 90% RH) 1.7% (90 - 100% RH)	1% RH	4% RH
HMP155 (T)	-80 bis +20°C $\pm$(0.226 - 0.0028 $\times$ temperature)°C	-0.4 K	-0.35 K
HMP155 (T)	+20 bis +60°C $\pm$(0.055 + 0.0057 $\times$ temperature)°C	-0.8 K	-***
BAROCAP®	$\pm$ 3% between -40 and +60°C	-0.4 hPa	-0.45 hPa

* The mean difference is calculated as (DWD-MAWS).
** Could not be determined, due to falsely programmed setup.
*** air temperature below 20°C during the measurements.

On 1.6.2017, a measurement with the mobile meteorological station (MAWS) was performed at the official DWD weather station at Münster/Osnabrück International Airport

(Fig. 70). This event was set up in order to check the functionality of the mobile meteorological unit before the GENESIS-UV campaign 2017 by comparing both synchronously collected meteorological data sets. The DWD station in Münster was again chosen as reference station because of its relatively easy accessability not being located within the airport's security zone and because both previously performed "comparing" measurements already happened there. The mobile meteorological station was rigged up close to the DWD sensors within the official "weather garden" zone bounded by a fence (Figs. 70, 71).

Fig. 70: Aerial picture of the Münster/Osnabrück airport with the aerial weather station (black rectangle) (www.bing.com/maps)

Fig. 71: Aerial picture of the DWD weather station at the airport with the location of the mobile meteorological unit (arrow) (www.bing.com/maps)

The meteorological instruments were listed in section 3.2 including the shadow ring to collect the diffuse part of the solar irradiance (Fig. 73) as well as the sensors additionally attached to the mobile unit (Fig. 72, 74).

Fig. 72: Mobile station (MAWS) at DWD site (1.6.2017, 9:55 MESZ)

Fig. 73: Shadow ring with pyranometer and dosimeter (1.6.2017, 9:54 MESZ)

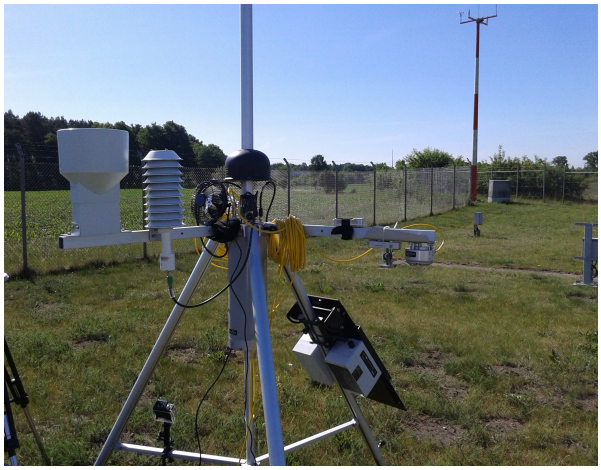

Fig. 74: Meteorological sensors of MAWS (1.6.2017, 9:54 MESZ)

On 1.6.2017 the synoptic situation over Central Europe is characterized by a shallow ridge with its horizontal axis being located in north-south direction over the North Sea and the corresponding surface high pressure system over the southern parts of the North Sea, the Netherlands and Lower Saxony (Fig. 75). The anticyclonic wind regime within the high pressure system as well as the general northwesterly flow over the South of Scandinavia are responsible for the advection of cooler air of maritime origin to the northern parts of Germany and thus to the Münster/Osnabrück area as indicated by the relatively low 850 hPa pseudopotential temperature values (Fig. 76). An airmass boundary extending from Aachen to Prague separates the cooler air in the northern parts of Germany from the warmer and more humid air over Southern Germany, France and the Balkan region indicated by the much higher pseudopotential temperature values in these regions. Due to the anticyclonic influence with largescale subsidence in the Münster/Osnabrück region, dry and sunny conditions had to be expected except for some very high thin cirrus clouds.

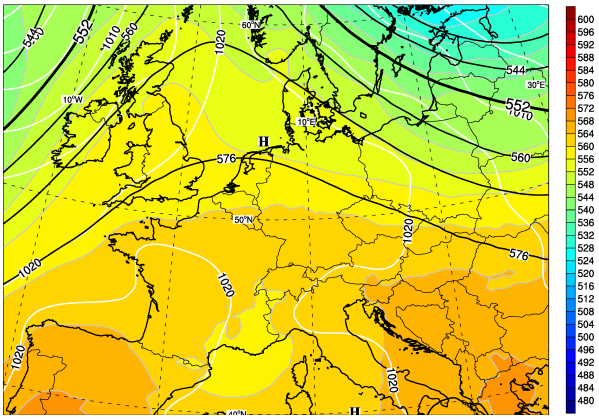

Fig. 75: 500 hPa geopotential [gpdam], surface pressure [hPa], relative topography 500-1000 [gpdam], 1 June 2017, 12 UTC (NCEP-GFS model analysis)

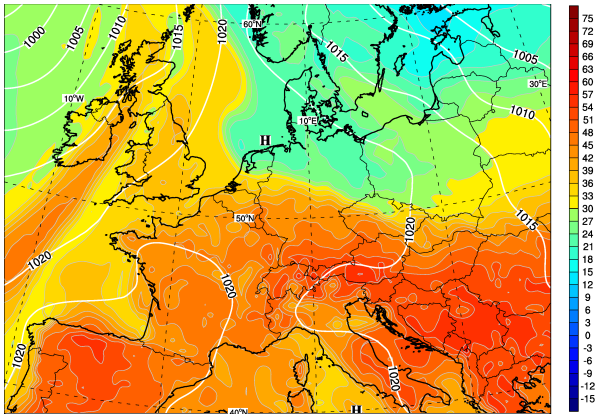

Fig. 76: 850 hPa pseudopotential temperature [°C], surface pressure [hPa], 1 June 2017, 12 UTC (NCEP-GFS model analysis)

The prognosis chart for the daily maximum UV index shows values reaching up to 7 over Central Europe (Fig. 77). These UV index values indicate high UV danger throughout

the measurement period resulting from the almost clear conditions as mentioned above. The reason for high UV danger levels especially during noon results from relatively low solar zenith angles during noon close to its annual maximum on 21.6.2017.

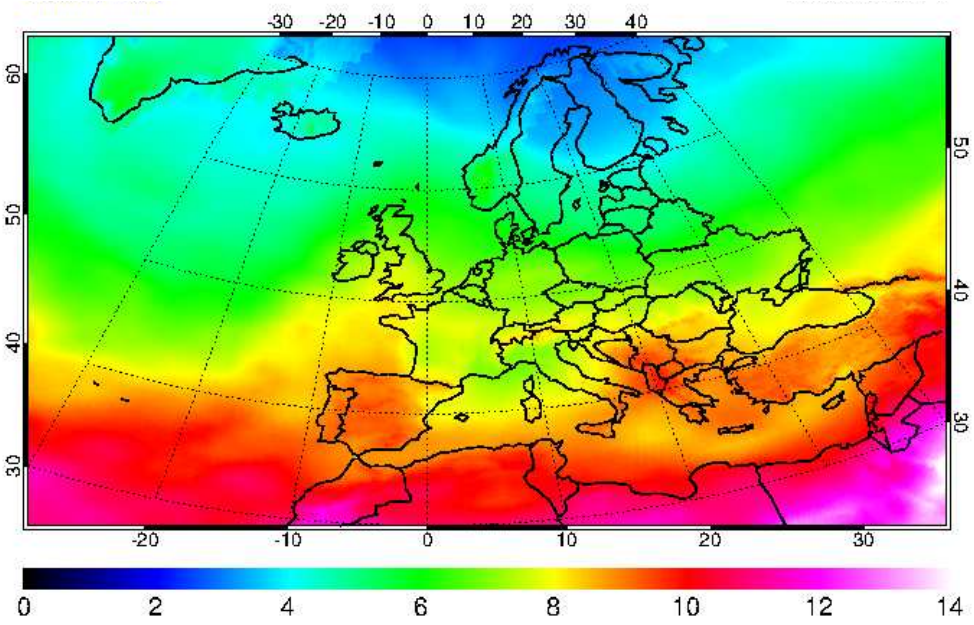

Fig. 77: UV index chart for 1.6.2017 (www.temis.nl)

In the following the comparison results for each meteorological parameter mentioned above will be presented except for the irradiance values, which could not be provided by DWD due to a sensor failure having occurred just in the early morning of the measurement day. The comparison of the relative humidity values of DWD and MAWS (Fig. 78) as well as its 10 *min* mean values (Fig. 79) shows a very good agreement for the respective time

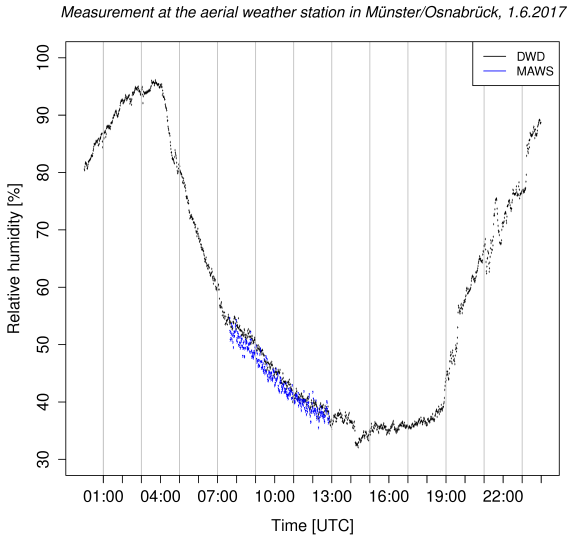

Fig. 78: Relative humidity measurements of DWD and MAWS (1.6.2017)

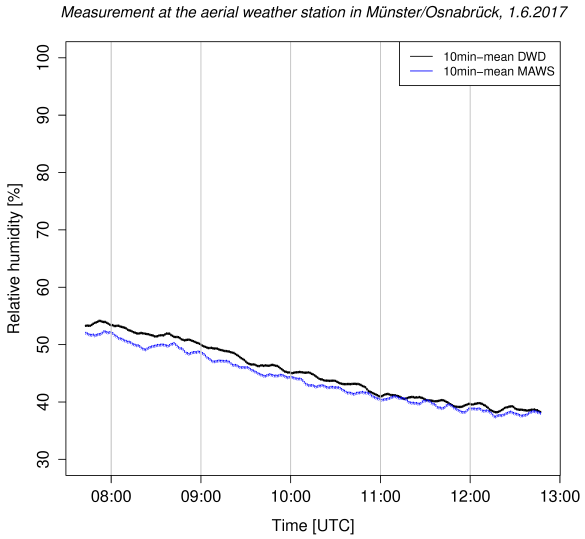

Fig. 79: 10min-mean relative humidity values of DWD and MAWS (1.6.2017)

interval (8 - 13 UTC) resulting in a mean difference of 1.7% RH for the comparison interval (Fig. 80). Thus the MAWS sensor collecting relative humidity (HMP155) is expected

to gather data in a reasonably manner with an accuracy similar to the one of the first check on 6.6.2016 (Tab. 23). Comparing DWD and MAWS temperature values (Fig. 81)

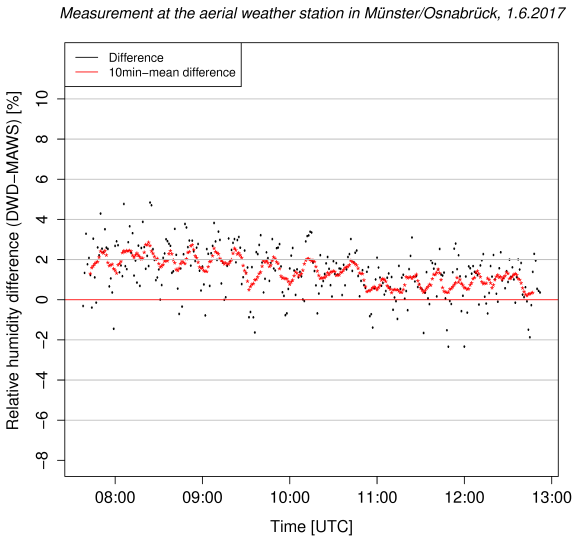

Fig. 80: Difference and 10min-mean difference of DWD and MAWS relative humidity values (1.6.2017)

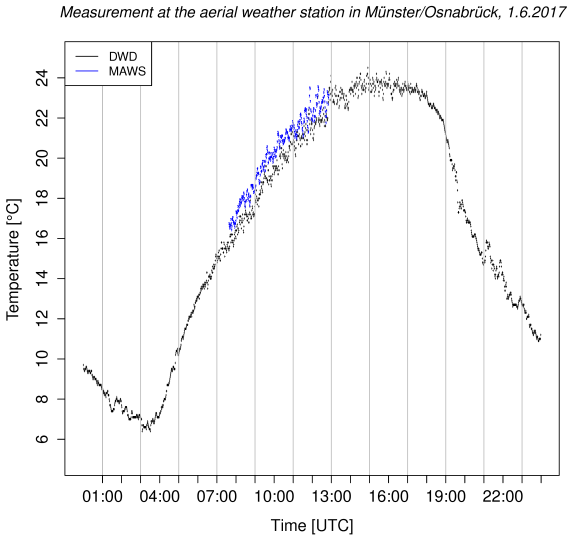

Fig. 81: Temperature measurements of DWD and MAWS (1.6.2017)

and its 10 *min* mean values (Fig. 82) also shows a very good agreement resulting in a mean difference of -0.8 K indicating a little higher temperatures for the MAWS sensor (Fig. 83). This behaviour of the temperature sensor (HMP155) and the mean difference amount is consistent with both functionality test measurements performed on 6.6.2016 and 14.11.2016, respectively.

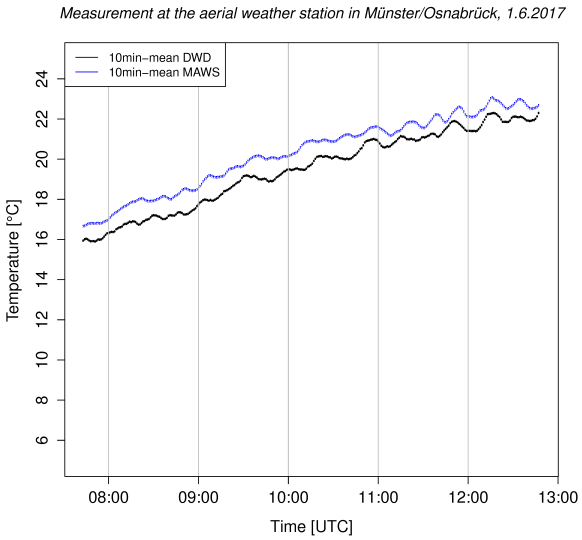

Fig. 82: 10min-mean temperature values of DWD and MAWS (1.6.2017)

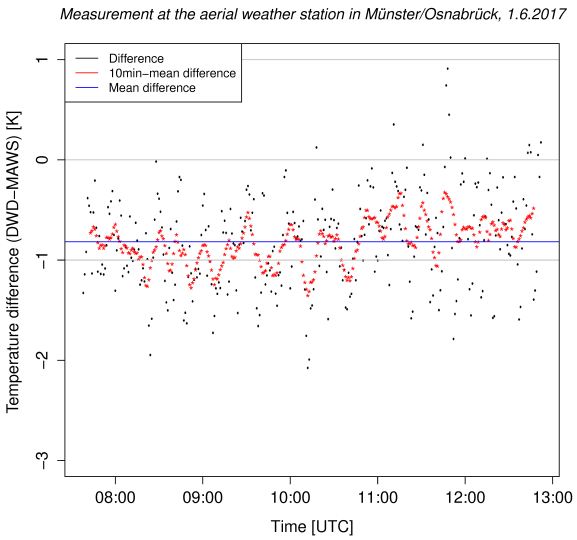

Fig. 83: Difference and 10min-mean difference of DWD and MAWS temperatures (1.6.2017)

The comparison of DWD and MAWS unreduced air pressure measurements (Fig. 84) shows a synchronous behaviour of both data sets with an overall mean difference of -0.44 hPa (Fig. 85) resulting from the sensor's height difference being mounted either in the first floor of the DWD station building or 1 m above ground (MAWS sensor).

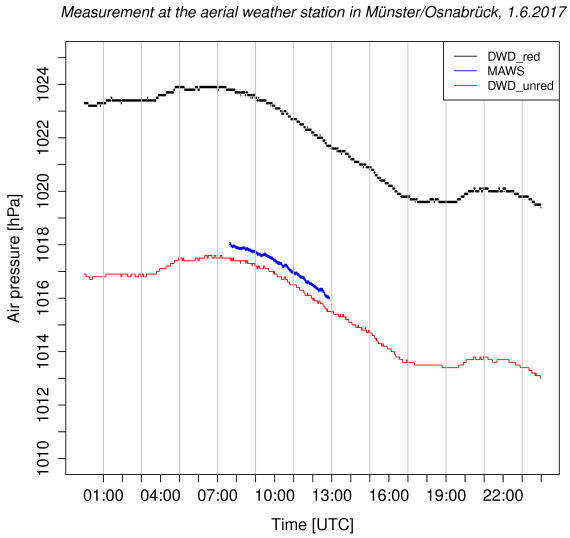

Fig. 84: Air pressure values of DWD and MAWS (1.6.2017)

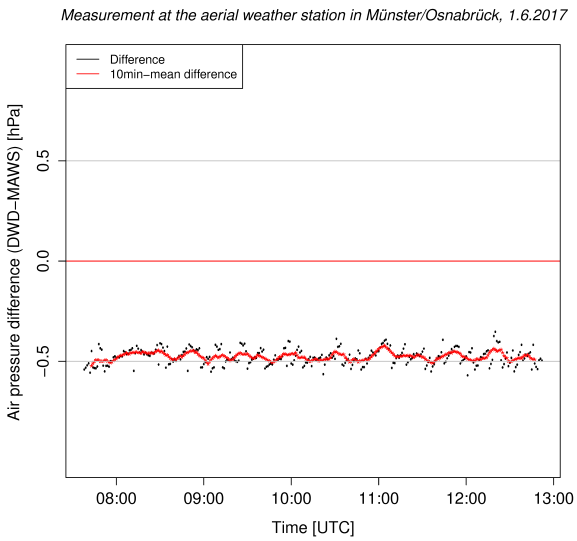

Fig. 85: Difference and 10min-mean difference of DWD and MAWS air pressure values (1.6.2017)

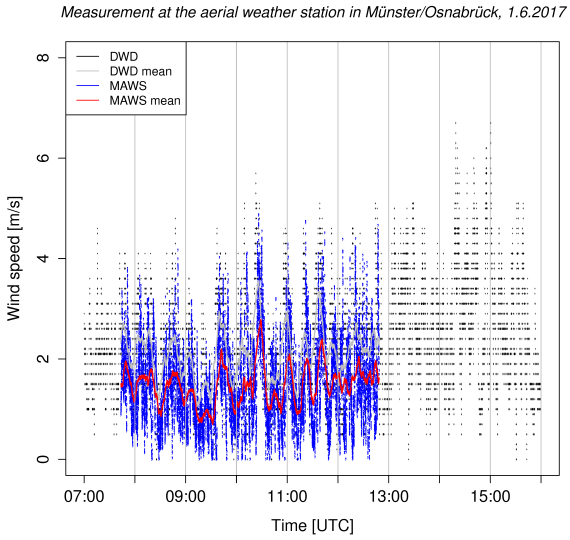

Fig. 86: Wind speed measurements of DWD and MAWS (1.6.2017)

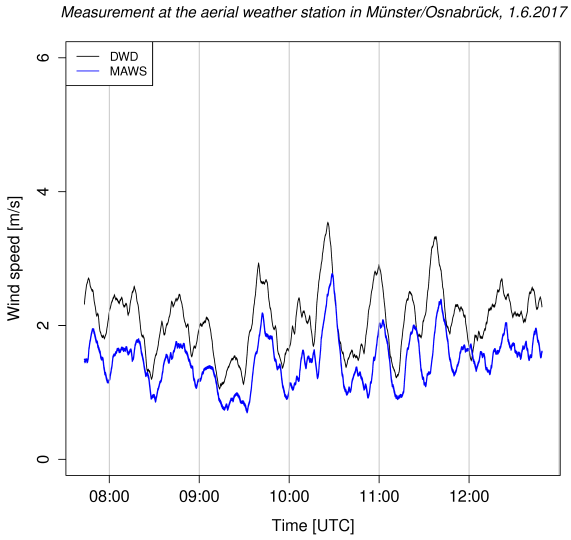

Fig. 87: 10min-mean of DWD and MAWS wind speed data (1.6.2017)

Comparing the wind speed data of DWD and MAWS and its 10min-mean values (Figs. 86 and 87) shows a synchronous behaviour of both data series with an overall mean difference of 0.6 ms^{-1} (Fig. 88). The major reason for this relatively large difference, compared to the absolute wind speed values, is the 6 m height difference between the DWD sensor (10 m above ground) and the MAWS sensor being mounted on top of the 4 m wind mast.

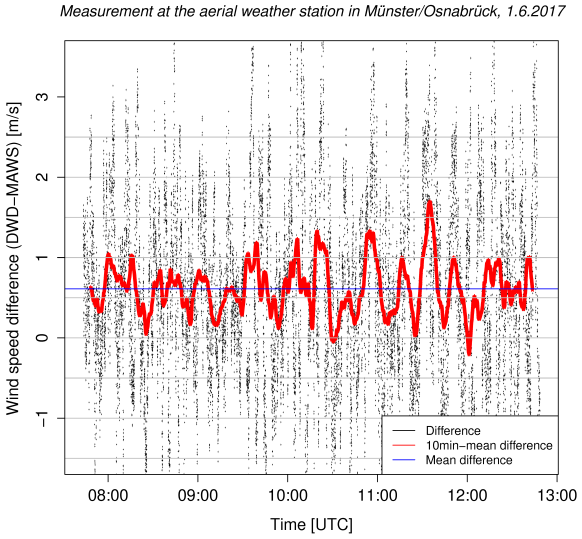

Fig. 88: Difference and 10min-mean difference of DWD and MAWS wind speed data (1.6.2017)

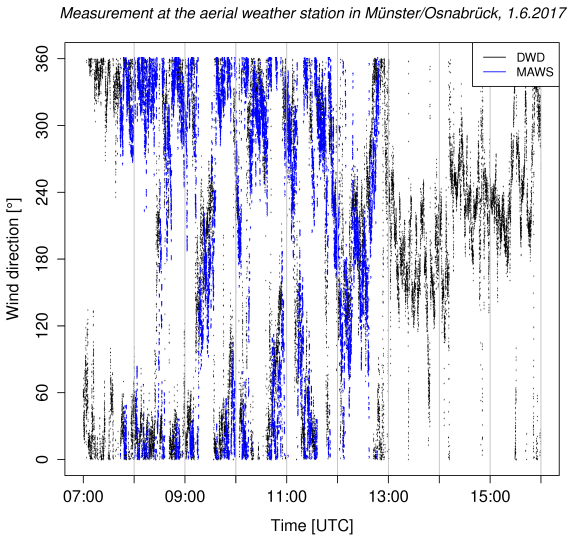

Fig. 89: Wind direction measurements of DWD and MAWS (1.6.2017)

Tab. 24: Comparison of the MAWS sensor mean differences* (MD)

sensor	accuracy	MD 6.6.16	MD 14.11.16	MD 1.6.17
Anemometer	$\pm$ 0.3 ms^{-1} ($\mathbf{v} \leq 10$ ms^{-1}) < 2 % ($\mathbf{v} > 10$ ms^{-1})	0.9 ms^{-1}	1.2 ms^{-1}	0.6 ms^{-1}
Potentiometer	$\pm$ 3%	10°	12°	-
Pyranometer	diffuse irradiance 10 Wm^{-2} (direction)	-**	8%	-****
Pyranometer	global irradiance 10 Wm^{-2} (direction)	5%	8%	-****
HMP155 (RH)	1% (0 - 90% RH) 1.7% (90 - 100% RH)	1% RH	4% RH	1.7% RH
HMP155 (T)	-80 to +20°C $\pm$(0.226 - 0.0028 x T)°C	-0.4 K	-0.35 K	-0.9 K
HMP155 (T)	+20 to +60°C $\pm$(0.055 + 0.0057 x T)°C	-0.8 K	-***	-0.6 K
BAROCAP®	$\pm$ 3% -40 to +60°C	-0.4 hPa	-0.45 hPa	-0.44 hPa

* The mean difference is calculated as (DWD-MAWS).
** Could not be determined due to wrong setup programming.
*** Air temperature below 20°C during the measurement.
**** No DWD data due to sensor failure.

In a minor fashion, the horizontal distance of about 20 m between the two sensor masts also could have contributed to the wind speed difference. With respect to the wind direction data, the comparison will be restricted to the visualization of both data series in general (Fig. 89). Despite the high variability of the wind direction during the day with-

out a ‘preferred‘ wind direction the general visualization shows a quite well fitting of both measurements indicating a correct data gathering of the MAWS wind sensor. The comparing measurement on 1.6.2017 results show that all sensors, except for the pyranometers, work quite well and reasonably collect data like during the previously performed measurements (6.6.2016, 14.11.2016). Due to a sensor failure of the DWD station's irradiance sensors (pyranometers), unfortunately no comparison between the MAWS pyranometer data and the respective DWD data can be presented here. All meteorological MAWS sensors, the respective accuracy according to the producer as well as the mean difference values resulting of all three comparing measurements are summarized in table 24.

List of symbols and abbreviations

UV	ultraviolet
GENESIS	GENeration and Extraction System for Individual expoSure
DWD	Deutscher Wetterdienst (engl: German Meteorological Service)
λ	wavelength [nm]
BKV	Berufskrankheitenverordnung
DGUV	Deutsche Gesetzliche Unfallversicherung (engl: German Social Accident Insurance)
RH	relative humidity
SSC	shallow stratocumulus clouds
COF	cloud ozone factor
RAF_m	RAF based on measurements
UV-A$_e$	estimated UV-A radiation
LI	long interval
ω	albedo
T	temperature
h	Planck constant
k_B	Boltzmann constant
r_{sun}	sun's radius
O	oxygen atom
CMAM	Canadian Middle Atmosphere Model
CO_2	carbondioxide
CMF	cloud modification factor
UV_m	measured UV radiation (cloudy)
SZA	solar zenith angle
G	global solar irradiation
BfS	Bundesamt für Strahlenschutz (engl: Federal Office for Radiation Protection)
IAEA	International Atomic Energy Agency
$I(\Theta_s)$	intensity after scattering process
BAuA	Bundesanstalt für Arbeitsschutz und Arbeitsmedizin Federal Institute for Occupational Safety and Health
LfU	Bayerisches Landesamt für Umwelt (engl: Bavarian Environmental Agency)
SED	standard erythema dose
UTC	universal time coordinated
NCEP	National Centers for Environmental Predictions
MAWS	mobile automatic weather station
$gpdam$	geopotential decameter
IARC	International Agency for Research on Cancer
WMO	World Meteorological Organization
kyr	kiloyear
θ_s	scattering angle
Γ	day angle
CIE	International Commission on Illumination
pm	post meridium
k	kilo
am	ante meridium
pdf	portable document format
$\mathbf{\Omega_s}$	photon direction (after scattering)
$d\tau_s$	differential scattering optical depth
$k_{s,\nu}$	differential scattering coefficient
k_0	wave number
ρ_0	ratio (particle circumfence, wavelength)
$d\tau_a$	differential absorption optical depth
$k_{e,\nu}$	differential extinction coefficient
N	complex index of refraction $(n + i\kappa)$
x	Mie size parameter
$\bar{P}_r$	average reflected power (radar)
$\lvert K\rvert^2$	refractive index factor
Z	radar reflectivity factor
V_T	velocity of falling droplets
P_{Mie}	Mie scattering phase function
P_{H-G}	Henyey-Greenstein scattering phase function
g	scattering asymmetry parameter
TOA	top of the atmosphere
ASTM	American Society for Testing and Materials
K	Kelvin
Figs.	figures
UVER	UV erythemal radiation
IFA	Institut für Arbeitsschutz der DGUV
AU	astronomical unit
δ	solar declination
a.s.l	above sea level
LT	local time
RAF	radiation amplification factor
UV$_e$	estimated UV radiation
UV-B$_e$	estimated UV-B radiation
Φ	latitude
α	solar height
E_λ	wavelength-specific emission
c	light speed
r_{earth}	earth's radius
O_2	oxygen molecule
O_3	ozone molecule
ν	photon frequency
CFC	chlorofluorocarbon
Fig.	figure
UV_c	clear-sky UV radiation
UVT	total solar UV irradiation
DNA	deoxyribonucleic acid
WHO	World Health Organization
RTM	radiative transfer model
UBA	Umweltbundesamt (engl: Federal Environment Agency)
UVI	UV Index
GFS	global forecast system
SimUVEx	Simulating UV Exposure
BG	Berufsgenossenschaft (Occupational Insurance Association)
t	time
Ω	solid angle
$P_{s,\nu}$	scattering phase function
τ	optical thickness
hPa	hectopascal
g	terrestrial gravity
UV-A	ultraviolet radiation (315-400 nm)
$\mathbf{\Omega}$	photon direction (prior to scattering)
UV-B	ultraviolet radiation (280-315 nm)
W	Watt
m	meter
S_0	solar constant
$d\Omega_s$	solid angle element
dl	photon path element
$\mathbf{r}$	position vector
C_s	scattering cross-section
ϕ^s	scattered energy flux
E^i	incident radiative energy
E^s	scattered radiative energy
$k_{a,\nu}$	differential absorption coefficient
j_ν	differential emission coefficient
N_ν	number of photons
dV	unit volume
C	radar constant
$N(D)$	number of drops
D	particle diameter
R	rainfall rate
ρ	air density
μm	micro meter
PVU	potential vorticity unit

OMR	ozone mixing ratio
GOMR	gradient of OMR
ppbv	parts per billion volume
ITCZ	intertropical convergence zone
SBL	stable boundary layer
CBL	convective boundary layer
CTBL	cloud topped boundary layer
PDBL	pure dynamical boundary layer
CISK	convective instability of the second kind
QBO	Quasi-Biennial oscillation
WMRG	westward-moving mixed Rossby-Gravity waves
MMW	major midwinter warming
NAO	North Atlantic oscillation
O	oxigen atom
ACV	Antarctic circumpolar vortex
cm	centimeter
M	concentration of air molecules
OH	hydroxide
NO	nitrogenoxide
NO_x	$N + NO + NO_2$
N_2O	Dinitrogenoxide
H_2O	Dihydrogenoxide
$O(^1D)$	metastable oxygen atom
X	ions as part of a chemical reaction
PSC	polar stratospheric clouds
$ClONO_2$	chlorine nitrate
HNO_3	nitric acid
EESC	equivalent effective stratospheric chlorine
UT/LS	upper troposphere lower stratosphere
AAF	anomaly amplification factor
IN	ice nuclei
TR_{clear}	total clear-sky radiation
TROPOMI	TROPOspheric Monitoring Instrument
ACGIH	American Conference of Governmental Industrial Hygienists
°C	degree(s) Celsius
J	Joule
ϵ_λ	wavelength specific emissivity
π	ratio of scope and diameter (circle)
J_{ery}	erythemal effective energy
P	phase function
SPE	solar proton event
EPP	energetic particle precipitation
k_t	clearness index
sMAPE	symmetric mean absolute percentage error
PHE	Public Health England
BDC	Brewer Dobson circulation
STE	stratosphere troposphere exchange
ABL	atmospheric boundary layer
PBL	panetary boundary layer
NWP	numerical weather prediction
MJO	Madden-Julian oscillation
Θ	potential temperature
PV	potential vorticity
TSE	troposphere stratosphere exchange
SAO	Semi-Annual osciallation
SC	sun cycle
SSW	sudden stratospheric warming
GHG	greenhouse gas
DU	Dobson Unit
UV-C	ultraviolet radiation (100-290 nm)
matm	milli-atmosphere
No.	number
CO	carbonmonoxide
HO_x	$H + OH + HO_2$
BrO_x	$Br + BrO + BrCl + HOBr$
ClO_x	$Cl + ClO + OClO + HOCl + BrCl$
$N + N_2$	atomar nitrogen, molecular nitrogen
$h\nu$	energy of a photon with frequency ν
Mt.	Mount
HCl	hydrogenchloride
STS	supercooled ternary solutions
ODS	ozone depleting substance
TOC	total ozone column
LOD	low ozone days
CCN	cloud condensation nuclei
ARI	aerosol-radiation interaction
SEA	solar elevation angle
USB	universal serial bus
V	Volt
T	Tesla
A	Ampère
SI	short interval
c	speed of light
τ	optical depth
a_λ	wavelength specific absorptivity
mPa	milli Pascal
EPP IE	EPP indirect effect
min	minute
k_{tuv}	ultraviolet clearness index
POI	points-of-interest
IST	Institute for Work and Health (Lausanne)

Bibliography

ACGIH, 1999: *Threshold Limit Values (TLV) for Chemical Substances and Physical Agents: Biological Exposure Indices (BEI). Cincinnati, Ohio: American Conference of Governmental Industrial Hygienists.* 154-158.

Adam, J. A., 2002: The mathematical physics of rainbows and glories. *Physics Reports*, **356**, 229-365.

Allaart, M., P. Valks, R. van der A, A. Piters, H. Kelder, and P. van Velthoven, 2000: Ozone mini-hole observed over Europe, influence of low stratospheric temperature on observations. *Geophys. Res. Lett.*, **27(24)**, 4089-4092.

Ambach, W., and M. Blumthaler, 1993: Biological effectiveness of solar UV radiation in humans. *Experentia*, **49**, 747-753.

Antón, M., M. L. Cancillo, A. Serrano, J. M. Vaquero, and J. A. García, 2007: Ozone mini-hole over southwestern Spain during January 2004: Influence over ultraviolet radiation. *Geophys. Res. Lett.*, **34**, L10808, doi:10.1029/2007GL029689.

Baldwin, M. P., and T. J. Dunkerton, 2001: Stratospheric harbingers of anomalous weather regimes. *Science*, **294(5542)**, 581-584, doi:10.1126/science.1063315.

Barbero, F. J., G. López, and F. J. Batlles, 2006: Determination of daily solar ultraviolet radiation using statistical models and artificial neural networks. *Ann. Geophys.*, **24**, 2105-2114.

Baumgaertner, A. J. G., P. Jöckel, H. Riede, G. Stiller, and B. Funke, 2010: Energetic particle precipitation in ECHAM5/MESSy - Part 2: Solar proton events. *Atmos. Chem. Phys.*, **10**, 7285-7302, doi:10.5194/acp-10-7285-2010.

Bethan, S., G. Vaughan, and S. J. Reid, 1996: A comparison of ozone and thermal tropopause heights and the impact of tropopause definition on quantifying the ozone content of the troposphere. *Q. J. R. Meteorol. Soc.*, **122**, 929-944.

Biniek, K., K. Levi, and R. H. Dauskardt, 2012: Solar UV radiation reduces the barrier function of human skin. *Proc. Natl. Acad. Soc. USA*, **109(42)**, 17111-17116, doi:10.1073/pnas.1206851109.

BKV, 1997: *Berufskrankheiten-Verordnung vom 31. Oktober 1997 (BGBl. | S. 2623), die zuletzt durch Artikel 1 der Verordnung vom 10. Juli 2017 (BGBl. | S. 2299) geändert worden ist.* German law.

Boers, R., T. Brandsma, and A. P. Siebesma, 2017: Impact of aerosols and clouds on decadal trends in all-sky solar radiation over the Netherlands (1966-2015). *Atmos. Chem. Phys.*, **17**, 8081-8100, doi: 10.5194/acp-17-8081-2017.

Bojkov, R. D., and D. S. Balis, 2001: Characteristics of episodes with extremely low ozone values in the northern middle latitudes 1957-2000. *Ann. Geophys.*, **19**, 797-807.

Boniol M., A. Koechlin, F. Valentini, M.-C. Chignol, J.-F. Dore, J.-L. Buillard, A. Milon, and D. Vernez, 2015: Occupational UV exposure in French oudoor workers. *J. Occup. Environ. Med.*, **57(3)**, 315-320.

Bott, A., 2016: *Synoptische Meteorologie. Methoden der Wetteranalyse und -prognose.* Springer-Verlag, Berlin, Heidelberg. XIV, 534 pp., doi: 10.1007/978-3-662-48195-0.

Bourqui, M. S., 2006: Stratosphere-troposphere exchange from the Lagrangian perspective: a case study and method sensitivities. *Atmos. Chem. Phys.*, **6**, 2651-2670.

Brasseur, G. P., and S. Solomon, 2005: *Aeronomy of the Middle Atmosphere. Chemistry and Physics of the Stratosphere and Mesosphere.* xii, 646 pp.

Brewer, A. W., 1949: Evidence for a world circulation provided by the measurements of helium and water vapour distribution in the stratosphere. *Q. J. R. Meteorol. Soc.*, **75**, 351-363, doi:10.1002/qj.49707532603.

Brönnimann, S., and L. L. Hood, 2003: Frequency of low-ozone events over northwestern Europe in 1952-1963 and 1990-2000. *Geophys. Res. Lett.*, **30(21)**, 2118, doi:10.1029/2003GL018431.

Burzlaff, J., E. Deloughry, and P. Lynch, 2008: Generation of zonal flow by resonant Rossby-Haurwitz wave interactions. *Geophys. Astrophys. Fluid Dyn.*, **102(2)**, 165-177, doi:10.1080/03091920701491576.

Butchart, N., J. Austin, J. R. Knight, A. A. Scaife, and M. L. Gallani, 2000: The response of the stratospheric climate to projected changes in the concentrations of well-mixed greenhouse gases from 1992 to 2051. *J. Climate*, **13**, 2142-2159.

Butler, A. H., D. J. Seidel, S. C. Hardiman, N. Butchart, T. Birner, and A. Match, 2015: Defining sudden stratospheric warmings. *Bull. Amer. Meteor. Soc.*, **96**, 1913-1928, doi:10.1175/BAMS-D-13-00173.1.

Calbó, J., J.-A. González, J. Badosa, R. McKenzie, and B. Liley, 2017: How large and how long are UV and total radiation enhancements? *AIP Conf. Proc.*, **1810**, 110002-1- 110002-4, doi:10.1063/1.4975564.

Calbó, J., D. Pagès, and J.-A. González, 2005: Empirical studies of cloud effects on UV radiation: A review. *Rev. Geophys.*, **43**, RG2002, doi:10.1029/2004RG000155.

Camp, C. D., and K.-K. Tung, 2007: The influence of the solar cycle and QBO on the late-winter stratospheric polar vortex. *J. Atmos. Sci.*, **64**, 1267-1283, doi:10.1175/JAS3883.1.

Canziani, P. O., R. H. Compagnucci, S. A. Bischoff, and W. E. Legnani, 2002: A study of impacts of tropospheric synoptic processes on the genesis and evolution of extreme total ozone anomalies over southern South America. *J. Geophys. Res.*, **107(D24)**, 4741, doi: 10.1029/2001JD000965.

Carslaw, K. S., R. G. Harrison, and J. Kirkby, 2002: Cosmic rays, clouds, and climate. *Science*, **298**, 1732-1737.

Cede, A., M. Blumthaler, E. Luccini, and R. D. Piacentini, 2002: Effects of clouds on erythemal and total irradiance as derived from data of the Argentine Network. *Geophys. Res. Lett*, **29(24)**, 2223-2227.

Chapman, F. R. S., 1930: On ozone and atomic oxygen in the upper atmosphere. *The London, Edinburgh, and Dublin Philosophical Magazine and Journal of Science*, **10(64)**, 369-383, doi:10.1080/14786443009461588.

Chen, T., W. B. Rossow, and Y. C. Zhang, 2000: Radiative effects of cloud-type variations. *J. Climate*, **13**, 264-286.

Chipperfield, M. P., and J. A. Pyle, 1998: Model sensitivity studies of Arctic ozone depletion. *J. Geophys. Res.*, **103(D21)**, 28,389-28,403.

Chiodo, G., L. M. Polvani, D. R. Marsh, A. Stenke, W. Ball, E. Rozanov, S. Muthers, and K. Tsigaridis, 2018: The response of the ozone layer to quadrupled CO_2 concentrations *J. Climate*, **31**, 3893-3907, doi:10.1175/JCLI-D-17-0492.1.

CIE, 2014: Rationalizing Nomenclature for UV Doses and Effects on Humans. CIE 209:2014.

WMO/GAW Report No 211. ISBN 978-3-902842-35-0.

CIE, 2002: International Standard Global UV Index. CIE DS 013.2/E:2002.

CIE, 1987: A reference action spectrum for ultraviolet induced erythema in human skin. CIE Research Note. CIE Journal 6, 17-22.

Crutzen, P. J., and F. Arnold, 1986: Nitric acid cloud formation in the cold Antarctic stratosphere: a major cause for the springtime ‚ozone hole'. *Nature*, **324**, 651-655.

Danielsen, E. F., 1968: Stratospheric-tropospheric exchange based on radioactivity, ozone and potential vorticity. *J. Atmos. Sci.*, **25**, 502-518.

Davies, P. A., 2000: Development and mechanisms of the nocturnal jet. *Meteorol. Appl.*, **7**, 239-246.

de Grandpré, J., S. R. Beagley, V. I. Fomichev, E. Griffioen, J. C. McConnell, A. S. Medvedev, and T. G. Shepherd, 2000: Ozone climatology using interactive chemistry: Results from the Canadian Middle Atmosphere Model. *J. Geophys. Res.*, **105(D21)**, 26475-26491.

di Sarra, A., M. Cacciani, P. Chamard, C. Cornwall, J. J. DeLuisi, T. Di Iorio, P. Disterhoft, G. Fiocco, D. Fuà, and F. Monteleone, 2002: Effects of desert dust and ozone on the ultraviolet irradiance at the Mediterranean island of Lampedusa during PAUR II. *J. Geophys. Res.*, **107**, NO. D18, 8135, doi:10.1029/2000JD000139.

D'Orazio, J., S. Jarrett, A. Amaro-Ortiz, and T. Scott, 2013: UV Radiation and the Skin. *Int. J. Mol. Sci.*, **14**, 12222-12248, doi:10.3390/ijms140612222.

Diepgen, T. L., M. Fartsch, H. Drexler, and J. Schmitt, 2012: Occupational skin cancer induced by ultraviolet radiation and its prevention. *Brit. J. Dermatol.*, **167(2)**, 76-84, doi:10.1111/j.1365-2133.2012.11090.x.

Diepgen, T. L., S. Brandenburg, W. Aberer, A. Bauer, H. Drexler, M. Fartasch, S. M. John, S. Krohn, S. Paffner, W. Römer, U. Schuhmacher-Stock, and P. Elsner, 2014: Skin cancer induced by natural UV-irradiation as an occupational disease - Requirements for its notification and recognition. *J. Dtsch. Dermatol. Ges.*, **12(12)**, 1102-6, doi:10.1111/ddg.12537.

DWD, 2015: Erythemal Effective UV Dose. German Meteorological Service, Human-Biometeorology.

Eisinger, M., and J. P. Burrows, 1998: Tropospheric sulfur dioxide observed by the ERS-2 GOME instrument. *Geophys. Res. Lett.*, **25(22)**, 4177-4180.

Engelsen, O., 2010: The Relationship between Ultraviolet Radiation Exposure and Vitamin D Status. *Nutrients*, **2**, 482-495, doi:10.3390/nu2050482.

Fan, J., Y. Wang, D. Rosenfeld, and X. Liu, 2016: Review of Aerosol-Cloud Interactions: Mechanisms, Significance, and Challenges. *J. Atmos. Sci.*, **73**, 4221-4252, doi:10.1175/JAS-D-16-0037.1.

Farman, J. C., B. G. Gardiner, and J. D. Shanklin, 1985: Large losses of total ozone in Antarctica reveal seasonal ClO_x/NO_x interaction. *Nature*, **315**, 207-210.

Feister, U., G. Meyer, G. Laschewski, and C. Boettcher, 2015: Validation of modeled daily erythemal exposure along tropical and subtropical shipping routes by ship-based and satellite-based measurements. *J. Geophys. Res. Atmos.*, **120**, 4117-4131, doi:10.1002/2014JD023005.

Fomin, B., and V. Falaleeva, 2012: A polarized atmospheric radiative transfer model for calculations of spectra of the Stokes parameters of shortwave radiation based on the Line-by-Line and Monte Carlo methods. *Atmosphere*, **3**, 451-467, doi:10.3390/atmos3040451.

Foyo-Moreno, I., I. Alados, F. J. Olmo, and L. Alados-Arboledas, 2003: The influence of cloudiness on UV global irradiance (295-385 nm). *Agric. For. Meteorol.*, **120**, 101-111, doi:10.1016/j.agrformet.2003.08.023.

Foyo-Moreno, I., I. Alados, F. J. Olmo, J. Vida, and L. Alados-Arboledas, 2001: On the use of a cloud modification factor for solar UV (290-385 nm) spectral range. *Theor. Appl. Climatol.*, **68**, 41-50.

Fragkos, K., A. F. Bais, I. Fountoulakis, D. S. Balis, K. Tourpali, C. Meleti, and P. Zanis, 2016: Extreme total column ozone events and effects on UV solar radiation at Thessaloniki, Greece. *Theor. Appl. Climatol.*, **126**, 505-517, doi:10.1007/s00704-015-1562-3.

Fröhlich, C., 2006: Solar Irradiance Variability since 1978 *Space Sci. Rev.*, **125**, 53-65, doi:10.1007/s11214-006-9046-5.

Garrat, J. R, 1994: Review: the atmospheric boundary layer. *Earth-Sci. Rev.*, **37**, 89-134.

Gillotay, D., D. Bolsée, and T. Besnard, 2005: *Attenuation of solar UV irradiances by different types of cloud condition: A potential improvement for UV indices forecast.* https://www.researchgate.net/publication/253712244.

Grant, R. H., and W. Gao, 2003: Diffuse fraction of UV radiation under partly cloudy skies as defined by the Automated Surface Observation System (ASOS). *J. Geophys. Res.*, **108(D2)**, 4046, doi:10.1029/2002JD002201.

Gray, L., S. Rumbold, and K. Shine, 2009: Stratospheric Temperature and Radiative Forcing Response to 11-Year Solar Cycle Changes in Irradiance and Ozone. *J. Atmos. Sci.*, **66**, 2402-2417.

Greinert, R., E. de Vries, F. Erdmann, C. Espina, A. Auvinen, A. Kesminiene, and J. Schüz, 2015: European Code against Cancer 4th Edition: Ultraviolet radiation and cancer. *Cancer Epidemiol.*, **39S**, S75-S83, doi:10.1016/j.canep.2014.12.014.

Hartmann, D. L., J. M. Wallace, V. Limpasuvan, D. W. J. Thompson, and J. R. Holton, 2000: Can ozone depletion and global warming interact to produce rapid climate change? *Proc. Natl. Acad. Sci. USA*, **97(4)**, 1412-1417.

Haynes, P. H., C J. Marks, M. E. McIntyre, T. G. Shepherd, and K. P. Shine, 1991: On the "Downward Control" of Extratropical Diabatic Circulations by Eddy-Induced Mean Zonal Forces. *J. Atmos. Sci.*, **48(4)**, 651-678.

Heisler, G. M., and R. H. Grant, 2000: Ultraviolet radiation in urban ecosystems with consideration of effects on human health. *Urban Ecosyst.*, **4**, 193-229.

Herlihy, E., P. H. Gies, C. R. Rov, and M. Jones, 1994: Personal Dosimetry of Solar UV Radiation for Different Outdoor Activities. *Photochem. Photobiol.*, **60(3)**, 288-294.

Hoinka, K. P., H. Claude, and U. Köhler, 1996: On the correlation between tropopause pressure and ozone above Central Europe. *Geophys. Res. Lett.*, **23(14)**, 1753-1756.

Holick, M. F., 2008: Vitamin D and Sunlight: Strategies for Cancer Prevention and Other Health Benefits. *Clin. J. Am. Soc. Nephrol.*, **3(5)**, 1548-1554.

Holton, J. R., 2004: *An Introduction to Dynamic Meteorology, Fourth Edition.* 529 pp.

Holton, J. R., P. H. Haynes, M. E. McIntyre, A. R. Douglas, R. B. Rood, and L. Pfister, 1995: Stratosphere-Troposphere Exchange. *Rev. Geophys.*, **33(4)**, 403-439.

Holton, J. R., 1990: Notes and Correspondence. On the global exchange of mass between the stratosphere and troposphere. *J. Atmos. Sci.*, **47(3)**, 392-395.

Hoskins, B. J., 1991: Towards a PV-θ view of the general circulation. *Tellus*, **43AB**, 27-35.

Hu, B., X. Zhao, H. Liu, Z. Liu, T. Song, Y. Wang, L. Tang, X. Xia, G. Tang, D. Ji, T. Wen, L. Wang, Y. Sun, and J. Xin, 2017: Quantification of the impact of aerosol on broadband solar radiation in North China. *Sci. Rep.*, **7**, 44851, doi:10.1038/srep44851.

Hu, L.-W., Q. Gao, W.-Y. Xu, Y. Wang, H.-Z. Gong, G.-Q. Dong, J.-H. Li, and Y. Liu, 2010: Diurnal Variations in Solar Ultraviolet Radiation at Typical Anatomical Sites. *Biomed. Environ. Sci.*, **23**, 234-243.

Iwao, K., and T. Hirooka, 2006: Dynamical quantifications of ozone minihole formation in both hemispheres. *J. Geophys. Res.*, **111**, D02104, doi:10.1029/2005JD006333.

Jablonski, N. G., and G. Chaplin, 2010: Human skin pigmentation as an adaption to UV radiation. *Proc. Natl. Acad. Sci.*, **107(2)**, 8962-8968, doi:10.1073/pnas.0914628107.

Jackman, C. H., D. R. Marsh, F. M. Vitt, R. R. Garcia, E. L. Fleming, G. J. Labow, C. E. Randall, M. López-Puertas, and B. Funke, 2007: Short- and medium-term atmospheric effects of very large solar proton events. *Atmos. Chem. Phys. Discuss.*, **7**, 10543-10588.

Jackman, C. H., and E. L. Fleming, 2000: Influence of extremely large solar proton events in a changing stratosphere. *J. Geophys. Res.*, **105(D9)**, 11,659-11,670.

James, P. M., 1998: A climatology of ozone mini-holes over the northern hemisphere. *Int. J. Climatol.*, **18**, 1287-1303.

James, P. M., D. Peters, and K. M. Greisiger, 1997: A study of ozone mini-hole formation using a tracer advection model driven by barotropic dynamics. *Meteorol. Atmos. Phys.*, **64**, 107-121.

Jonsson, A. I., J. de Grandpré, V. I. Fomichev, J. C. McConnell, and S. R. Beagley, 2004: Doubled CO_2-induced cooling in the middle stratosphere: Photochemical analysis of the ozone radiative feedback. *J. Geophys. Res.*, **109**, D24103, doi:10.1029/2004JD005093.

Junge, C. E., C. W. Chagnon, and J. E. Manson, 1961: A world-wide stratospheric aerosol layer. *Science*, **133(3463)**, 1478-1479, doi:10.1126/science.133.3463.1478-a.

Juzeniene, A., P. Brekke, A. Dahlback, S. Andersson-Engels, J. Reichrath, K. Moan, M. F. Holick, W. B. Grant, and J. Moan, 2011: Solar radiation and human health. *Rep. Prog. Phys.*, **74**, 066701 (56pp), doi:10.1088/0034-4885/74/6/066701.

Keil, M., D. R. Jackson, and M. C. Hort, 2007: The January 2006 low ozone event over the UK. *Atmos. Chem. Phys.*, **7**, 961-972.

Kelbch, A., M. Wittlich, and A. Bott, 2019: Quantifying the effects of a low-ozone event and shallow stratocumulus clouds on ultraviolet erythemal radiation exposure. *Int. J. Biometeorol.*, **63**, 359-369, doi:10.1007/s00484-018-01669-8.

Koch, G., H. Wernli, J. Staehelin, and T. Peter, 2003: Reply to comment by H. Teitelbaum et al. on "A Lagrangian analysis of stratospheric ozone variability and long-term trends above Payerne (Switzerland) during 1970-2001." *J. Geophys. Res.*, **108(D21)**, 4675, doi:10.1029/2003JD003911.

Koch, G., H. Wernli, J. Staehelin, and T. Peter, 2002: A Lagrangian analysis of stratospheric ozone variability and long-term trends above Payerne (Switzerland) during 1970-2001. *J. Geophys. Res.*, **107(0)**, ACL, doi:10.1029/2001JD001550.

Kopp, G., 2016: Magnitudes and timescales of total solar irradiance variability. *J. Space Weather Space Clim.*, **6**, A30, doi: 10.1051/swsc/2016025.

Kopp, G., and J. Lean, 2011: A new, lower value of total solar irradiance: Evidence and climate significance. *Geophys. Res. Lett.*, **38**, L01706, doi: 10.1029/2010GL045777.

Kopp, G., G. Lawrence, and G. Rottman, 2005: The total irradiance monitor (TIM): Science results. *Solar Phys.*, **239**, 129-139.

Kraus, H., and U. Ebel, 1989: Atmospheric boundary layer characteristics in severe smog episodes. *Meteorol. Atmos. Phys.*, **40**, 211-224.

Kren, A. C., 2015: *"Investigating the Role of the Sun, the Quasi-Biennial Oscillation, and the Pacific Decadal Oscillation on Decadal Climate Variability of the Stratosphere".* Atmospheric & Oceanic Sciences Graduate Theses & Dissertations. 52. https://scholar.colorado.edu/atoc_gradetds/52.

Krzyścin, J. W., 2002: Long-term changes in ozone mini-hole event frequency over the Northern Hemisphere derived from ground-based measurements. *Int. J. Climatol.*, **22**, 1425-1439, doi:10.1002/joc.812.

Labitzke, K., and M. Kunze, 2009: *Variability in the stratosphere: The sun and the QBO. TERRAPUB, Tokyo, 2009* Climate and Weather of the Sun-Earth System (CAWSES): Selected Papers from the 2007 Kyoto Symposiumpp. 257-278.

Lindfors, A. V., J. Kujanpää, N. Kalakoski, A. Heikkilä, K. Lakkala, T. Mielonen, M. Sneep, N. A. Krotkov, A. Arola, and J. Tamminen, 2018: The TROPOMI surface UV algorithm. *Atmos. Meas. Tech.*, **11**, 997-1008, doi:10.5194/amt-11-997-2018.

Liu, S. C., S. A. McKeen, and S. Madronich, 1991: Effect of anthropogenic aerosols on biologically active ultraviolet radiation. *Geophys. Res. Lett.*, **18(12)**, 2265-2268.

Long, C. N., and T. P. Ackermann, 2000: Identification of clear skies from broadband pyranometer measurements and calculation of downwelling shortwave cloud effects. *J. Geophys. Res.*, **105(D12)**, 15,609-15,626.

Lu, H., T. J. Bracegirdle, T. Phillips, A. Bushell, and L. Gray, 2014: Mechanisms for the Holton-Tan relationship and its decadal variation. *J. Geophys. Res. Atmos.*, **119**, 2811-2830, doi:10.1002/2013JD021352.

Madronich, S., 2007: Analytic Formula for the clear-sky UV Index. *Photochem. Photobiol.*, **83**, 1537-1538, doi:10.1111/j.1751-1097.2007.00200.x.

Madronich, S., 1993: *UV radiation in the natural and perturbed atmosphere in Environmental Effects of Ultraviolet Radiation,* edited by M. Tevini, pp. 17–69, Lewis, Boca Raton, Fla.

Mahrt, L., and D. Vickers, 2006: Extremely weak mixing in stable conditions. *Boundary-Layer Meteorol.*, **119**, 19-39, doi:10.1007/s10546-005-9017-5.

Marshall, J. S., and W. McK. Palmer, 1948: Shorter contributions. The distribution of raindrops with size. *J. Meteor.*, **5**, 165-166.

Martínez-Lozano, J., M. Utrillas, J. Núñez, J. Tamayo, M. Marín, A. Esteve, J. Cañada, and J. Moreno, 2011: Ozone mini-holes over Valencia (Spain) and their influence on the UV erythemal radiation. *Int. J. Climatol.*, **31**, 1554-1566.

Mateos, D., A. di Sarra, J. Bilbao, D. Meloni, G. Pace, A. de Miguel, and G. Casasanta, 2015: Spectral attenuation of global and diffuse UV irradiance and actinic flux by clouds. *Q. J. R. Meteorol. Soc.*, **141**, 109-113.

Matuszko, D., 2012: Influence of the extent and genera of cloud cover on solar radiation intensity. *Int. J. Climatol.*, **32**, 2403-2414, doi: 10.1002/joc.2432.

Maury, P., C. Claud, E. Manzini, A. Hauchecorne, and P. Keckhut, 2016: Characteristics of stratospheric warming events during Northern winter. *J. Geophys. Res. Atmos.*, **121**, 5368-5380, doi:10.1002/2015JD024226.

Mayer, B., A. Kylling, S. Madronich, and G. Seckmeyer, 1998: Enhanced absorption of UV radiation due to multiple scattering in clouds: Experimental evidence and theoretical explanation. *J. Geophys. Res.*, **103**, 31,241-31,254.

McConnell, J. C., and J. J. Jin, 2008: Stratospheric Ozone Chemistry. *Atmos. Ocean*, **46(1)**, 69-92, doi: 10.3137/ao.460104.

McCormack, J. P., L. L. Hood, 1997: The frequency and size of ozone "mini-hole" events at northern midlatitudes in February. *Geophys. Res. Lett.*, **24(21)**, 2647-2650.

McKenzie, R., B. Liley, M. Kotkamp, and P. Disterhoft, 2017: Peak UV: Spectral Contributions from Cloud Enhancements. *AIP Conf. Proc.*, **1810**, 110008-1- 110008-4, doi:10.1063/1.4975570.

McKenzie, R. L., P. J. Aucamp, A. F. Bais, L. O. Björn, M. Ilyas, and S Madronich, 2011: Ozone depletion and climate change: impacts on UV Radiation. *Photochem. Photobiol. Sci.*, **10**, 182-198, doi: 10.1039/c0pp90034f.

McKenzie, R. L., J. B. Liley, and L. O. Björn, 2009: UV Radiation: Balancing Risks and Benefits. *Photochem. Photobiol.*, **85**, 88-98, doi: 10.1111/j.1751-1097.2008.00400.x.

McKenzie, R. L., W. A. Matthews, and P. V. Johnston, 1991: The Relationship between erythemal UV and Ozone derived from spectral Irradiance Measurements. *Geophys. Res. Lett.*, **18(12)**, 2269-2272.

Mie, G., 1908: Beiträge zur Optik trüber Medien, speziell kolloidaler Metallösungen. *Ann. d. Phys.*, **25(4)**, 377-445.

Millán, L. F., and G. L. Manney, 2017: An assessment of ozone mini-hole representation in reanalyses over the Northern Hemisphere. *Atmos. Chem. Phys.*, **17**, 9277-9289, doi:10.5194/acp17-9277-2017.

Milon, A., J.-L. Bulliard, L. Vuilleumier, B. Danuser, and D. Vernez, 2014: Estimating the contribution of occupational solar ultraviolet exposure to skin cancer. *Br. J. Dermatol.*, **170**, 157-164, doi:10.1111/bjd.12604.

Montreal Protocol, 1987: *Montreal Protocol on substances that deplete the ozone layer (with annex). No. 26369.* Vol. 1522, 1-26369.

Montzka, S. A., G. S. Dutton, P. Yu, E. Ray, R. W. Portmann, J. S. Daniel, L. Kuijpers, B. D. Hall, D. Mondeel, C. Siso, J. D. Nance, M. Rigby, A. J. Manning, L. Hu, F. Moore, B. R. Miller, and J. W. Elkins, 2018: An unexpected and persistent increase in global emissions of ozone-depleting CFC-11. *Nature*, **557**, 413-417, doi:10.1038/s41586-018-0106-2.

Newman, P. A., L. R. Lait, and M. R. Schoeberl, 1988: The morphology and meteorology of southern hemisphere spring total ozone mini-holes. *Geophys. Res. Lett.*, **15(8)**, 923-926, doi:10.1029/GL015i008p00923.

Orlanski, I., 1975: A rational subdivision of scales for atmospheric processes. *Bull. Amer. Meteor. Soc.*, **56(5)**, 527–530.

Palmén, E., and C. W. Newton, 1969: *Atmospheric Circulation Systems.* Academic Press, New York, London, 603 pp.

Peng, J., M. Hu, S. Guo, Z. Du, J. Zheng, D. Shang, M. L. Zamora, L. Zeng, M. Shao, Y.-S. Wu, J. Zheng, Y. Wang, C. R. Glen, D. R. Collins, M. J. Molina, and R. Zhang, 2016b: Markedly enhanced absorption and direct radiative forcing of black carbon under polluted urban environments. *Proc. Natl. Amer. Soc. USA*, **113(16)**, 4266-4271, doi:10.1073/pnas.1602310113.

Pérez, A., I. Aguirre de Cárcer, and F. Jaque, 2002: Low ozone event at Madrid in November 1996. *J. Atmos. Solar-Terr. Phys.*, **64**, 283-289.

Pérez, A., E. Crino, I. Aguirre de Cárcer, and F. Jaque, 2000: Low-ozone events and three-dimensional transport at midlatitudes of South America during springs of 1996 and 1997. *J. Geophys. Res.*, **105(D4)**, 4553-4561.

Peters, D., J. Egger, and G. Entzian, 1995: Dynamical aspects of ozone mini-hole formation. *Meteorol. Atmos. Phys.*, **55**, 205-214.

Petkov B., V. Vitale, C. Tomasi, A. Siani, G. Seckmeyer, A. Webb, A. Smedley, G. Casale, R. Werner, C. Lanconelli, M. Mazzola, A. Lupi, M. Busetto, H. Diémoz, F. Goutail, U. Köhler, B. D. Mendeva, W. Josefsson, D. Moore, M. Bartolomé, J. González, O. Mišaga, A. Dahlback, Z. Tóth, S. Varghese, H. De Backer, R. Stübi, K. Vaníček, 2014: Response of the ozone column over Europe to the 2011 Arctic ozone depletion event according to ground-based observations and assessment of the consequent variations in surface UV irradiance. *Atmos. Environ.*, **85**, 169-178.

Petropavlovskikh, I., R. Evans, G. McConville, G. L. Manney, and H. E. Rieder, 2015: The influence of the North Atlantic Oscillation on mean and extreme values of column ozone over the United States. *Atmos. Chem. Phys.*, **15**, 1585-1598, doi:10.5194/acp-15-1585-2015.

Probert-Jones, J. R., 1962: The radar equation in meteorology. *Q. J. R. Meteorol. Soc.*, **88 (378)**, 485-495.

Pruppacher, H. R. and J. D. Klett, 1997: *Microphysics of Clouds and Precipitation.* Kluwer Academic Publishers, Dordrecht, The Netherlands, 954 pp.

Randall, C. E., V. L. Harvey, C. S. Singleton, S. M. Bailey, P. F. Bernath, M. Codrescu, H. Nakajima, and J. M. Russell III, 2007: Energetic particle precipitation effects on the Southern Hemisphere stratosphere in 1992-2005. *J. Geophys. Res.*, **112**, D08308, doi:10.1029/2006JD007696.

Reed, R. J., 1950: The role of vertical motions in ozone-weather relationships. *J. Meteor.*, **7**, 263-267.

Reichrath, J., 2007: Vitamin D and the skin: an ancient friend, revisited *Exp. Dermatol.*, **16**, 618-625, doi:10.1111/j.1600-0625.2007.00570.x.

Rieckh, T., B. Scherllin-Pirscher, F. Ladstädter, and U. Foelsche, 2014: Characteristics of tropopause parameters as observed with GPS radio occultation *Atmos. Meas. Tech.*, **7**, 3947-3958.

Rieder, H. E., J. Staehelin, J. A. Maeder, T. Peter, M. Ribatet, A. C. Davison, R. Stübi, P. Weihs, and F. Holawe, 2010: Extreme events in total ozone over Arosa - Part 1: Application of extreme value theory. *Atmos. Chem. Phys.*, **10**, 10021-10031, doi:10.5194/acp-10-10021-2010.

Rigby, M., S. Park, T. Saito, L. M. Western, A. L. Redington, X. Fang, S. Henne, A. J. Manning, R. G. Prinn, G. S. Dutton, P. J. Fraser, A. L. Ganesan, B. D. Hall, C. M. Harth, J.

Kim, K.-R. Kim, P. B. Krummel, T. Lee, S. Li, Q. Liang, M. F. Lunt, S. A. Montzka, J. Mühle, S. O'Doherty, M.-K. Park, S. Reimann, P. K. Salameh, P. Simmonds, R. L. Tunnicliffe, R. F. Weiss, Y. Yokouchi, and D. Young, 2019: Increase in CFC-11 emissions from eastern China based on atmospheric observations. *Nature*, **569**, 546-550, doi:10.1038/s41586-019-1193-4.

Rind, D., P. Lonergna, N. K. Balachandran, and D. Shindell, 2002: 2xCO_2 and solar variability influences on the troposphere through wave-mean flow interactions. *J. Meteor. Soc. Japan*, **80(4B)**, 863-876.

Rohen, G., C. von Savigny, M. Sinnhuber, E. J. Llewellyn, J. W. Kaiser, C. H. Jackman, M.-B. Kallenrode, J. Schröter, K.-U. Eichmann, H. Bovensmann, and J. P. Burrows, 2005: Ozone depletion during the solar proton events of October/November 2003 as seen by SCIAMACHY. *J. Geophys. Res.*, **110**, A09S39, doi:10.1029/2004JA010984.

Román, R. M. Antón, A. Valenzuela, J. E. Gil, H. Lyamani, A. De Miguel, F. J. Olmo, J. Bilbao, and L. Alados-Arboledas, 2013: Evaluation of the desert dust effects on global, direct and diffuse spectral ultraviolet irradiance *Tellus B*, **665**, 19578, doi:10.3402/tellusb.v65i0.19578.

Rood, R. B., J. E. Nielsen, R. S. Stolarski, A. R. Douglass, J. A. Kaye, and D. J. Allen, 1992: Episodic total ozone minima and associated effects on Heterogeneous chemistry and lower stratospheric transport. *J. Geophys. Res.*, **97(D8)**, 7979-7996.

Rosenfeld, D., 1999: TRMM observed first direct evidence of smoke from forest fires inhibiting rainfall. *Geophys. Res. Lett.*, **26(20)**, 3105-3108, doi:10.1111/ics.12219.

Santos, J. B., D. M. Villán, and A. de Miguel Castrillo, 2011: Analysis and cloudiness influence on UV total irradiation. *Int. J. Climatol.*, **31**, 451-460, doi: 10.1002/joc.2072.

Schoeberl, M. R., and D. L. Hartmann, 1991: The dynamics of the stratospheric Polar Vortex and its relation to springtime ozone depletions. *Science*, **251(4989)**, 46-52, doi:10.1126/science.251.4989.46.

Schwartz, S. E., and P. Warneck, 1995: Units for use in atmospheric chemistry. IUPAC recommendations 1995. *Pure & Appl. Chem.*, **67(8/9)**, 1377-1406.

Schwarz, M., D. J. Baumgartner, H. Pietsch, M. Blumthaler, P. Weihs, and H. E. Rieder, 2018: Influence of low ozone episodes on erythemal UV-B radiation in Austria. *Theor. Appl. Climatol.*, **133**, 319-329, doi:10.1007/s00704-017-2170-1.

Serrano, A., M. Antón, M. L. Cancillo, and V. L. Mateos, 2006: Daily and annual variations of erythemal ultraviolet radiation in Southwestern Spain. *Ann. Geophys.*, **24**, 427-441.

Setlow, R. B., E. Grist, K. Thompson, and A. D. Woodhead, 1993: Wavelengths effective in induction of malignant melanoma. *Proc. Natl. Acad. Sci. USA*, **90**, 6666-6670.

Setlow, R. B., 1974: The wavelengths in sunlight effective in producing skin cancer: A theoretical analysis. *Proc. Natl. Acad. Sci. USA*, **71(9)**, 3363-3366.

Siani, A. M., G. R. Casale, R. Sisto, A. Colosimo, C. A. Lang, and M. G. Kinlin, 2011: Occupational Exposures to Solar Ultraviolet Radiation of Vineyard Workers in Tuscany (Italy). *Photochem. Photobiol.*, **87**, 925-934, doi:10.1111/j.1751-1097.2011.00934.x.

Škerlak, B., M. Sprenger, and H. Wernli, 2014: A global climatology of stratosphere-troposphere exchange using the ERA-Interim data set from 1979 to 2011. *Atmos. Chem. Phys.*, **14**, 913-937, doi:10.5194/acp-14-913-2014.

Sklar, L. R., F. Almutawa, H. W. Lim, and I. Hamzavi, 2013: Effects of ultraviolet radiation, visible light, and infrared radiation on erythema and pigmentation: a review. *Photochem. Photobiol. Sci.*, **12**, 54-64, doi:10.1039/c2pp25152c.

Sola, Y., and J. Lorente, 2011: Impact of two low ozone events on surface solar UV radiation over the northeast of Spain. *Int. J. Climatol.*, **31**, 1724-1734, doi:10.1002/joc.2194.

Solomon, S., 1999: Stratospheric Ozone Depletion: A Review of Concepts and History. *Rev. Geophys.*, **37(3)**, 275-316.

Solomon, S., R. R. Garcia, F. S. Rowland, and D. J. Wuebbles, 1986: On the depletion of Antarctic ozone. *Nature*, **321**, 755-758.

Staiger, H., and P. Koepke, 2005: UV Index forecasting on a global scale. *Meteorol. Z.*, **14(2)**, 259-270, doi:10.1127/0941-2948/2005/0029.

Stevens, B., 2007: On the growth of layers of nonprecipitating cumulus convection. *J. Atmos. Sci.*, **64**, 2916-2931, doi:10.1175/JAS3983.1.

Stohl, A., P. Bonasoni, P. Cristofanelli, W. Collins, J. Feichter, A. Frank, C. Forster, E. Gerasopoulos, H. Gäggeler, P. James, T. Kentarchos, H. Kromp-Kolb, B. Krüger, C. Land, J. Meloen, A. Papayannis, A. Priller, P. Seibert, M. Sprenger, G. J. Roelofs, H. E. Scheel, C. Schnabel, P. Siegmund, L. Tobler, T. Trickl, H. Wernli, V. Wirth, P. Zanis, and C. Zerefos, 2003: Stratosphere-troposphere exchange: A review, and what we have learned from STACCATO. *J. Geophys. Res.*, **108(D12)**, 8516, doi:10.1029/2002JD002490.

Stolarski, R. S., A. R. Douglass, M. Gupta, P. A. Newman, S. Pawson, M. R. Schoeberl, and J. E. Nielsen, 2006: An ozone increase in the Antarctic summer stratosphere: A dynamical response to the ozone hole. *Geophys. Res. Lett.*, **33**, L21805, doi:10.1029/2006GL026820.

Stolarski, R. S., A. J. Krieger, M. R. Schoeberl, R. D. McPeters, P. A. Newman, and J. C. Alpert, 1986: Nimbus 7 satellite measurements of the springtime Antarctic ozone decrease. *Nature*, **322**, 808-811.

Svensmark, H., and E. Friis-Christensen, 1997: Variation of cosmic ray flux and global cloud coverage - a missing link in solar-climate relationships *J. Atmos. Solar-Terr. Phys.*, **59(11)**, 1225-1232.

Taalas, P., J. Damski, and E. Kyrö, 1997: Effect of stratospheric ozone variations on UV radiation and on tropospheric ozone at high latitudes. *J. Geophys. Res.*, **102**, 1533-1539.

Teitelbaum, H., M. Moustaoui, and M. Fromm, 2001: Exploring polar stratospheric cloud and ozone minihole formation: The primary importance of synoptic-scale flow perturbations. *J. Geophys. Res.*, **106(D22)**, 28.173-28,188.

Thackeray, C. W., and A. Hall, 2019: An emergent constraint on future Arctic sea-ice albedo feedback. *Nat. Clim. Change*, **9**, 972-978, doi:10.1038/s41558-019-0619-1.

Thieden, E., P. A. Philipsen, J. Heydenreich, H. C. Wulf, 2004: UV Radiation Exposure Related to Age, Sex, Occupation, and Sun Behavior Based on Time-Stamped Personal Dosimeter Readings. *Arch. Dermatol.*, **140**, 197-203.

Thompson, D. W. J., M. P. Baldwin, and J. M. Wallace, 2002: Stratospheric circulation to Northern hemisphere wintertime weather: Implications for prediction. *J. Climate*, **15**, 1421-1428.

Thuillier, G., J.-M. Perrin, P. Keckhut, and F. Huppert, 2013: Local enhanced solar irradiance on the ground generated by cirrus: measurements and interpretation. *J. Appl. Remote Sens.*, **7**, 073543, doi:10.1117/1.JRS.7.073543.

Trenberth, K. E., J. T. Fasullo, and J. Kiehl, 2009: Earth's global energy budget. *Bull. Amer. Meteor. Soc.*, **90(3)**, 311-324, doi:10.1175/2008BAMS2634.1.

Tsiaras, W. G., and M. A. Weinstock, 2011: Factors Influencing Vitamin D Status. *Acta. Derm. Venereol.*, **91**, 115-124.

Twomey, S., 1977: The influence of pollution on the shortwave albedo of clouds. *J. Atmos. Sci.*, **34**, 1149-1152.

Vernez, D., A. Milon, L. Vuilleumier, and J.-L. Bulliard, 2012: Anatomical exposure patterns of skin to sunlight: relative contributions of direct, diffuse and reflected ultraviolet radiation. *Br. J. Dermatol.*, **167**, 383-390, doi:10.1111/j.1365-2133.2012.10898.x.

Vernez, D., A. Milon, L. Francioli, J.-L. Bulliard, L. Vuilleumier, and L. Moccozet, 2011: A numeric model to simulate solar individual ultraviolet exposure. *Photochem. Photobiol.*, **87**, 721-728, doi:10.1111/j.1751-1097.2011.00895.x.

Waibel, A. E., T. Peter, K. S. Carslaw, H. Oelhaf, G. Wetzel, P. J. Crutzen, U. Pöschl, A. Tsias, E. Reimer, and H. Fischer, 1999: Arctic ozone loss due to denitrification. *Science*, **283(5410)**, 2064-2069, doi:10.1126/science.283.5410.2064.

Wang, F., T. Ge, Q. Gao, L. Hu, J. Yu, and Y. Liu, 2014: The distribution of biologically effective UV spectral irradiances received on a manikin face that cause erythema and skin cancer. *J. Photochem. Photobiol. B - Biol.*, **140**, 205-214, doi:10.1016/j.jphotobiol.2014.08.004.

Wargan, K., C. Orbe, S. Pawson, J. R. Ziemke, L. D. Oman, M. A. Olsen, L. Coy, and K. E. Knowland, 2018: Recent decline in extratropical lower stratospheric ozone attributed to circulation changes. *Geophys. Res. Lett.*, **45**, 5166-5176, doi:10.1029/2018GL077406.

Watson, M., D. M. Holman, and M. Maguire-Eisen, 2016: Ultraviolet Radiation Exposure and Its Impact on Skin Cancer Risk. *Semin. Oncol. Nurs.*, **32(3)**, 241-254, doi:10.1016/j.soncn.2016.05.005.

Waugh, D. W., A. H. Sobel, and L. M. Polvani, 2017: What is the Polar Vortex and how does it influence weather. *Bull. Amer. Meteor. Soc.*, , 37-44, doi:10.1175/BAMS-D-15-00212.1.

Wernli, H., and M. Bourqui, 2002: A Lagrangian "1-year climatology" of (deep) cross-tropopause exchange in the extratropical Northern Hemisphere. *J. Geophys. Res.*, **107(D2)**, 4021, doi:10.1029/2001JD000812.

Wittlich, M., S. Westerhausen, P. Kleinespel, G. Rifer, and W. Stöppelmann, 2016: An approximation of occupational lifetime UVR exposure: algorithm for retrospective assessment and current measurements. *J. Eur. Acad. Dermatol. Venereol.*, **30(3)**, 27-33.

Wolfram, E. A., F. Orte, J. Salvador, J. Quiroga, R. D'Elia, M. Antón, L. Alados-Arboledas, and E. Quel, 2017: Study of cloud modification factors in Southern Patagonia. *AIP Conf. Proc.*, **1810**, 110012, doi:10.1063/1.4975574.

Wood, R., 2012: Review stratocumulus clouds. *Mon. Wea. Rev.*, **140**, 2373-2423, doi:10.1175/MWR-D-11-00121.1.

World Meteorological Organization, 2017: *Manual on Codes. International Codes.* WMO-No. 306, 2011 edition, updated in 2017.

World Meteorological Organization, 2010b: *Instruments to measure solar ultraviolet radiation, Part 3: multi-channel filter instruments.* WMO-No. 190, WMO/TD-No. 1537, July 2010.

World Meteorological Organization, 2010: *Guide to Meteorological Instruments and Methods of Observation.* WMO-No. 8, 2008 edition, updated in 2010.

World Meteorological Organization: *Global Ozone Research and Monitoring Project - Report No. 52. Scientific Assessment of Ozone Depletion: 2010. Twenty Questions and Answers about the Ozone Layer: 2010 Update.* https://www.esrl.noaa.gov/csd/assessments/ozone/2010/twentyquestions/

Wright, C. Y., M. Norval, B. Summers, L. M. Davids, G. Coetzee, and M. Oriowo, 2012: Solar ultraviolet radiation exposure and human health in South Africa: Finding a balance. *S. Afr. Med. J.*, **102(8)**, 665-666, doi:10.7196/SAMJ.5921.

Xia, S., A. M. Mestas-Nuñez, H. Xie, J. Tang, and R. Vega, 2018: Characterizing variability of solar irradiance in San Antonio, Texas using satellite observations of cloudiness *Remote Sens.*, **10**, 2016, doi:10.3390/rs10122016.

Zdunkowski, W., T. Trautmann, and A. Bott, 2007: *Radiation in the Atmosphere. A Course in Theoretical Meteorology.* Cambridge University Press, Cambridge, 482 pp.

Zhang, J., W. Tian, F. Xie, M. P. Chipperfield, W. Feng, S.-W. Son, N. L. Abraham, A. T. Archibald, S. Bekki, N. Butchart, M. Deushi, S. Dhomse, Y. Han, P. Jöckel, D. Kinnison, O. Kirner, M. Michou, O. Morgenstern, F. M. O'Connor, G. Pitari, D. A. Plummer, L. E. Revell, E. Rozanov, D. Visioni, W. Wang, and G. Zeng, 2018: Stratospheric ozone loss over the Eurasian continent induced by the polar vortex shift. *Nat. Commun.*, **9(206)**, 1-8.

Alphabetical index

Acknowledgements

After more than four years of working, measuring, analyzing and writing - an in many ways very intense period of time - I was very happy to submit the thesis at hand. Along the way many people supported and helped me to get the job done - a big thank you to all of them especially to

- Prof. Dr. Andreas Bott for the opportunity to start a PhD project in his working group and for his supervision, support and a lot of patience.

- the German Social Accident Insurance (DGUV) for providing financial support in form of a PhD grant.

- the Institute for Occupational Safety and Health of the DGUV for providing the measurement equipment and great support regarding the conduction of the many measurements.

- K. Baczynska and her colleagues at Public Health England (PHE) for their great support and hosting during the low-ozone event measurements.

- the Institute for Work and Health (IST) in Lausanne for the access to the SimUVEx model (D. Vernez) and for the support in executing the model simulations (A. Milon).

- my parents, my sister and close family members for offering welcome changes to my daily routine by Swabian food supply, talking and listening.

- all my friends and relatives for their interest, many good wishes and positive support.

- my room mates Stina and Philipp for positive vibes, super delicious pasta variations as well as some nice joint dinners and barbecue events on the balcony. Special thanks to my former room mate Felix for a good time and very effective sporting activities.

- some other special people ...

- both of my SCOBY cultures for their reliable support in keeping me healthy.

BONNER METEOROLOGISCHE ABHANDLUNGEN

Herausgegeben vom Institut für Geowissenschaften der Universität Bonn, Abteilung Meteorologie, durch Prof. Dr. H. FLOHN (Hefte 1-25), Prof. Dr. M. HANTEL (Hefte 26-35), Prof. Dr. H.-D. SCHILLING (Hefte 36-39), Prof. Dr. H. KRAUS (Hefte 40-49), ab Heft 50 durch Prof. Dr. A. HENSE.

Heft 1-69: siehe `http://www.meteo.uni-bonn.de/bibliothek/bma`

70-90: open access, verfügbar unter `https://uni-bn.de/kpSDaQffe1`

Heft 70: ***A S M Mostaquimur Rahman***: Influence of subsurface hydrodynamics on the lower atmosphere at the catchment scale, 2015, 98 S. + XVI.

Heft 71: ***Sabrina Wahl***: Uncertainty in mesoscale numerical weather prediction: probabilistic forecasting of precipitation, 2015, 108 S.

Heft 72: ***Markus Übel***: Simulation of mesoscale patterns and diurnal variations of atmospheric CO_2 mixing ratios with the model system TerrSysMP-CO_2, 2015, [erschienen] 2016, 158 S. + II

Heft 73: ***Christian Bernardus Maria Weijenborg***: Characteristics of Potential Vorticity anomalies associated with mesoscale extremes in the extratropical troposphere, 2015, [erschienen] 2016, 151 S. + XI

Heft 74: ***Muhammad Kaleem***: A sensitivity study of decadal climate prediction to aerosol variability using ECHAM6-HAM (GCM), 2016, 98 S. + XII

Heft 75: ***Theresa Bick***: 3D Radar reflectivity assimilation with an ensemble Kalman filter on the convective scale, 2016, [erschienen] 2017, 96 S. + IX

Heft 76: ***Zied Ben Bouallegue***: Verification and post-processing of ensemble weather forecasts for renewable energy applications, 2017, 119 S.

Heft 77: ***Julia Lutz***: Improvements and application of the STatistical Analogue Resampling Scheme STARS, 2016, [erschienen] 2017, 103 S.

Heft 78: ***Benno Michael Thoma***: Palaeoclimate Reconstruction in the Levant and on the Balkans, 2016, [erschienen] 2017, XVI, 266 S.

Heft 79: ***Ieda Pscheidt***: Generating high resolution precipitation conditional on rainfall observations and satellite data, 2017, V, 173 S.

Heft 80: ***Tanja Zerenner***: Atmospheric downscaling using multi-objective genetic programming, 2016, [erschienen] 2017, X, 191 S.

Heft 81: ***Sophie Stolzenberger***: On the probabilistic evaluation of decadal and paleoclimate model predictions, 2017, IV, 122 S.

Heft 82: ***Insa Thiele-Eich***: Flooding in Dhaka, Bangladesh, and the challenge of climate change, 2017, V, 158 S.

Heft 83: ***Liselotte Bach***: Towards a probabilistic regional reanalysis for Europe, 2017 [erschienen] 2018, VI, 114 S.

Heft 84: ***Yen-Sen Lu***: Propagation of land surface model uncertainties in terrestrial system states, 2017, [erschienen] 2018, X, 120 S.

Heft 85: ***Rüdiger Hewer***: Stochastic physical models for wind fields and precipitation extremes, 2018, 99 S.

Heft 86: ***Sebastian Knist***: Land-atmosphere interactions in multiscale regional climate change simulations over Europe, 2018, VIII, 147 S.

Heft 87: ***Jessica Keune***: Integrated terrestrial simulations at the continental scale: Impact of groundwater dynamics and human water use on groundwater-to-atmosphere feedbacks during the European heatwave in 2003, 2019, IX, 172 S.

Heft 88: ***Christoph Beekmans***: 3-D Cloud Morphology and Evolution Derived from Hemispheric Stereo Cameras, 2019, [erschienen] 2020, VIII, 118 S.

Heft 89: ***Nils Weitzel***: Climate field reconstructions from pollen and macrofossil syntheses using Bayesian hierarchical models, 2019, [erschienen] 2020, XII, 153 S.

Heft 90: ***Alexander Kelbch***: Investigations to quantify individual exposure to solar ultraviolet erythemal radiation including cloud meteorological impact, 2020, III, 107 S.

Institut für Geowissenschaften
Abteilung Meteorologie
Mathematisch Naturwissenschaftliche Fakultät
Universität Bonn

institut für geowissenschaften
METEOROLOGIE